Two Particle Correlations in $Au + Au$ Collisions at 11.5 GeV/c per Nucleon

A Dissertation Presented

by

Thongbay Vongpaseuth

to

The Graduate School

in Partial Fulfillment of the Requirements

for the Degree of

Doctor of Philosophy

in

Physics

State University of New York
at
Stony Brook

May 1999

State University of New York
at Stony Brook

The Graduate School

Thongbay Vongpaseuth

We, the dissertation committee for the above candidate for the Doctor of Philosophy degree, hereby recommend acceptance of the dissertation.

Dr. Thomas K. Hemmick
Advisor
Professor of Physics

Dr. Chris Jacobsen
Professor of Physics

Dr. David P. Morrison
Physicist, Brookhaven National Laboratory

Dr. Edward Shuryak
Professor of Physics

This dissertation is accepted by the Graduate School.

Graduate School

Abstract of the Dissertation

Two Particle Correlations in $Au + Au$ Collisions at 11.5 GeV/c per Nucleon

by

Thongbay Vongpaseuth

Doctor of Philosophy

in

Physics

State University of New York at Stony Brook

1999

Two particle $\pi^+\pi^+$, $\pi^-\pi^-$, and K^+K^+ correlations have been measured in $Au + Au$ collisions at $11.5 AGeV$ at the AGS at BNL. The pion correlations exhibit the need for a λ parameters while the K^+K^+ correlation does not. The pion correlations' radius parameter is also considerably larger than the K^+K^+ radius parameter. The pion correlations' dependence on the reaction plane angle lead us to conclude that the azimuthal spatial asymmetry at freezeout is less than 8% for the π^+ source and less than 6% for the π^- source. Through a model study, for the π^-s, the average pair momentum dependence of the correlations and the invari-

ant multiplicities lead us to a set of global parameters for the π^- source: $R_G = 8.08 \pm 0.37 fm$, $\beta_t = 0.52^{+0.10}_{-0.27}$, $T = 0.068^{+0.026}_{-0.002} GeV$, $\tau_0 = 12.49^{+0.26}_{-4.28} fm$, and $\Delta\eta = 0.58^{+666}_{-0.06}$. With some assumptions and caveats, the full geomtrical transverse size for the K^+ source is estimated to be 0.5 to 1.2 times $R_G^{\pi^-}$.

For my father

Contents

List of Figures

List of Tables

Acknowledgements

The acknowledgements is the only part of this thesis that is never proofread by anyone else except the author herself. So there are bound to be those I will inadvertently omit due to my aging memory. For those that fall into this category, I beg their forgiveness and offer them my sicerest thanks. Now onto those that I recall (before I forget)...

The person that taught, influenced, and guided me most is my advisor Prof. Thomas K. Hemmick. I met Tom because he was the instructor for the graduate seminar that everyone was required to take. My first few conversations with him always began with one or two hour of neutrino oscillation physics (the topic of my seminar talk) and always ended with a *few* hours of relativistic heavy ion physics. If you think RHI physics is boring you should talk to Tom! I have never seen so much energy and enthusiasm for physics in any one person as is in Tom. The next thing I remember was that I wanted to study RHI physics. And lucky for me Tom agreed to be my advisor. He has an endless pool of knowledge and skills that I never cease to draw from. Without him, this thesis would have been impossible. I thank you Tom.

The Stony Brook RHI group is made up of a diverse bunch. I am fortunate to have crossed paths with them. Among those that I have benefited from are: Steve Johnson, Tim Piazza, Wen-Chen Chang, Sergey Panitkin, Mark Pollack, Youngil Kwon, Dariusz Miskowiec, Vlad Pantuev, Martin Trzaska, Jane Burward-Hoy, and Misha Kopytine. I thank them for their time, patience, and conversations. Special thanks to Rich Hutter and Socoro Delquaglio for doing things behind the scenes that made the experiment ran smoother and my life easier.

The McGill RHI group also deserve my thanks for plowing through the 1995 data tapes, and sharing some frustrations and panic attacks with me. They are: Yi Dai, Kirill Filimonov, and Yujin Qi.

The non-physics people that helped me through the years by lending their ears to listen to me are my college pals: Thea Antos, Jane Chew, Sophia Chen, Judy Kim, and Mary Kuo. I thank them for their time and fun when I needed it most.

I would also like to thank my mother and my late father, Bouakhay and Somchai, my sister and brother, Tongsay and Khamkeo, for giving me the freedom to do whatever I wanted to do. Without their support, this first doctor in the family ("first" being defined with a few qualifications) would not be a doctor today.

And finally my husband, Francisco, I thank him for loving and supporting me through all but my first graduate school years. (It was not under his control for being absent during my first year at Stony Brook. :) He has withstand my wraths, fits, and moods; he has even endured reading through the first draft of some chapters in this thesis; and he still is unwavered in his love and support.

I am fortunate that he has so much strength. This thesis is as much mine as it is his.

Chapter 1

An Introduction

Our universe is made up of matter. The constituents of matter are the leptons and the quarks. These constituents interact with one another through the four forces of nature: gravitational, electromagnetic, weak, and strong, whose carriers are the gauge bosons (gravitons, γ, W, Z, and gluons). The study of relativistic heavy ion (RHI) physics is motivated by the need to better understand Quantum Chromo-Dynamics (QCD), the theory of the strong force. In QCD, the only players are the quarks and the gluons because they carry color charge. At low energies the quarks and gluons are always bound into colorless packages; no free quark or gluon has been observed as an asymptotic state. QCD calculations can be done perturbatively for high energy, short range, reactions because in that regime, the QCD coupling constant is small. However it is notoriously difficult to make predictions for low energy, long range, reactions because QCD is non-perturbative in this regime due to the QCD coupling constant being large. Instead, numerical methods have been devised to make the calculations on a finite space time lattice. Lattice calculations predict [1] that as the density of quarks and gluons increase, along with their temperature, normal matter will under go a phase transition into a free, unbounded collection, the so called Quark Gluon Plasma (QGP). Initially lattice calculations were done for high temperature and low baryon density. Over the years the calculations have become more complex as they become more realistic. The predictions of the critical temperature vary from $150-250GeV$ and the critical density from $5-10$ times normal nuclear density. The order of the phase transition also flip-flopped from first to second order. A schematic of this phase boundary is drawn in Fig. 1.1. The early universe is believed to be an extremely hot thermal QGP that cooled and hadronized into the present day universe. It is also speculated that the exotic QGP may exist in the center of neutron stars where the matter density is several times that of normal matter density.

The possibility of creating the QGP in our earth bound laboratory is the aim of RHI physics. On the experimental side, by colliding heavy nuclei together at high energies, the hope is that the beam kinetic energy may be transfer into thermal energy because particles are created in a finite volume and they must collide with each other many times before escaping. The Brookhaven National Labs (BNL) tandem accelerator system was coupled to the Alternating Gradient Synchrotron (AGS) to be able to accelerate nuclei as large as Au to over $10GeV$ per nucleon. These energies are sufficient to produce roughly as many πs as the initial nucleons. At CERN (Conseil Europen pour la Recherche Nuclaire), the Super Protron Synchrotron (SPS) can accelerate nuclei as large as Pb to $160GeV$ per nucleon producing roughly four times as

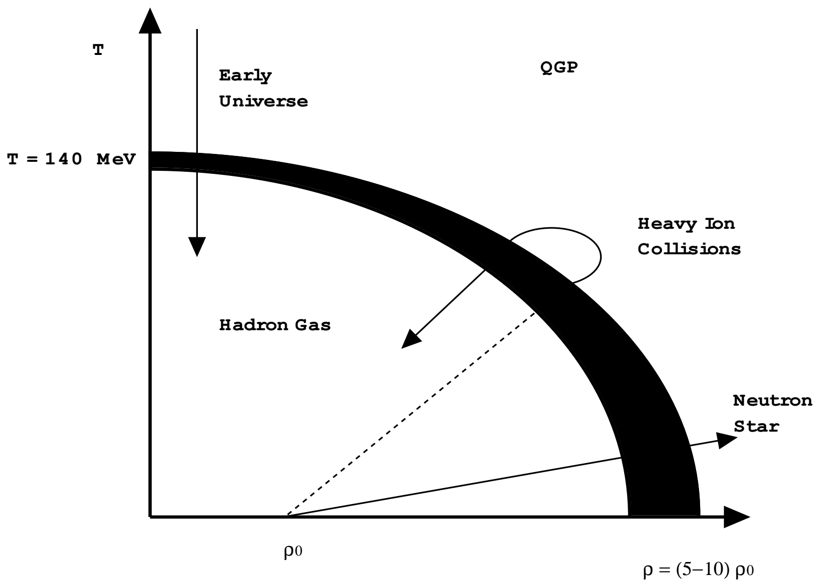

Figure 1.1: A schematic of the phase boundary between normal matter and the QGP. ρ_0 is normal nuclear matter density.

many πs as the initial nucleons. On the theoretical side, differences between plasma and normal hadronic matter were exploited to produce many possible signatures to identify the existence of the QGP [2]. Initially the proposed signatures were abundant, unique, and easy to measure. But as measurements are being made and theories develop with more realistic details, the difficulty of identifying the QGP becomes apparent. If the QGP is formed, it must dissolve and become normal hadronic matter for us to make a measurement. Most of the once unique and simple signatures of the QGP now also have corresponding "ordinary" scenarios explanations. Of the measurements that have been made [3] so far none can conclusively and unambiguously confirm the existence of a QGP. However a few - such as the CERES measurement of low mass dilepton enhancement [4] may prove to be chiral symmetry restoration in the QGP; NA50's observation of J/Ψ suppression [5] may be a measure of the color screening length in the QGP; and E877 and E895's flow measurements [61, 6] may show a softening of the equation of state - can potentially settle the question with more data points and theoretical tests to rule out the "ordinary" scenarios. Meanwhile current experiments are recording and analysing more data, constructions of even higher energy colliders (no fixed target) are underway. The Relativistic Heavy Ion Collider (RHIC) at BNL is scheduled to turn on in the fall of 1999. RHIC will be able to accelerate nuclei as large as Au up to $100GeV$ per nucleon. The Large Hadron Collider (LHC) at CERN is schedule to turn on in 2005. The LHC will be able to accelerate nuclei as large as Pb up to $3TeV$ per nucleon. If present day experiments cannot conclude the existence or non-existence of the QGP, the future experiments at RHIC and LHC will surely will due to if only the increase in statistics.

The present QGP formatation scenario has evolved to the following. By colliding heavy nuclei together at high enough energies, we are forcing the constituent quarks and gluons into a small volume. With this overcrowding, the quarks and gluons lose their "bag" boundaries. This matter then thermalizes, changing from normal matter to the QGP. The initial stages are the compression and heating, and equilibration stage that culminate in the formation of the QGP. After some time, the QGP will start to cool and in the process it will also expand through collisions of the constituents. During expansion, the QGP will revert back to normal matter once the dilution of particles reaches a certain level. The constituents will cease to interact as independent asymptotic particles and cluster to form hadrons that fly toward our detectors. This final stage is called freezeout. The amount of memory of the whole process that each detected particle retains will depend on the time birth and escape of the particles. All particles will have memory of the freezeout stage. Some will also have memory of the cool down and expansion and equilibrium stages. And fewer still (only direct leptons and photons) will have memory of the compression and heating stage. Nevertheless, a better understanding and maps of the later stages will help us extrapolate more accurately to the earlier stages.

To assess whether a QGP is created during collisions requires answering with certainty the following [7]: Did we create a high enough particle density (energy density) during the compression and heating stage to create the QGP? Was there enough equilibration of the matter to undergo a thermodynamic phase transition? These are difficult questions to answer directly. Initially hadronic correlation measurements, via intensity interferometry, promised to provide a straight forward volume (size) measurement of the particle emitting source. Since all the hadrons are detected after the freezeout stage, a measure of the size of the collision zone at that last stage will nevertheless provide us with a map to trace back to the earlier stages. The hope of a size measurement is based on the successes of Hanbury-Brown and Twiss [8] who first discovered and applied the technique to the field of astronomy by measuring the size of stars; and Goldhaber, Goldhaber, Lee, and Pais [9] who independently rediscovered the technique and applied it to measuring the size of pion emitting sources in high energy physics. The answer to the first question is then attainable by correlation measurements and the answer to the second question has to be deferred to other types of measurements. Unfortunately *and* fortunately, RHI collisions create sources that are dynamic, as opposed to the static nature of stars. The unfortunate part is that intensity interferometry is no longer a straight forward tool for size measurement in RHI physics. The fortunate part is that, with modifications, intensity interferometry can still be a tool for size measurement and in addition, address the equilibrium issue that may answer the second question asked above. The dynamical dependences of the correlation measurements are due to random motion and collective motion of the source. Random motion is caused by equilibration and collective motion is caused by pressure. Having a clearer picture of these two components of the dynamics, and having a size measurement will help us move one step closer to confirming or refuting the existence of the QGP.

In this thesis, we will present measurements of correlation functions of

π^+, π^-, and K^+. The πs, being the more numerous species, will be studied in greater detail. We will study the general features of the correlation functions for π^+, π^-, and K^+. In more details, we will study the correlations as a function of: reaction plane angle (for π^+ and π^-), and average momentum of the pair (for π^+ and π^-). There are general differences among π^+, π^-, and K^+. These differences will show in their corresponding correlations. The distinction between corresponding cause and effect is not clear but will be explored with the help of model studies. With the reaction plane dependence the pion correlation functions, we will deduce to what degree the initial state "almond" shape of the collision zone in semi-peripheral collisions is lost as the system moves toward equilibrium. We will also show that the correlation functions depend on the average momentum of the particle pair as well as the pair momentum difference. The average momentum dependence is the effect of the dynamical source and through an explicit source model we can extract the source estimates of the dynamics and determine the true source radius.

Chapter 2

The Formalism of the Correlation Function

The theory of two bosonic particle correlations (C_2) has grown and matured extensively since its inception. The evolution of the theory can be separated into two parts: the static and the dynamic source. In this chapter we will introduce the reader to the static source first. In this framework, C_2 is much easier to formulate, to understand, and to realize its potential for information. We then introduce the reader to the dynamic source, which hand-in-hand with its complexity, contains many folds of richness in its extractable information. Finally, the need for an extra parameter for the complete parameterization of C_2, motivated by data, is discussed.

The following discussions are drawn mainly from Refs. [10], [11], and [12]. The reader should refer to them for a more detailed, general introduction to correlations than what is provided below.

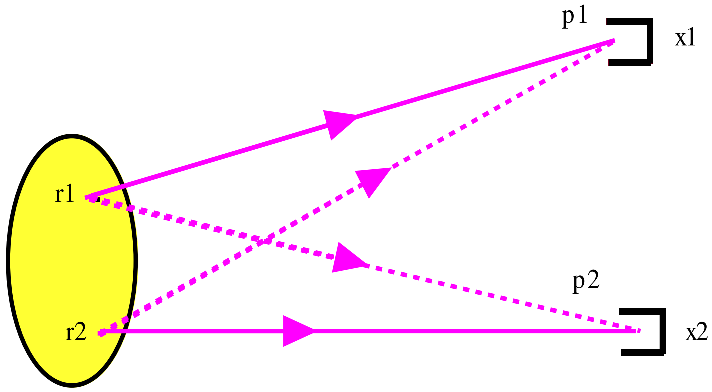

Figure 2.1: The different paths a pair of indistinguishable particles may take to reach our detectors are drawn.

2.1 The Static Source and the Standard Parameterization

To begin, let us consider an extended source that is composed of many independent sources. These independent sources emit massive bosonic particles that we can measure with our detectors. If the particles are identical bosons, the two possible paths that the particles can travel to reach our detectors, as shown in Fig. 2.1, are equally likely. *Amplitude* interferometry, a commonly used technique in physics, is the study of the interference pattern at $x1$ and $x2$ caused by the phase difference between the probability *amplitudes* of the particles to travel the two paths to $x1$ and $x2$. *Intensity* interferometry, on the other hand, is the measure of the correlation between two particles observed simultaneously at $x1$ and $x2$. The probability of joint observation (the amplitude squared) is measured relative to the product of the probability of each observation:

$$C_2 = \frac{P(\vec{p}_1, \vec{p}_2)}{P(\vec{p}_1)P(\vec{p}_2)} \tag{2.1}$$

where $P(\vec{p}_1, \vec{p}_2)$ is the probability of detecting a particle with momentum $\vec{p}_1$ and a second particle with momentum $\vec{p}_2$; $P(\vec{p}_1)$ ($P(\vec{p}_2)$) is the probability of detecting a particle with momentum $\vec{p}_1$ ($\vec{p}_2$) regardless of the second (first) particle's momentum.[1] From Eq. 2.1 we see that C_2 deviates from unity, $P(\vec{p}_1, \vec{p}_2) \neq P(\vec{p}_1)P(\vec{p}_2)$, if there is statistical correlation (Bose-Einstein or Fermi) or interactions (Coulomb, Strong, etc.) between particles. Through the Wigner formalism, one can arrive at the expressions for the probabilities in Eq. 2.1 [15]: If we have a source function $S(r_i, p_i)$ parameterizing the probability for the emission of each i^{th} massive boson from space-time coordinate r_i with (asymptotic) four momentum p_i, then for non-interacting particles:

$$\begin{aligned} P(\vec{p}_1, \vec{p}_2) &= \int\int \mid \Psi_{12}^{BE} \mid^2 S(r_1, \frac{p_1+p_2}{2}) S(r_2, \frac{p_1+p_2}{2}) d^4r_1 d^4r_2 && (2.2) \\ P(\vec{p}_1)P(\vec{p}_2) &= \int\int \mid \Psi_{12}^{Ref} \mid^2 S(r_1, p_1) S(r_2, p_2) d^4r_1 d^4r_2 && (2.3) \end{aligned}$$

where Ψ_{12}^{BE}, approximated by a plane wave, is the two particles wave function that is symmetric under particle exchange:

$$\Psi_{12}^{BE} = \frac{1}{\sqrt{2}}\{e^{ip_1(x_1-r_1)}e^{ip_2(x_2-r_2)} + e^{ip_1(x_1-r_2)}e^{ip_2(x_2-r_1)}\} \tag{2.4}$$

[1] Please note: in this thesis four vectors will simply be denoted as plain letters, i.e. p, r, x, etc; three vectors will be denoted as plain letters with a vector sign, i.e. $\vec{p}$, $\vec{r}$, $\vec{x}$, etc.

and $\mid \Psi_{12}^{Ref} \mid^2$ is the uncorrelated wave function squared which consists of the addition of the two alternative scenarios' intensities:

$$\mid \Psi_{12}^{Ref} \mid^2 = \frac{1}{2}\{\mid e^{ip_1(x_1-r_1)}e^{ip_2(x_2-r_2)} \mid^2 + \mid e^{ip_1(x_1-r_2)}e^{ip_2(x_2-r_1)} \mid^2\} = 1. \tag{2.5}$$

Working out the integrations of Eq. 2.2 and 2.3 and dividing the results, C_2 becomes:

$$\begin{aligned} C_2(\vec{p}_1, \vec{p}_2) = \frac{1}{2}\Big(2 \quad &+ \quad \frac{\int\int S(r_1,K)S(r_2,K)e^{i(p_1-p_2)(r_1-r_2)}d^4r_1d^4r_2}{\int\int S(r_1,p_1)S(r_2,p_2)d^4r_1d^4r_2} \\ &+ \quad \frac{\int\int S(r_1,K)S(r_2,K)e^{-i(p_1-p_2)(r_1-r_2)}d^4r_1d^4r_2}{\int\int S(r_1,p_1)S(r_2,p_2)d^4r_1d^4r_2}\Big) \end{aligned} \tag{2.6}$$

where $K = \frac{p_1+p_2}{2}$, the average momentum of the pair. This equation can be recognized as the normalized Fourier transform of the source function S:

$$\begin{aligned} C_2(\vec{p}_1, \vec{p}_2) = \frac{1}{2}\Big(2 \quad &+ \quad \frac{\int S(r_1,K)e^{iqr_1}d^4r_1}{\int S(r_1,p_1)d^4r_1}\frac{\int S(r_2,K)e^{-iqr_2}d^4r_2}{\int S(r_2,p_2)d^4r_2} \\ &+ \quad \frac{\int S(r_1,K)e^{-iqr_1}d^4r_1}{\int S(r_1,p_1)d^4r_1}\frac{\int S(r_2,K)e^{iqr_2}d^4r_2}{\int S(r_2,p_2)d^4r_2}\Big) \\ \approx 1 \quad &+ \quad \frac{\int S(r,K)e^{iqr}d^4r}{\int S(r,K)d^4r}\frac{\int S(r,K)e^{-iqr}d^4r}{\int S(r,K)d^4r} \\ \approx 1 \quad &+ \quad \mathcal{S}(q,K)\mathcal{S}^*(q,K) = 1 + \mid \mathcal{S}(q,K) \mid^2 \end{aligned} \tag{2.7}$$

with $q = p_1 - p_2$, the momentum difference of the pair and $\mathcal{S}(q,K)$ is the normalized Fourier transform of $S(r,K)$. The approximation, $p_1 \approx p_2 \approx K$, is appropriate and valid because the correlation signal exists at small q [13]. Though Eq. 2.7 looks simple and elegant, it contains a hidden complication. At first sight it seems trivial to invert the Fourier transform on the measured C_2 to discover the source distribution $S(r,p)$. However, with careful examination, we must realize that the left hand side of Eq. 2.7 spans only six ($\vec{p}_1 \Rightarrow$

$3, \vec{p}_2 \Rightarrow 3$) independent components while the right hand side spans seven ($q \Rightarrow 4, K \Rightarrow 4$, minus 1 from $q \cdot K = 0$), because it includes off shell behavior of S. The missing component on the l.h.s. is a result of our measuring on shell particles for our correlation. Thus the inverse Fourier transform of Eq. 2.7 will never be uniquely determined. We therefore have to rely on fitting our measured C_2 to some form and interpreting the fit parameters in the framework of some assumed models of the source.

2.1.1 General Assumptions About the Source

For simplicity, we start with the assumption that $S(r,p)$ is factorizable.[2] Namely:

$$S(r,p) = G(p)F(r). \tag{2.8}$$

Since the integration in Eq. 2.7 does not depend on p, $G(p)$ from the numerator simply cancels with one in the denominator.

$$\begin{aligned} C_2(q) &= 1 + \mid \frac{\int F(r) e^{iqr} d^4r}{\int F(r) d^4r} \mid^2, & (2.9) \\ &= 1 + \mathcal{F}(q)\mathcal{F}^*(q), & (2.10) \\ &= 1 + \mid \mathcal{F}(q) \mid^2 . & (2.11) \end{aligned}$$

We can further assume an explicit form, such as a spherically symmetric Gaussian, for $F(r)$, to explore the shape of C_2. Given

$$F(r) = \frac{1}{4\pi^2 R^4} e^{-r^2/2R^2}, \tag{2.12}$$

[2]Note: This assumption is incorrect for a dynamical source.

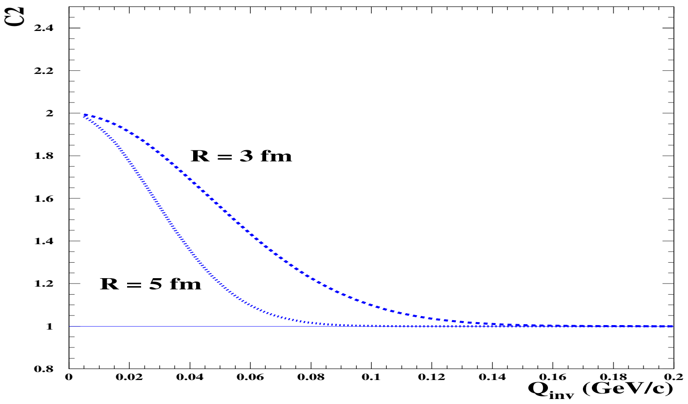

Figure 2.2: Example C_2 for different source sizes.

---

then the Fourier transform is:

$$\mathcal{F}(q) = e^{(-q^2R^2)/2}, \tag{2.13}$$

resulting in:

$$C_2(q) = 1 + e^{-q^2R^2}. \tag{2.14}$$

The width of C_2 is then inversely proportional to the Gaussian radius R. $C_2(0) = 2$ while $C_2(q = large) = 1$. From this it is obvious that there indeed is an enhancement for non-interacting particle pairs whose q is close to zero. An example of C_2 for different Rs is shown in Fig. 2.2.

Having a spherically symmetric source in all three spatial and time directions is highly unlikely and not expected in heavy ion collisions. A more general form for $F(r)$, is when spherical symmetry is not assumed:

$$F(r) = \frac{1}{4\pi^2R^4}e^{(-r_x^2/2R_x^2 - r_y^2/2R_y^2 - r_z^2/2R_z^2 - t^2/2\tau^2)}, \tag{2.15}$$

$$C_2(q) = 1 + e^{(-q_x^2 R_x^2 - q_y^2 R_y^2 - q_z^2 R_z^2 - q_\emptyset{}^2 \tau^2)}. \tag{2.16}$$

Since in this thesis, we measure C_2 for on shell massive particles (we do not measure $\gamma\gamma$ correlations), the l.h.s. of Eq. 2.16 has only three independent variables while the r.h.s. appears to have four. One of the variables on the r.h.s. is in fact redundant. We can rewrite $q_\emptyset$ as:

$$q_\emptyset = \vec{\beta} \cdot \vec{q}, \tag{2.17}$$

$$\vec{\beta} = \frac{\vec{K}}{K_\emptyset} \approx \frac{\vec{K}}{E_K}. \tag{2.18}$$

$K_\emptyset = (p_{\emptyset_1} + p_{\emptyset_2})/2$ is the off shell average energy component while $E_K = \sqrt{m^2 + \vec{K}^2}$ is the on shell average energy. If we expand $K_\emptyset$ for small q, we then find that:

$$\begin{aligned} K_\emptyset &= E_K \left(1 + \frac{\vec{q}^2}{8E_K^2} + \mathcal{O}\left(\frac{\vec{q}^4}{E_K^4}\right) + \ldots\right) \\ &\approx E_K. \end{aligned} \tag{2.19}$$

The approximation $K_\emptyset \approx E_K$ is thus valid for small q, the area of interest where the correlation deviates from one. $\vec{\beta}$ can then be approximated by the average velocity of the particle pair.

Before we continue, a change of coordinate system proves to be convenient. Devised by Bertsch [14] and Pratt et al [15], a convenient coordinate to have is one in which q_z is along the beam axis, the "long" direction; q_x is parallel to K_t, the "outward" direction; and q_y is perpendicular to K_t, the "sideward" direction. This is the standard parameterization of C_2. One can always rotate to the "out-side-long" (osl) coordinate without losing any information:

$$(K_\emptyset, K_x, K_y, K_z) \;\; \rightarrow \;\; (K_\emptyset, K_t, 0, K_z),$$

$$
\begin{aligned}
(q_\emptyset, q_x, q_y, q_z) &\rightarrow (q_\emptyset, q_o, q_s, q_l), \\
(t, x, y, z) &\rightarrow (t, o, s, l);
\end{aligned}
\tag{2.20}
$$

$$
C_2(q) = 1 + e^{(-q_o^2 R_t^2 - q_s^2 R_t^2 - q_l^2 R_z^2 - q_\emptyset{}^2 \tau^2)}. \tag{2.21}
$$

The variables conjugate to q_o and q_s are to the lowest approximation equal to the same variable, R_t because we believe that the source we are creating in the laboratory, is more or less azimuthally symmetric, particularly for central collisions. [3] The source is stretched along the beam direction because that is the direction of the input momentum before the source is created. There is some dimension in the transverse direction because the beam and target particles have finite transverse dimensions. Thus the picture of the source is generally a cigar shape with the long axis of the cigar parallel to the beam axis (the "long" axis), although the parameterization works equally well for a "pancake" (shorter along the beam axis) shape.

Now we replace Eq. 2.16 by Eq. 2.21 and $q_\emptyset$ by:

$$
\begin{aligned}
q_\emptyset &= \beta_o q_o + \beta_s q_s + \beta_{||} q_l, \\
&= \beta_t q_o + \beta_{||} q_l,
\end{aligned}
\tag{2.22}
$$

$$
q_\emptyset{}^2 = \beta_t^2 q_o^2 + \beta_{||}^2 q_l^2 + 2\beta_t \beta_{||} q_o q_l, \tag{2.23}
$$

where the velocity of the pair in the "side" direction, perpendicular to K_t direction, is zero, $\beta_s = 0$, by definition. Regrouping the terms in Eq. 2.21 we find:

$$
C_2(q) = 1 + e^{(-q_o^2 (R_t^2 + \beta_o^2 \tau^2) - q_s^2 R_t^2 - q_l^2 (R_z^2 + \beta_{||}^2 \tau^2) + 2 q_o q_l \beta_o \beta_{||} \tau^2)}, \tag{2.24}
$$

[3] We shall test this assumption in detail for non-central collisions.

$$= \quad 1 + e^{(-q_o^2 R_o^2 - q_s^2 R_s^2 - q_l^2 R_l^2 + 2q_o q_l R_{ol}^2)}, \tag{2.25}$$

where

$$\begin{aligned} R_s &= R_t, \\ R_o^2 &= R_s^2 + \beta_o^2 \tau^2, \\ R_l^2 &= R_z^2 + \beta_{||}^2 \tau^2, \\ R_{ol}^2 &= \beta_o \beta_{||} \tau^2. \end{aligned} \tag{2.26}$$

2.1.2 Different Reference Frames

So far we have not indicated if the source itself is moving or not. When we think about Lorentz tranformation it is useful to indentify invariants first. C_2 is a Lorentz invariant as follows from examining Eq. 2.7. Therefore as long as the qs and Rs are in the same frame, Eq. 2.25 is always valid. We are however most interested in Rs in the source's rest frame. Rs in this special frame are not distorted by motion and are easier to compare from different experiments and different colliding systems. However we do not measure qs in the source's rest frame, but rather we measure qs in the lab. To keep the Rs untouched (in the source's rest frame), we can transform the qs from the lab to the special frame.

$$(q'_\emptyset, q'_o, q'_s, q'_l)_{Lab} \rightarrow (q_\emptyset, q_o, q_s, q_l)_{Source's\ Rest\ Frame} \tag{2.27}$$

The source's rest frame is not known a priori however; this special frame is not necessarily a universal frame for the whole extension of the source. The center of mass frame of the beam and target, in general, cannot be assumed to be the source's rest frame because the source has a finite extension and the different sections of the source can be in relative motion.

There have been conjectures as to what frame is the source's rest frame. Let us go over some popular ones.

If we assume that the source has the simplest form, static fluid cells, then the source's rest frame is the particle pairs' center of mass frame (PCMS). In this frame $\vec{p}_{1_{PCMS}} + \vec{p}_{2_{PCMS}} = 0$. We can boost $q' = q_{lab} \rightarrow q_{PCMS}$ via the relations:

$$\begin{aligned} \vec{q}_{PCMS} &= \vec{q'} + \vec{v}\Big[\frac{\vec{q'} \cdot \vec{v}}{v^2}(\gamma - 1) - \gamma q'_{\emptyset}\Big]; \\ q_{\emptyset_{PCMS}} &= \gamma(q'_{\emptyset} - \vec{q'} \cdot \vec{v}) = 0 \end{aligned} \tag{2.28}$$

where $\gamma = 1/\sqrt{1 - v^2}$, and $\vec{v}$ is the velocity of the boosted frame relative to the lab. Please note that there is a unique $\vec{v}$ for every particle pair. Using Eq. 2.23, we can simplify the above as:

$$q_{i_{PCMS}} = a_{ij} q'_j \text{ for i,j=1,2,3;} \tag{2.29}$$

Eq. 2.21 then simplifies:

$$C_2(q) = 1 + e^{(-q_o{}^2 R_t{}^2 - q_s{}^2 R_t{}^2 - q_l{}^2 R_z{}^2)} \tag{2.30}$$

since $q_{\emptyset_{PCMS}} = 0$ for two identical massive particles and where q_i are the PCMS frame quantities that are linear combinations of q'_i lab frame quantities (via Eq. 2.29). The temporal information, τ, is thus "lost" in this frame.

On the other hand, if we consider a source that is azimuthally symmetric and longitudinally boost invariant, such as the one suggested by Bjorken [16], then a rest frame in a fluid cell of the source is one in which $p_{z1_{LCMS}}+p_{z2_{LCMS}} = 0$; this is the longitudinal center of mass frame (LCMS). This frame is a simplification of the PCMS frame, in that there is a boost from the lab frame in only the longitidunal direction. In the LCMS frame $\beta_{||_{LCMS}} = 0$, and Eq. 2.23 is simply:

$$q_\emptyset = \beta_o q_o. \tag{2.31}$$

Since we are boosting only in the "long" direction, the four-vector components perpendicular to "long," namely the q_o and q_s components, are not affected by the transformation. But velocity, $\vec{\beta}$, is a three vector and does not follow the Lorentz transformation rules going from one observer frame to another. An easy way to recognize this is to remind ourselves that $\vec{\beta}$, written in terms of components of the 4 vector K, is:

$$\begin{aligned}
\vec{\beta}_{lab} &= \vec{K}_{lab}/K_{\emptyset lab}, \\
\beta_{olab} &= K_{olab}/K_{\emptyset lab}, \\
\beta_{oLCMS} &= K_{oLCMS}/K_{\emptyset LCMS}, \\
&= K_{olab}/K_{\emptyset LCMS}.
\end{aligned} \tag{2.32}$$

Eq. 2.21 then becomes:

$$\begin{aligned}
C_2(q) &= 1 + e^{-q_o^2(R_t^2+\beta_o^2\tau^2)-q_s^2R_t^2-q_l{}^2R_z{}^2}, \\
&= 1 + e^{-q_\emptyset^2 R_o{}^2-q_s^2R_s^2-q_l{}^2R_z{}^2}.
\end{aligned} \tag{2.33}$$

Then τ is extractable from the difference between $R_o{}^2$ and R_s^2.

Both the PCMS and the LCMS frames require boosting *each* particle pair by different velocities. This lead to non-trivial interpretation of the Rs if the source's rest frame does not coincide with either frame. A third option is a fixed observer's frame. In this frame, we boost *all* particle pairs by one fixed velocity. Then if and when the source frame is found to be different than the one we assumed, we can deduce the Rs in the source's rest frame by forming linear combinations of the extracted Rs.[4]

2.2 The Dynamical Source and Its Parameterization

A crucial fallacy in the previous section's discussion is the assumption of factorizability of the source function (Eq. 2.8). This assumption is valid when the source is static, such as a star. A photon that is emitted from a spatial-temporal point on the surface of a star will have an random momentum p. However, a source created in heavy ion collision, is much more complex than a star. The reaction is more like an explosion rather than a burning. There is a preferential distribution of momentum depending on where the particle is emitted. This commonly is called position-momentum correlation, or x-p correlation [13, 17]. If there is expansion of and/or temperature gradient in the source, then there necessarily is an x-p correlation. In addition, not all

[4]It is a straight forward but algebraically lenthy calculation to find the linear combinations of extracted Rs for each source's rest frame Rs. It is not illuminating so we do not do it here. Besides, there is a better way to account for guessing the wrong frame, to boost all of one's measured qs to, as in the next section.

particles are emitted simultaneously. They are emitted over a finite time. Eq. 2.7 then cannot be reduced to be just dependent on the momentum difference q. Instead, C_2 depends also on the average pair momentum K.

Heinz et al [18] have reformulated C_2 and derived "model independent" expressions for the fit radii. A source with radii that have the most general K dependence is used in Eq. 2.7. It can be shown [19] that C_2, to within experimental precision, is sensitive only to the 2^{nd} moment of the space-time distribution. Given this assumption we can formulate a completely general source by formulating a source which is 2^{nd} order in a all observables. It is sufficient to approximate S by a Gaussian part plus all higher moment terms δS:

$$S(x,K) = N(\vec{K})S(\tilde{x}(\vec{K}),K)e^{-\frac{1}{2}\tilde{x}^{\mu}(\vec{K})B_{\mu\nu}(\vec{K})\tilde{x}^{\nu}(\vec{K})} + \delta S(x,K). \tag{2.34}$$

The $N(\vec{K})$, $\bar{x}(\vec{K})$, and $B_{\mu\nu}(\vec{K})$ are chosen such that δS has vanishing zeroth, first, and second order space time moments. $N(\vec{K})$ is also fixed to give the correct single particle spectrum. $\bar{x}(\vec{K})$ is the Gaussian center of S, i.e. the point of highest probability of emission of particles with momentum $\vec{K}$. And $B^{-1}_{\mu\nu}(\vec{K}) = \langle (x-\bar{x})_{\mu}(x-\bar{x})_{\nu}\rangle = \langle \tilde{x}_{\mu}\tilde{x}_{\nu}\rangle$ is the width of the Gaussian relative to $\bar{x}(\vec{K})$ from which particles are emitted. Integrating Eq. 2.7 we find:

$$\begin{aligned} C_2(\vec{q},\vec{K}) &= 1 + e^{-q^{\mu}q^{\nu}B^{-1}_{\mu\nu}(\vec{K})} + \delta C(\vec{q},\vec{K}), && (2.35) \\ &\approx 1 + e^{-q^{\mu}q^{\nu}\langle\tilde{x}_{\mu}\tilde{x}_{\nu}\rangle(\vec{K})}. && (2.36) \end{aligned}$$

Only δS contributes to δC. Therefore δC contains only third and higher moment pieces of of the source. It has been shown that δC is small in magnitude compared to the Gaussian part (Eq. 2.36) and is discernible, if at all, away from the $q = 0$ region. The $B^{-1}_{\mu\nu}(\vec{K})$ then are the average separation between particles pairs, or "homogeneity lengths." They are related to, but not equal to, the geometric extension of the source (depending on the nature of the x-p correlation). Eq. 2.36 thus far is model independent. With a replacement of the redundant component, $q_\emptyset$, as in the previous section, with Eq. 2.23 into Eq. 2.36, we arrive at:

$$R^2_{ij}(\vec{K}) = \langle(\tilde{x}_i - \beta_i\tilde{t})(\tilde{x}_j - \beta_j\tilde{t})\rangle \text{where } i,j = 1,2,3 = o,s,l. \qquad (2.37)$$

By symmetry, for an azimuthally symmetric source all coefficients linear in q_s must be zero. We can thus see that the only nonzero parameters are the ones in the standard parameterization (osl) form (Eq. 2.25) with:

$$\begin{aligned} R^2_o(\vec{K}) &= \langle(\tilde{x} - \beta_o\tilde{t})^2\rangle, \\ R^2_s(\vec{K}) &= \langle\tilde{y}^2\rangle, \\ R^2_l(\vec{K}) &= \langle(\tilde{z} - \beta_l\tilde{t})^2\rangle, \\ R^2_{ol}(\vec{K}) &= \langle(\tilde{x} - \beta_o\tilde{t})(\tilde{z} - \beta_l\tilde{t})\rangle \end{aligned} \qquad (2.38)$$

It is clear from this notation that these standard parameters mix spatial and temporal information of the source in a non-trivial way. An alternative choice of parameters for an azimuthally symmetric source is one in which we keep q_l and $q_\emptyset$, while q_o and q_s are replaced by $q_\perp = \sqrt{q_o^2 + q_s^2}$. Additionally, we can explicitly write the velocity of the lab frame relative to the source's rest frame in our fit equation. Eq. 2.36 then takes the form of:

$$C_2(\vec{q}, \vec{K}) = 1 + e^{-R^2_\perp q^2_\perp - R^2_\parallel \gamma^2 (q_l - v q_\emptyset)^2 - \tau^2\gamma^2(q_\emptyset - v q_l)^2}$$

$$= \quad 1 + e^{-R_\perp^2 q_\perp^2 - R_\parallel^2 (q_l^2 - q_\emptyset{}^2) - (R_\emptyset{}^2 + R_\parallel^2)(q \cdot U)^2}, \tag{2.39}$$

where

$$U(\vec{K}) \quad = \quad \gamma(\vec{K})(1, 0, 0, v(\vec{K})); \tag{2.40}$$

and

$$\begin{aligned} R_\perp^2(\vec{K}) &= \langle \tilde{y}^2 \rangle, \\ R_\parallel^2(\vec{K}) &= \langle (\tilde{z} - \beta_\parallel \tilde{x}/\beta_\perp)^2 \rangle - \beta_\parallel^2 \langle \tilde{y}^2 \rangle / \beta_\perp^2, \\ R_\emptyset{}^2(\vec{K}) &= \langle (\tilde{t} - \tilde{x}/\beta_\perp)^2 \rangle - \langle \tilde{y}^2 \rangle / \beta_\perp^2. \end{aligned} \tag{2.41}$$

Eq. 2.39 has the advantage that it is longitudinally boost invariant; consequently the Rs are also invariant. Since there exists a longitudinally boosted reference frame in which $v(\vec{K}) = 0$, the Rs extracted from fitting to Eq. 2.39 measure the source in this special frame and do not depend on the longitudinal velocity of the observer's frame. Going to the special frame in which $v(\vec{K}) = 0$ gives a physical interpretation to the Rs:

$$\begin{aligned} R_\parallel^2(\vec{K}) &\approx \langle \tilde{z}^2 \rangle, \\ R_\emptyset{}^2(\vec{K}) &\approx \langle \tilde{t}^2 \rangle, \end{aligned} \tag{2.42}$$

where the approximation is valid for cigar shape sources ($\langle \tilde{z}^2 \rangle, \langle \tilde{t}^2 \rangle \gg \langle \tilde{x}^2 \rangle, \langle \tilde{y}^2 \rangle$) [20]. The fitted Rs from Eq. 2.39 are then the averaged spatial and temporal separation between emitted particles and the maximum point of emission for that fluid cell. Eq. 2.39 was first derived by Yano and Koonin [21], and Podgorestskiǐ [22] for a less generalized model. Thus Eq. 2.39 is commonly called the Yano-Koonin-Podgorestskiĭ (YKP) parameterization in honor of those who first wrote it down.

The standard radii can be equated with the YKP radii by the following relations [18]:

$$\begin{aligned}
R_s^2 &= R_\perp^2 \\
R_l^2 &= (1-\beta_{||})R_{||}^2 + \gamma^2(\beta_{||}-v)^2({R_\emptyset}^2 + R_{||}^2) \\
R_{diff}^2 &= R_o^2 - R_s^2 = \beta_\perp^2\gamma^2({R_\emptyset}^2 + v^2 R_{||}^2) \\
R_{ol}^2 &= \beta_\perp(-\beta_{||}R_{||}^2 + \gamma^2(\beta_{||}-v)^2({R_\emptyset}^2 + R_{||}^2))
\end{aligned} \tag{2.43}$$

These provide a powerful consistency check of the Gaussian part of $S(x, K)$ by fitting the measured data to both parameterizations.

2.3 The Chaoticity Parameter

It has been experimentally observed from the very beginning that in the low $q \approx 0$ region C_2 falls short of the expected value of 2. This effect is accounted for by introducing another parameter, λ, into C_2 to characterize the height of $C_2(0)$:

$$C_2 = 1 + \lambda e^{-q^2 R^2}. \tag{2.44}$$

One physical explanation to justify $\lambda < 1$ is an admixture of coherent bosons [23]. In the case of coherence, the phases of particle 1 and 2 are fixed relative to each other. Thus $\langle \mid \Psi_{12} \mid^2 \rangle = \langle \mid \Psi_1 \mid^2 \rangle \langle \mid \Psi_2 \mid^2 \rangle$, and $C_2 = 1$. Eq. 2.44 allows for a mixture of a coherent and incoherent (chaotic) sources. λ can be related to the fraction of bosons from the incoherent source, hence the name - *chaoticity parameter.*

An alternative justification for λ is that the particles can be emitted from a source which is very different from a single Gaussian. Consider for example a narrow and wide Gaussian source as [24]:

$$F(r) = \frac{\lambda}{4\pi^2 R_1^4} e^{-r^2/2R_1^2} + \frac{1-\lambda}{4\pi^2 R_2^4} e^{-r^2/2R_2^2} \tag{2.45}$$

where $R_2 >> R_1$. Such a scenario can arise from picturing the first Gaussian as direct boson production, and the second Gaussian as boson production from resonance decays [25]. Since it would take a very small q difference to see the second Gaussian (the width of $C_2(q)$ is inversely proportional to R), and we have finite resolution in our q measurements, then it is conceivable that the second Gaussian is not detectable in our measured C_2. See Fig. 2.3. The C_2 with only the first Gaussian that is measurable is then described by Eq. 2.44.

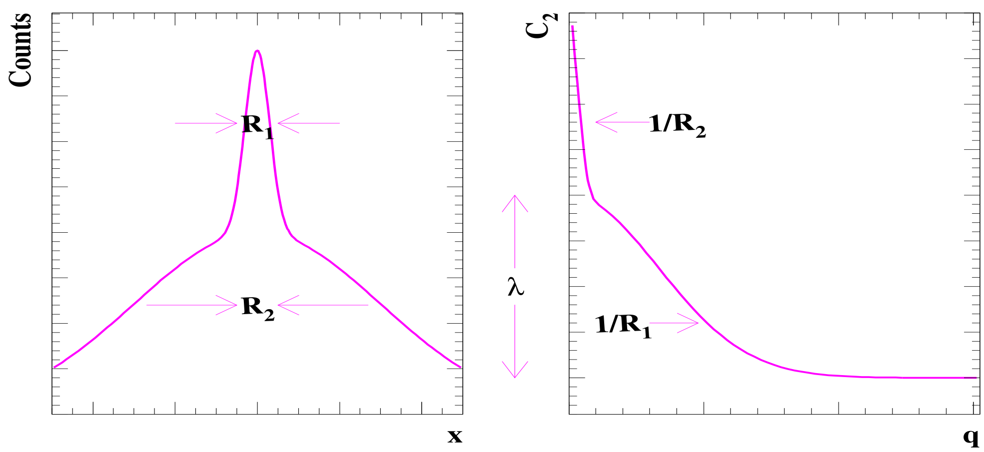

Figure 2.3: Schematic of two Gaussian sources, $R_2 >> R_1$, in spatial coordinate and its Fourier transform to momentum coordinate.

Chapter 3

Experimental Apparatus

E877 was a fixed target experiment located in the C5 beam line of the Alternating Gradient Synchrotron (AGS) at the Brookhaven National Laboratory (BNL) from 1993 to 1995. The data for this thesis are derived from the winter of 1994 and winter of 1995 data runs. The beam and target are ^{197}Au nuclei and the beam momentum is $11.5GeV$ per nucleon ($AGeV$).

3.1 The Alternating Gradient Synchrotron

The heavy ion accelerating complex at BNL is composed of essentially three parts. The first component is the tandem. The tandem accelerates the Au atom to an initial energy of $\sim 1AMeV$. In the acceleration process, the Au atom loses some electrons and becomes a positively charged ion. The Au ion exits the tandem and have more electrons stripped off by going through a thin foil. These low energy Au nuclei are then transferred to the AGS booster, which accelerates them to 200 AMeV. Before leaving the booster, the Au ions are passed through another foil to completely strip them of any remaining electrons. After the booster is the AGS itself. In the AGS ring, the Au beam is accelerated to 11.5 AGeV before it is extracted through the C5 line into our experiment.

3.2 The E877 Experiment

The E877 experiment is a focusing magnetic analyzing spectrometer with three major components. The first is the beam definition part, accounting for a good beam particle and providing a start time for the event. The second is the event characterization component, which classifies the event in terms of centrality and reaction plane angle. The third is the forward spectrometer, which is utilized for tracking particles and identifying them in terms of their masses. Throughout the rest of the text, we employ a right handed coordinate system, with the positive z direction being the direction of the beam, and the positive y direction pointing upward, toward the ceiling. A top view of the components of the experimental apparatus and their approximate locations in the beam line is shown in Fig. 3.1.

3.2.1 Beam Definition Detectors

Essential information of each track, its momentum and time of flight, are measured relative to the beam particle. Therefore it is important to measure the beam particle's properties accurately. The beam definition detectors fulfill this task.

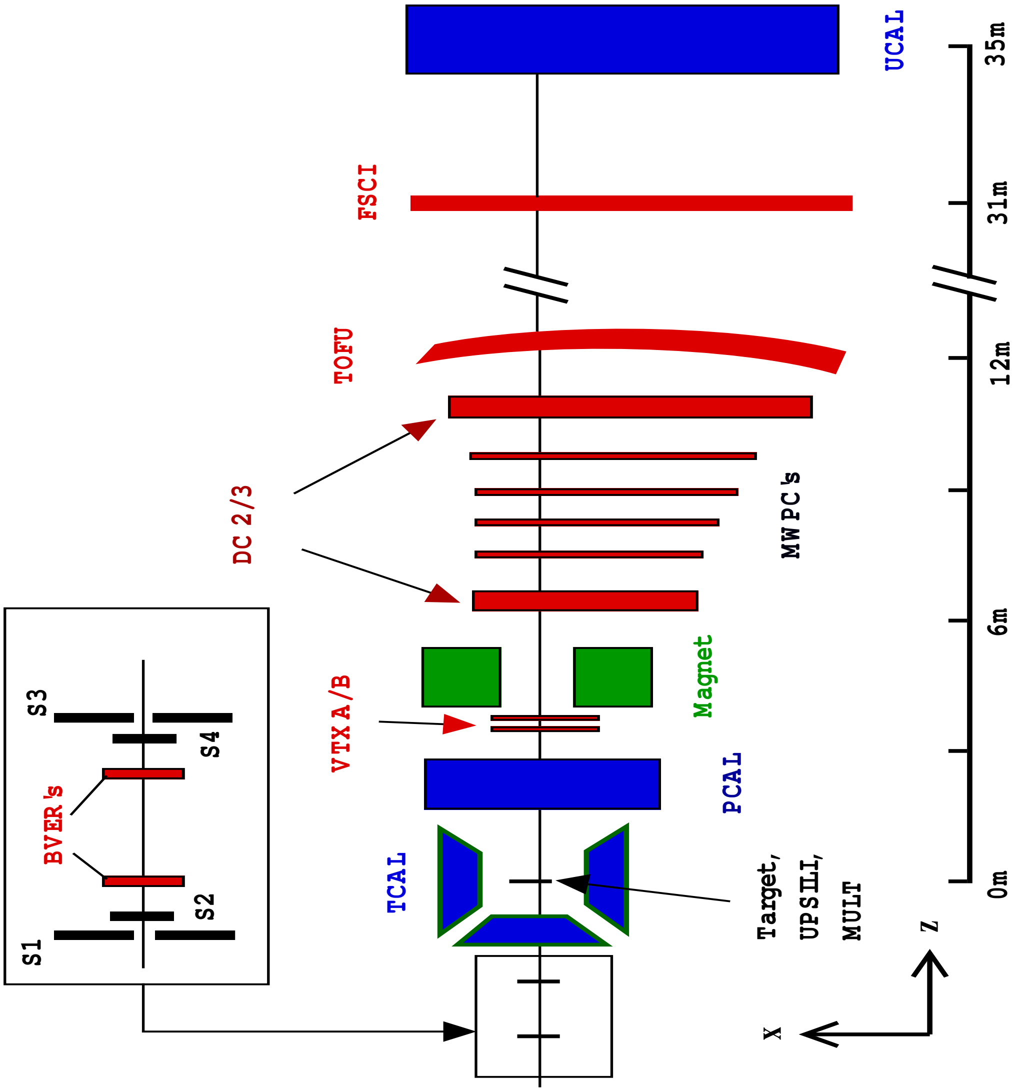

Figure 3.1: The E877 experimental setup, with all of its components and their approximate z location. Beam enters from the left of the page.

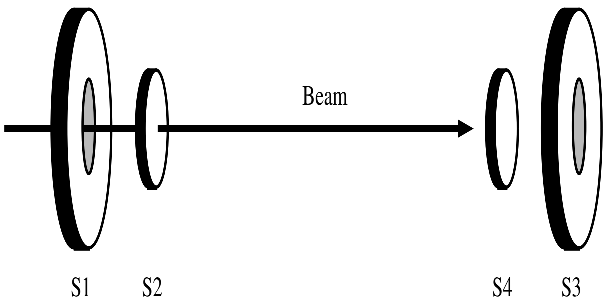

Figure 3.2: Two scintillation counters, replaced by Cherenkov counters in the 1995 run, and two veto counters to define a good beam particle and the start time of reference for the experiment.

- **The Beam Scintillator Counters (BSCIs)**: This group of detectors are made up of two scintillator counters and two veto counters, schematically drawn in Fig. 3.2. Due to increased beam intensity in the 1995 run, the two scintillator counters were replaced by two quartz Cherenkov counters to avoid radiation damage. A good beam particle is one that heads directly toward the target. Therefore it must strike $S2$ and $S4$ and "miss," or strike the holes of, $S1$ and $S3$. The beam logic is thus $(\bar{S}1 \cdot S2 \cdot \bar{S}3 \cdot S4)$. Fast rise time phototubes are connected to $S4$ to provide a high precision start time of reference for the experiment with a Gaussian width, σ, of $35 - 40$ *psec*. More details about the BSCIs can be found in Ref. [26] and [27].

- **The Beam Vertex Detectors (BVERs)**: The BSCI effectively restrict "valid" beam positions to the level of a few centimeters at the target. More accuracy is needed to determine the beam's position and direction. Between $S2$ and $S4$ are the BVERs, two $300\mu m$ thick silicon wafers each with $50\mu m$ pitch in the x axis. In the 1995 run, the BVERs were upgraded to double sided silicon wafers with $200\mu m$ pitch in both the x and y axes. ($\sigma_x = 300\mu m$ in 1994, $\sigma_x = 340\mu m$ and $\sigma_y = 340\mu m$ in 1995.)

- **The Upstream Silicon Detector (UPSILI):** The UPSILI is a thin Si detector placed just upstream of the target to measure the dE/dx of the beam particle. It has a unit charge resolution of Z=79 and is used to eliminate any beam particle that has an incorrect charge number due to Coulomb excitation or an interaction before striking the target.

All three sub-components have the ability to detect double beam events. A double beam event is when two beam particles arrive closer together in time than the experiment resolution. We cut on the maximum BSCI pulse height from $S2$ and $S4$, the maximum number of BVERs tracks, and the maximum dE/dx in the UPSILI. All of these will give a higher than normal value when a double beam event enters the detectors.

3.2.2 Event Characterization Detectors

An event can be characterized by the amount of overlapping region between the beam particle and the target during a collision. The amount of overlap is related to the impact parameter, $\vec{b}$, a vector that joins the center of

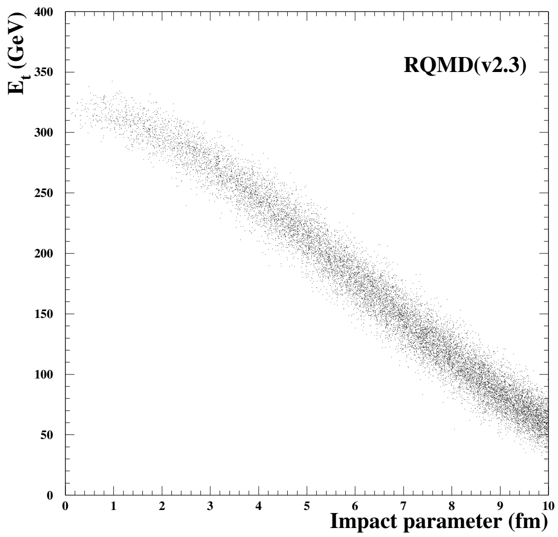

Figure 3.3: The correspondence between impact parameter and total transverse energy from RQMD(v2.3).

---

the beam particle to the center of the target particle at their point of closest approach. $\vec{b}$ is not, unfortunately, a direct observable. Using a model as a guide, we know there should be a strong anti-correlation of the collision violence with the impact parameter (see Fig. 3.3). Since the input energy of a collision is purely longitudinal, the total transverse energy [1] created in the collision is a gauge of the violence of the collision. We measure both the total transverse energy created in the collision and the azimuthal asymmetry of the transverse energy distribution to characterized our events using our calorimeters.

[1] $E_T = \sum E_i \sin\theta_i$ where the summation is over all particles; E_i is the i_{th} particle's energy; θ_i is the i_{th} particle's polar angle.

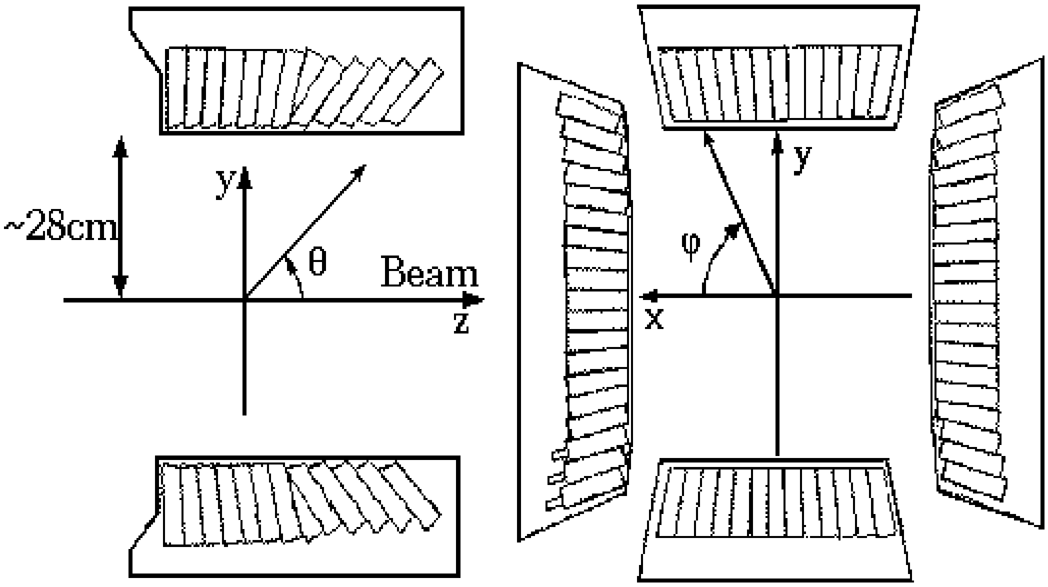

Figure 3.4: The target calorimeter in various views.

- **Target Calorimeter (TCAL)**: The TCAL, seen in Fig. 3.4, is composed of four walls of electromagnetic calorimeter surrounding the target completely in the azimuthal direction. The polar angle coverage is $48° < \theta_{lab} < 135°$ corresponding to a pseudorapidity coverage of $-0.5 < \eta < 0.8$. The walls are made up of an array of 832 NaI scintillating crystals. Each crystal is six radiation lengths deep. The signals from the crystals are read out with vacuum photodiodes. More details on the TCAL can be found in L.S. Waters' PhD thesis [28].

- **Participant Calorimeter (PCAL)**: The PCAL is a Pb-Fe scintillator sampling calorimeter with complete azimuthal coverage. It is located immediately after the TCAL. Its polar angle coverage is $1° < \theta < 47°$

corresponding to a psuedorapidity coverage of $0.83 < \eta < 4.7$. The PCAL is divided into two electromagnetic depths with ten radiation lengths each, and two hadronic depths with four hadronic interaction length each (iz =1,4 depth sections). It is further segmented into eight radial (ir =1,8) and 16 azimuthal sections ($i\phi$ =1,16) making a total of 512 cells in the whole device. Each cell is readout by wavelength shifting fibers guiding light to photomultiplier tubes (see Fig. 3.5). A full description of the detector can be found in Ref. [29, 30, 31].

- **Uranium Calorimeter (UCAL)**: The UCAL is the detector that is furthest downstream, approximately 35 meters from the target. Its purpose is to measure the energy of the forward particles, especially neutrons. The UCAL is a U-Fe scintillator sampling calorimeter with six hadronic interaction lengths. It is composed of 20 modules lined up horizontally perpendicular to the beam, and each module is segmented into 24 towers of 10x10 cm^2 cross sectional area. This results in an angular coverage relative to the target of $-5.2° < \theta_x < 1.3°$ and $-0.98° < \theta_y < 0.98°$. W.J. Llope's PhD thesis [32] provides more details on the UCAL.

Because the PCAL has a larger geometrical acceptance and less energy leakage than the TCAL, we use total transverse energy from the PCAL as the centrality tag. Both the PCAL and the TCAL, however, are used to determined the reaction plane angle of the collision. The UCAL is not used in the present analysis.

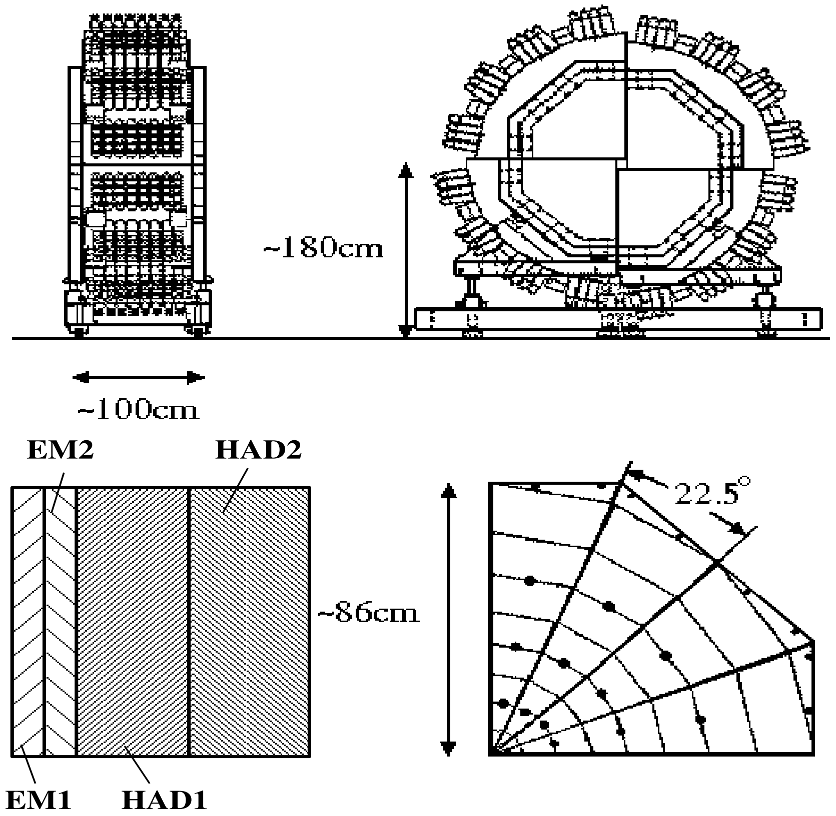

Figure 3.5: The participant calorimeter in various views.

3.2.3 The Forward Spectrometer

The forward spectrometer consists of detectors that work together to sort hit patterns into tracks and to measure quantities essential to derive the momentum and time of flight of each track.

- Collimator: The Collimator is located inside the PCAL opening in front of the magnet. It has an opening of $-115mrad < \theta_x < 15mrad$, and $-21mrad < \theta_y < 21mrad$. The collimator defines the acceptance of the forward spectrometer.

- Vertex Chambers (VTXA/B): Immediately after the PCAL and just in front of the magnet sit VTXA and VTXB, two highly segmented cathode pad detectors. Each vertex chamber consists of 20 anode wires strung along the x direction, 0.2 inch above a cathode plane of chevron shaped pads. A schematic of the pad plane is shown in Fig. 3.6. The x resolution is approximately $300\mu m$, and the y resolution is $2.54mm$, the spacing of the wires. More details of the VTXs can be found in R. Bersch's thesis [33]. The vertex chambers are used for confirmation that a track originates from the target. This is extremely useful to improve signal to noise ratio for rare particles such as K^+, K^-, and identifying secondary vertices of long lived resonances.

- Magnet: The dipole magnet has an opening comparable to that of the collimator. The magnetic field is set to 3,353 Gauss in the y direction for the 1994 run, bending positively charged particles into the -x direction.

Figure 3.6: The layout of the vertex chambers pad plane.

The field is reversed in the 1995 run, -3,353 Gauss in the y direction, bending positively charged particles in the +x direction. Since our forward spectrometer has most of its coverage in the -x direction, 1994 was the "positively charged particle run", and 1995 was the "negatively charged particle run".

- Drift Chambers (DC2/3): The drift chambers are made up of high resolution drift and low resolution pad detectors. The drift section consists of six parallel planes of alternating anode and cathode wires strung vertically. The drift planes are separated from one another by sheets of aluminized mylar. A schematic of a drift chamber is drawn in Fig. 3.7. The mylar and the cathode wires are held at negative voltage while the anodes are at ground potential. In addition, the drift planes are staggered relative to one another to resolve left right ambiguity of the avalanche. The signal from the anode wires provides time measurements, from which we can deduce the distance traveled by an avalanche, hence the position of the avalanche or track. The resolution, determined by the wire spacing (in the x direction), is $300\mu m$ in DC2 and $600\mu m$ in DC3. The seventh plane is the pad section. There the anode wires are held at high positive voltage while the cathode wires, the mylar, and the pads are held at ground. The back plane is composed of a chevron shaped pad circuit card, the pads running vertically along each anode wire. Relative image charge deposited on a pair of neighboring pads gives the y position measurement (along the anode wire) of the track. The chevron pad size varies to accommodate the high particle density and low particle density regions of the chambers; the y resolution thus ranges from 3 to $40mm$. A more comprehensive description of the DCs can be found in S.V. Green's Ph.D. thesis [34].

- Multiwire Proportional Chambers (MWPCs): The MWPCs are a set of four proportional wire chambers, the wires strung vertically, that are equipped with discriminator circuit readout only. The MWPCs are located between the two drift chambers as indicated in Fig. 3.1. Details on the MWPCs can be found in B. Hong's thesis [27]. The purpose of the MWPCs is to help with the pattern recognition. Due to the high multiplicity of tracks in heavy ion collisions, the combination of two sets of points measured in the DCs are not sufficient to unambiguously track. An additional four points from the MWPCs help confirm if the sets of points in the DCs match up to be a track.

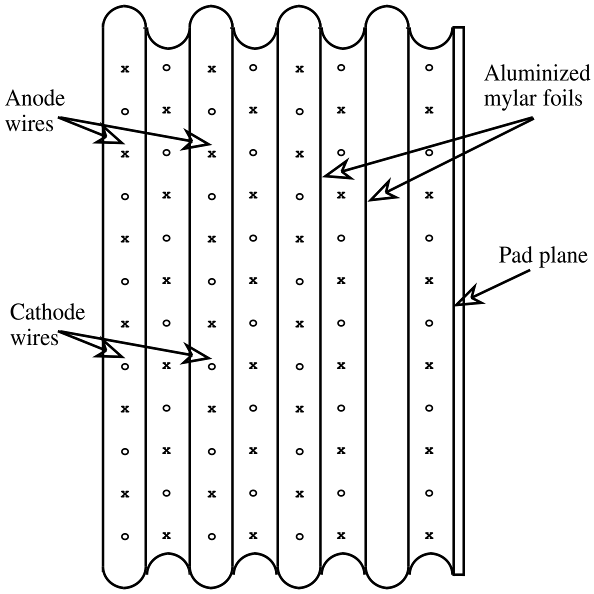

Figure 3.7: The drift planes and a cathode pad plane layout in the drift chambers.

- Time of Flight Hodoscope (TOFU): The TOFU is made up of 160 vertical scintallator slats that are staggered in z and overlapping by 10%. A phototube is mounted to both ends of each slat (top and bottom) to give a time of arrival and the y position of the track. The time resolution of TOFU is found to be $85psec$ and the y resolution is $1cm$. An average pulse height also tells us the charge of the track. A more thorough look at TOFU can be found in Ref. [35].

- Forward Scintillator (FSCI): The FSCI is another hodoscope wall placed far downstream ($30m$). It is consists of 39 10cm wide vertical plastic scintillator slats. It has a smaller coverage in phase space and its measurements are of a lower time resolution ($300psec$) than the TOFU. The FSCI provides a secondary measurement that can be used to improve particle identification and study of the TOFU systematics [36, 37], however, it is not used in the present analysis.

The E877 spectrometer is thus equipped to find tracks in high multiplicity heavy ion collisions, with higher position resolution in the x (bend) direction than in the y direction. The position of a track yields momentum of the track. With the time and pulse height measurements by the TOFU, we can deduce the mass and the charge of the track. The p_x and p_y resolutions are similar due to the fact that the mesurements in both directions are limited by multiple scattering. In this thesis we will select valid events using the beam definition detectors, sort the events via centrality and reaction plane angle measured by the calorimeters, and measure the correlation functions of charged particles identified by the forward spectrometer.

Chapter 4

Data Reduction

The digitized information from all detectors in each event is stored on 8mm data tape for later analysis. An event on tape is a self encoding archive. It begins with a header, indicating the beginning of an event. The header is followed by the beam definition detectors signals, the event detectors' signals, and the tracking detectors' signals. The self encoding refers to the fact that at the beginning of each major section is a word that tells the reader how many components in this section is to follow. For example, at the beginning of the event detectors section is a word that tells the reader that there are three detectors to follow. At the beginning of the first detector section is a word that tells the reader that there are 832 signals to follow. The 832 signals then come in 26 bundles of electronic modules (32 channels per ADC module). Each module has an identification word that associate it to the TCAL detector, that it holds ADC signals, that it is the i^{th} module in the chain of 26 modules, etc. This allows for ease of adding detectors to the data stream as E814 evolved into E877. Also, since the module identification fields were mask-coded for sub-system, module type, etc., this scheme allows for simple global analysis of common parameters such as pedestals for any ADC.

The information on tape are simply signals from TDCs and ADCs from all the detector channels. Even channels with no signal, except pedestal, are recorded. For a sophisticated experiment like E877 with its multitude of many channels detectors, the two month run in 1995 amounts to 1000GB of data written to 250 tapes. To analyze such an expanded form of data requires months for each pass of physics analysis. A procedure has been developed to reduce the raw data to a more compact and more immediately meaningful form. This procedure has thus been named STEP1. STEP1 is a large body of code that reads data from tape, calibrates the detectors' channels, and translates pulse heights into more meaningful quantities like momenta, positions, and times. This reduced form of data is then stored in ntuples, a database format developed by CERN program library. The 1000GB of raw data is reduced to 54GB of ntuples after a first pass through STEP1.

The ntuples, by design, contain redundant information as a safeguard against possible mistakes in some of the STEP1 calculations, or when unconventional analysis technique may emerge to study certain phenomema, without resorting to the raw data tapes. All information deemed the necessary (but redundant) is stored the ntuples. However the 54GB of data is still too large for daily analysis. To solve this we developed a second pass over the ntuples, STEP1.5. This step takes as its input the "fat" ntuples, and produces as its output "lean" ntuples. STEP1.5 recalibrates the detectors using their current calibration files (from the STEP1 scans) and also discretizes information that are used for cuts into simple yes/no for 1σ bit, 2σ bit, etc. Thus the "lean" ntuples contain only the necessary information for the current analyzes, and are truly "lean," totaling only 20GB, a factor of 50 reduction from the original size.

4.1 Calibration

Calibration needs to be performed detector by detector and channel by channel. E877 contained roughly 8000 channels in its final form. Calibration tasks are divided among the graduate students.[1] Automated procedures have the advantage that they can be used without human intervention. Procedures that are not automated require human monitoring and decision making and are more difficult and time consuming to use. Thus it is our goal to strive for 100% automated calibration procedures. We first succeeded in this goal during our last (1995) analysis.

4.1.1 Global Pedestals

A pedestal value for an ADC channel is the "zero" reading for that channel, i.e. the reading when there is no signal in the channel. If there is a signal in the ADC channel, the true signal is the signal minus the pedestal. However the pedestal value of any ADC channel may drift due to the turning on and off of external electrical noise and changes in the surrounding temperature, hu-

[1] Professors cannot be trusted with so many details :).

midity, etc. Therefore, pedestal values for all ADC channels must be evaluated regularly for the whole data taking period. In the past, it was the responsibility of the person in charge of each detector to construct a set of pedestal files for that detector for the whole run. But the process of determining a pedestal value of each ADC channel in the experiment can be determined indiscriminately of which detector the ADC channel belongs to. This indiscrimimation means that only one reading (and writing) subroutine is needed for all detectors, easing the maintainace of the STEP1 code. Additionally the process can be automated, freeing several graduate students' time so that they might solve other problems.[2]

For the 1994 and 1995 data set, pedestal values are collected over MT (empty - where there is no beam particle) events for all ADC channels. The fluctuation of the pedestal values is nearly Gaussian. Thus a collection of pedestal values for each ADC channel is fit to a Gaussian, with the fitted mean parameter being the pedestal value for that channel. Getting a good fit is crucial to the automation of the process. The fitting package we use is PAW [38], part of the CERN Libraries. PAW has automatic error bar assignment of $\sqrt{N}$, N being the bin content, which is valid for only large N. Bins with low counts should be assigned a Poisson error. For instance, bins with zero count should have a non-zero error bar (Poissonian) because the zero count is a measurement. If one assigns an error of zero to bins of zero count, then

[2]The author is irate that she alone did calibration on three times as many detectors for five times as much data as any of her predecessors :!.

it implies that no measurement was made there. PAW's automatic error bar assigments causes instability in the fits because a few outliers will cause the peak of the Gaussian to shift significantly. Once we identified the source of the fit instability, we bypassed the erroneous automatic error bar assignment of PAW (for low count bins) by assigning the error bars to each bin ourselves. Gaussian error bars are assigned to bins with $N > 20$ and for bins with $N \leq 20$, corresponding Poisson errors are assigned. Because Poisson errors are asymmetric, we take the larger of the two as the Poisson errors we assigned to our data. Global pedestals are determined twice a day, day and night time, for every day of data collection to allow for any drifts in their values. Global pedestals are determined before the scanning of raw data into ntuples.

4.1.2 PCAL

Calibrating the PCAL means gain equalizing the 512 phototubes such that a constant energy deposit in each of the segments will give the same energy reading from the corresponding phototubes.

Online

The PCAL is equipped with its own calibrating system with one 2.4 mCi ^{60}Co gamma ray source for each of the four quadrants (in the azimuthal plane). Let us recall the segmentation of the PCAL from Section 3.2.2 (with the aid of Fig. 4.1). Quadrant I contains all 8 radial and 4 depth sections in the $i\phi$ =1 to 4 sections; Quadrant II constains all 8 radial and 4 depth sections in the

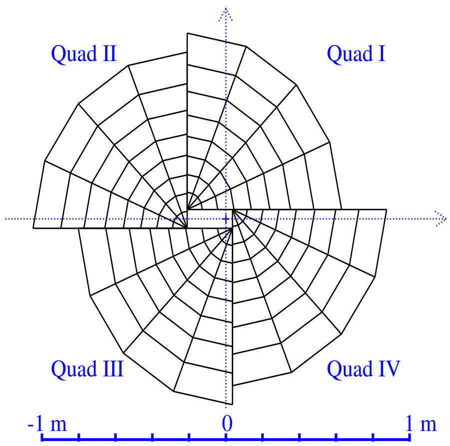

Figure 4.1: The segmentation of the PCAL (in the azimuthal plane), as viewed from downstream. Beam is coming out of the page, at the x and y cross hair intersection.

$i\phi$ =5 to 8 sections; Quadrant III contains all 8 radial and 4 depth sections in the $i\phi$ =9 to 12 sections; and Quadrant IV is in the $i\phi$ =13 to 16 area. The source is attached to a stainless steel cable running through the quadrants in a path that sequentially exposes the ir =2 to 8 towers. A steel cable is moved by a stepping motor and passes through a pulley attached to a shaft encoder, which allow us to ascertain the position of the source and know which tower's signal to be read out. The $ir = 1$ towers are read out (simultaneously with the $ir = 2$ towers) as the source passes the $ir = 2$ towers since the towers are smaller at smaller radii, there is significant energy leakage from $ir = 2$ to $ir = 1$ towers.

Historically, the calibration system of the PCAL was the least reliable system in all of E877. In the early years, the PCAL was calibrated once before and once after each data taking run. The reason for this "rare" calibration was that the system often lost track of the source position and had to be restarted. Typically two weeks were required to get four successful four-hour runs of the system (one run for each quadrant). The success of the PCAL source calibration degenerated as time passed because the responsibility was passed on from group to group. The blame was placed upon "slippage" of the motor-pulley system. For the last E877 run (1995), the author was placed in charge of the PCAL calibration.

We found that the five year old "slippage" theory was simply wrong. Instead, a number of electrical mis-designs were the real problem that prevented the proper function of the source PCAL calibration system. This problem is three-fold. First the position of the source is confused by "jitter" motion caused by the stepping motor. When stepping motors move very slowly, a step at a time, or move very fast, there are no "jitters." But during the ramping up (down) from a stable slow (fast) speed, there is a resonance frequency in which the stepping motor experiences near-zero torque. The "jitters" occur during this period. "Jitters" are literally when the motor moves one step backward and forward several times before proceeding in its original direction before the "jitters" occured. A schematic of this is drawn in Fig. 4.2 as a visual aid. During the "jitter" motion of the stepping motor, the shaft encoder loses counts. Therefore the position it reports back is inaccurate. To clear the confusion, we created a logic circuit that acts as a filter for the gray code readout from the shaft encoder. The filter allows for a change in direction in the counting of the shaft encoder only when there are two consecutive steps in that changed direction. Second, the signal from the filter (and the shaft encoder) is a TTL signal; it has a long line to travel into the counting house, where all the electronic signals are being processed. Any signal reflects when it travels in an unterminated line. Standard TTL signals cannot drive long line since they cannot drive long impedance. We converted the TTL into an ECL on the same circuit as the logic filter. Third, because the step of a stepping motor is on the order of mm and the size of the PCAL is on the order of m, the counts the shaft encoder reports back to us is geared down by a factor of 40; i.e. for every 40 steps the motor turns, the shaft encoder reported 1 step. We then need to multiply the signal from the shaft encoder by a factor of 40. This was done in a circuit box in the counting house that coverted the ECL signal back into TTL; and the TTL signal was then multiplied back up by generating a train of 40 pulses for each input pulse. This final output is then checked with the initial input - the steps that we instructed the motor to move originally - and they can be compare directly. With these improvements, the position of the source is known with great certainty, and "failed" runs were virtually eliminated.

The ^{60}Co signal from the phototube for each segment is integrated using a current monitor (CM). The CMs subsequently send their signals to ADC modules ($CM \rightarrow ADC$). There exist distinctive splittings of the quantity $\frac{CM}{ADC}$ for different (ir, iz) azimuthal slices when one runs the source through the PCAL. This is a consequence of the different sizes of the PCAL towers, i.e. the size is the same for all $i\phi$ for a particular set of (ir, iz). Since the ^{60}Co source

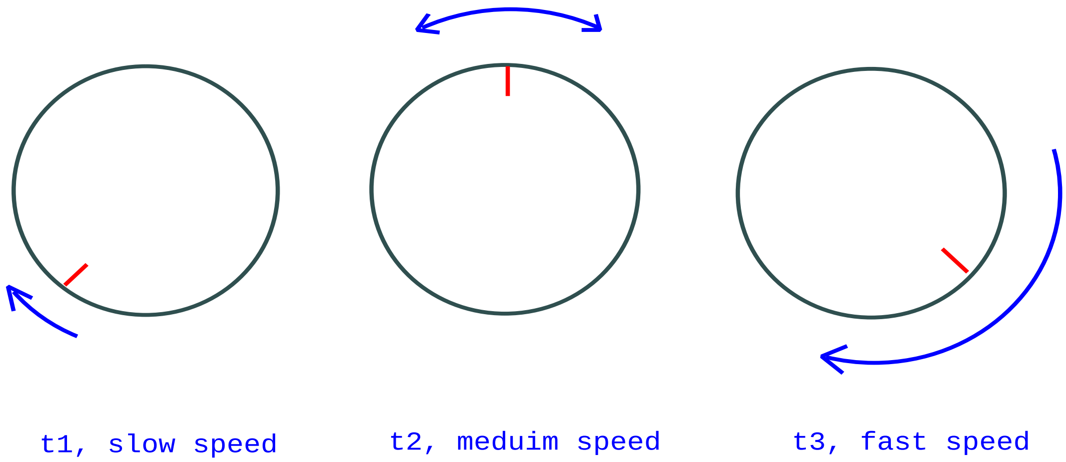

Figure 4.2: A cartoon showing motions of the stepping motor when it moves the radiative source through the PCAL during calibration. Left panel: at early time, t_1, the stepping motor moves at a stable slow speed. Middle panel: at t_2, where $t_1 < t_2 < t_3$, the motor is moving through a special frequency where it experiences near zero torque. The motion produced during this time is a "jitter"-ing motion. Right panel: at late time, t_3, the motor is moving as sufficiently high speed and is moving in only one direction now, the original direction at t_1.

emits a constant radiation as it passes through the PCAL, a smaller tower will detect only a fraction of that radiation while a larger tower will detect almost all of the radiation. The volume of the towers causes this distinctive splitting. But gain equalizing the phototubes means that there should not be a "volume" effect because the quantity $\frac{CM}{ADC}$ contains a "volume" factor in the numerator and the denominator; CM is integrated over the volume of the tower and ADC is also an integrated signal over the same volume. By requiring the $\frac{CM}{ADC}$ to be the same for all (ir, iz) we assign a CM_{target} for each (ir, iz) to make this so. Then for each calibration run, the CM of each phototube is required to match its corresponding CM_{target}. If $CM \neq CM_{target}$, the high voltage (hence the gain) is adjusted according to an empirical gain curve ($HV_{new} = HV_{old} + \frac{1}{k} log \frac{CM_{target}}{CM_{now}}$, $k = 0.00916$) so that the CM signal will match more closely to the CM_{target}.

Throughout the duration of the 1995 run, whenever the beam was not present, a PCAL source calibration was performed. New high voltages were then calculated from the CM readings to reached the corresponding CM_{target}s.

Offline

The set of CM_{target} from the online procedure gain equalizes only same size towers to one another. Gain equalize different size towers to one another requires knowledge of properties of each tower, such as volume, and shower containment and spread. This and putting the gains on an absolute energy scale are done in the offline procedure.

For each run after a ^{60}Co source calibration run, we compute a $\widetilde{ADC}_{target} =$

$\langle ADC \rangle \frac{CM_{target}}{CM}$ for each PCAL tower. $\langle ADC \rangle$ is the ADC value for that tower averaged over the upper 2% centrality events for that run (as determined by the TCAL since the PCAL is "not calibrated" yet). A Monte Carlo study of the PCAL, by Wen-Chen Chang [39], parametized collectively unknown properties for each tower. By imposing ϕ symmetry to the real external coordinate (r, z) and using the results of the Monte Carlo study, we do not need to know each tower's properties explicitly. We demand that $\frac{Par_{MonteCarlo}}{\widetilde{ADC}_{target}}|_{ir=i,iz} = \frac{Par_{MonteCarlo}}{\widetilde{ADC}_{target}}|_{ir=j,iz}$ for the same external coordinate r. Parameterizing $Ratio(r) = \frac{Par_{MonteCarlo}}{\widetilde{ADC}_{target}}(r)|_{iz=fix}$ then accounts for ϕ symmetry. The gain of the $(ir, i\phi, iz)$ phototube is then $\frac{ADC_{target}}{\langle ADC \rangle}$, where $ADC_{target} = \frac{Par_{MonteCarlo}(ir,i\phi,iz)}{Ratio(r(ir,i\phi,iz))}$. We now have gain equalized all the phototubes to one another.

To put this on an absolute energy scale, we need one more constant, γ that will make our $\frac{dN}{dE_{totalPCAL}}$ spectrum maximum at $350GeV$ as it should for the most central events. γ then is determined by trial and error and examining the $\frac{dN}{dE_{totalPCAL}}$ spectrum. Once it is determined, the gain of each phototube on an absolute scale is $\frac{ADC_{target}}{\langle ADC \rangle}\gamma$.

The short term drift of the phototube gains from run to run is taken into account by the so called n, n+1 method. For run n, $\langle ADC \rangle$ is stored for each phototube. In the subsequent run n+1, $\langle ADC \rangle$ is taken from previous run n to calculate the gain for the present run. We then monitor the gains from run to run. If there is a big shift from one run to another, then the present run n would need to be rescanned using its own $\langle ADC \rangle$ which has just been acquired to calculate the gains. But the PCAL phototubes are quite stable for all of 1995 data set that such rescanning due to a big shift in gains was never encountered.

4.1.3 Drift Chambers

The wires in the drift chambers measure drift times. A drift time is the time that the primary electrons take to move from the position of creation to avalanche. By assuming a constant electron drift velocity, the position of the charged particle that created the avalanche could be deduced. The drift chamber time to position calculation is done in two steps. First, because of electronic and cable delays, there exists offsets to all the times measured in all the channels (wires). These offsets are called t_0s. However since each wire has a similar time spectrum, the mean times are measured and aligned to one another, thereby correcting the delays. We fit a Gaussian to each wire's time spectrum, and then align the mean of all the wires' time spectra to the first wire's mean in that plane. Second, because the drift velocity is not constant for distances close to and far from the sense wire, the spectrum of drift time to the nearest wire integrated over all tracks is not flat. (Consequently the spatial distribution is not flat.) The non-flatness is a direct measure of the drift characteristics in the chamber. Instead of performing complicated studies and parameterizing the drift velocity, a much simpler method is developed [40]. The space to time relation is determined by transforming the non-flat time spectrum to a flat rectangular one, as one would have with a constant drift velocity scenerio:

$$\begin{aligned} d(x) &= \frac{x_{cell}}{2} w(t), \\ w(t) &= \frac{\int_0^t f(t')dt'}{A_{total}}, \end{aligned} \tag{4.1}$$

where $x_{cell} = 3175\mu m$ for DC2 and $6350\mu m$ for DC3; $f(t')$ is the time distribution to nearest wire for all tracks; and A_{total} is the integral of $f(t')$ over all measured time. The weight function, $w(t)$, gives the correct position of the charged particle, as if we have used a correct non-constant drift velocity. The disappearance of "wire structure" in the position spectrum and the improvement in the single wire resolution demonstrate the correctness of the technique. We calculate the $w(t)$ for each of the drift chamber planes. The calculation of the $w(t)$ is automated in the ntuple production and updated for each run employing the n, n+1 philosophy.

4.1.4 Pad Chambers

The y position of the charge particle that traversed through the DCs is measured by the pad chambers, the seventh plane of the DCs. Charge is induced in the 2-3 pads and "clusters" are formed. The position of the cluster tells us the position of the charged particle that induced the charge. Since the signal from each pad needs amplification prior to digitization, the gain of each amplifier need to be determined. A test pulser system was designed to calibrate the gain of each channel prior to each run period. Each channel is pulsed 20 times at 10 different amplitude test settings. The response of the

ADC channels was fit to a straight line. The slope is the gain factor for that channel's amplifier.

The centroid of the charge cluster can be calculated to first order by the charge weighted sum of two pads:

$$y(q_1, q_2) = \frac{q_1 \cdot y_1 + q_2 \cdot y_2}{q_1 + q_2}. \tag{4.2}$$

Because the shapes of the chevron pads were not ideal, we see a non-linear response from the chamber, i.e. we see a scalloping feature in periods of the pad size when integrating over all tracks' y positions deduced from Eq. 4.2. Using the same philosophy - dubbed "smoothy"- as the drift section's time to space relation (Sec. 4.1.3), we construct weight functions from the integrated y position spectra (different spectrum for different pad size regions). The scalloped y position spectra are then "smoothed" through the use of the weight functions. A before and after "smoothy" comparison of the y position spectrum for one pad size region in DC2 is shown in Fig. 4.3. The lack of significant structure at the pad edges validates the procedure.

The VTXs do not exhibit the same severity of non-linearity as the DCs due to design improvements in the pad shape. Therefore "smoothy" is not needed or used for the VTXs' measurements.

4.1.5 TOFU

TOFU measures the arrival and charge of the track by combining measurements from the top and bottom phototubes of a scintillator slat: $t_{track} = \frac{t_{top}+t_{bottom}}{2} - T_0$, $Q_{track} = \sqrt{Q_{top} \cdot Q_{bottom}}$. Q_{top} and Q_{bottom} are the pedestal

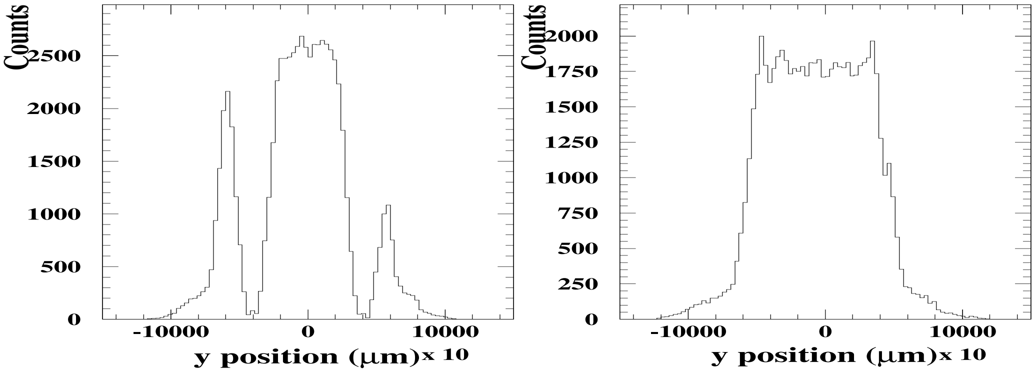

Figure 4.3: The left panel shows the y position spectrum before "smoothy" for one pad size region in DC2. The scallop feature indicates where the pad edges are. The right panel shows the y poisition spectrum after "smooth" for the same pad size region in DC2. The non-linear response of the chamber is eliminated.

subtracted pulse heights. T_0 is the time offset due to the properties of the scintillator and electronic and cable delays. T_0 is initially determined by examining the time of flight of high momentum π^-s. Since high momentum π^-s travel at nearly the speed of light, we can calculate the expected arrival times at TOFU from their measured path lengths. The difference between this and the measured time is the T_0. The initial T_0 is determined slat by slat for the first run. T_0 for the TOFU has been observed in previous years to drift significantly, thereby requiring constant monitoring and updating of the T_0 file. However, we want to follow the n, n+1 philosophy and automate the monitoring and updating procedure. The initial method of determining T_0 from π^-s requires human intervention because it is statistics bound and the fitting procedure is not always stable as a result. A more "blind" way is to examine the time distribution integrated over all tracks for each slat. This distribution, T_0 corrected, is well defined and should be constant with the right T_0 correction. Therefore, the difference between the mean of the $n = 2$ run and the mean of the $n = 1$ run of this distribution for a slat is a measure of the drift of this slat's T_0. A new T_0 is then calculated from this difference and saved to be used for the next n+1 run. This is an easier and non-statistics bound way of monitoring and correcting for shifts in T_0s that is automated. More details can be found in Y. Dai's thesis [41], the developer of this technique.

A second order effect should be noted concerning the TOFU. Because a time measurement is registered only when the pulse height passes some preset threshold, large pulse heights' time of arrival will be sooner than smaller pulse heights. A correct arrival time is when the pulse height is a fixed fraction of its peak height. This timing error, called slewing, is then inversely proportional to the pulse height. Thus an additive correction to the measured time is a factor:

$$\delta t_{slew} = \frac{\alpha}{Q_{top}} + \frac{\beta}{Q_{bottom}}. \tag{4.3}$$

The set of (α, β) is determined for each TOFU slat by minimizing the width of the peak in the time of flight error spectrum. This needed to be done only once for the whole run because these (α, β) do not change significantly over time.

4.2 Event Selection and Characterization

With well calibrated measured quantities in hand, we then need to characterize and select the events we are interested in studying.

4.2.1 Global Event Cuts

A good event is one in which there is only one beam particle colliding with the target producing a set of tracks. To ensure this, cuts are made on the signals of the beam definition detectors. The purpose of these cuts is to eliminate double beam and upstream or non-target interaction events. A typical BSCI pulse height spectrum shows a double hump, as in Fig. 4.4; the first hump corresponds to single beam particle and the second hump to double beam particles. The BSCI pulse height is then required to be of a typical value, consistent with the first hump. Double beam particles also make more than

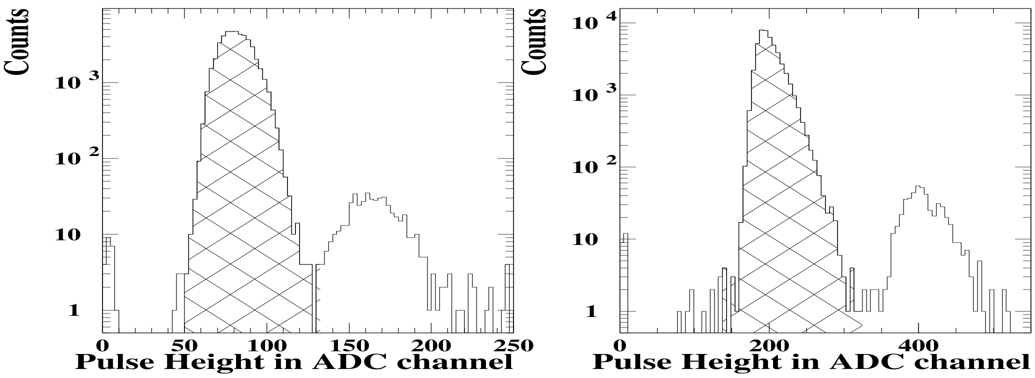

Figure 4.4: Typical pulse height spectrum from S2 (left panel) and S4 (right panel) of the BSCI. The hatch areas are defined as events with a single beam particle.

---

one clusters in the BVER. Thus the number of BVER cluster must be no more than one, see Fig. 4.5. In addition, the projected x, y, θ, and ϕ of the beam particle at the target as measured by the BVERs are also required to be in the typical range to ensure that the beam particle hit the target particle "head on," see Fig. 4.6. Finally in the forward spectrometer, extra beam particles that do not interact with the target usually produced a large multiplicity of δ rays which are detected in the MWPCs, DCs, and TOFU. As a safeguard against these "blast" events, the number of hits in the MWPCs are required not to exceed 40 for the event to be considered good, see Fig. 4.7. Individually, the good event cuts keep $\sim 90\% - 99\%$ of the total events that were saved; a detailed summary is given in Table 4.1. All the good event cuts combined, keep 84.6% of all events as good events.

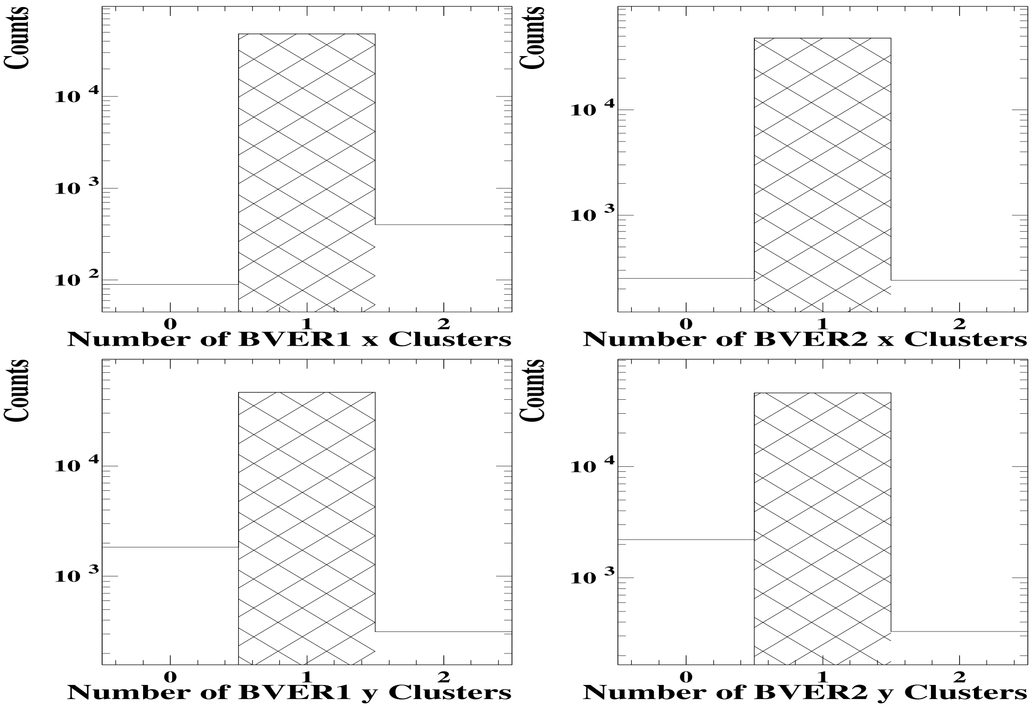

Figure 4.5: The number of BVER clusters in the x direction (top) and y direction (bottom). BVER1 is the left column and BVER2 is the right column. The hatch areas show the events that are accepted as single beam particle events.

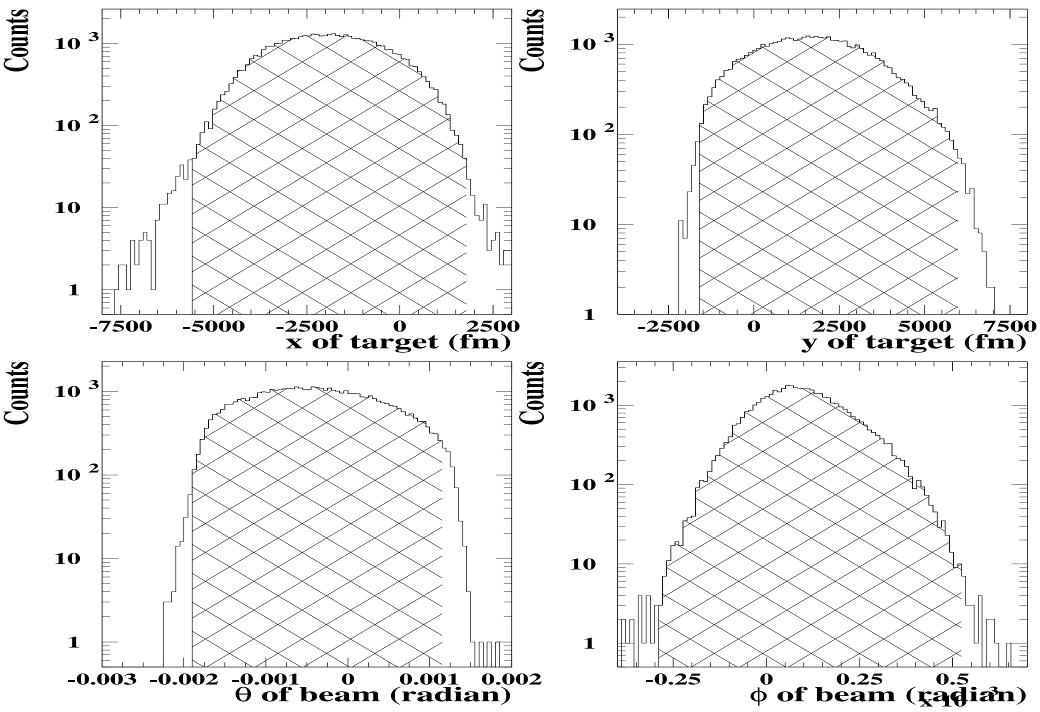

Figure 4.6: The projected x (top left), y (top right), θ (bottom left), and ϕ (bottom right) position of the beam particle at the target as measured by the BVERs. The hatched areas indicate “head on” interaction events.

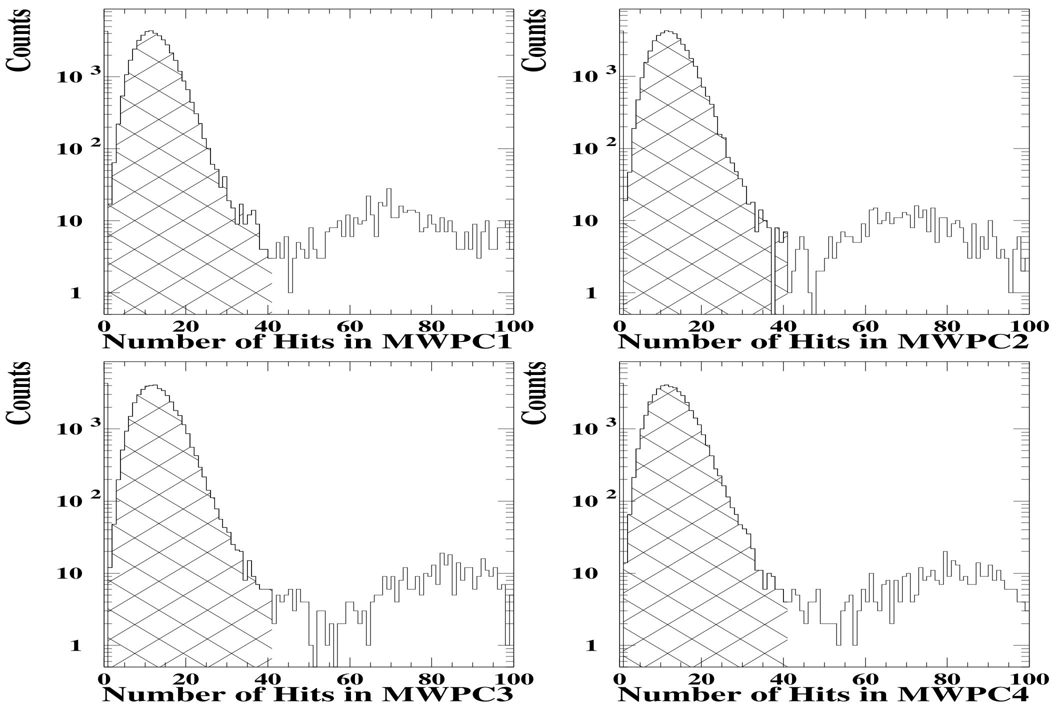

Figure 4.7: The number of hits in MWPC1 (top left), MWPC2 (top right), MWPC3 (bottom left), and MWPC4 (bottom right). The hatched areas indicate “non-blast” events, see text for explanation.

Cut	Good Events
BSCI S2	98.9%
BSCI S4	98.9%
BVER1 x	98.9%
BVER2 x	98.9%
BVER1 y	95.6%
BVER2 y	94.8%
x target	99.4%
y target	97.2%
θ beam	98.4%
ϕ beam	99.9%
MWPC1	90.1%
MWPC2	90.3%
MWPC3	90.4%
MWPC4	90.4%

Table 4.1: The percentages of events that made various single beam event definition cuts. See text for definition of the cuts.

4.2.2 Centrality Determination

Centrality is a measure of the violence of the collision and is defined in the following sense. The violence of a collision is measured by the amount of longitudinal energy (from the beam) converted to transverse energy (E_t). $E_t = \sum_{i=1}^{N} E_i \sin\theta_i = \sum_{i=1}^{N} E_t^i$, where E_i is the energy deposited in the i^{th} calorimeter segment, θ_i is the polar angle of the i^{th} segment relative to the beam axis, and the summation is over all segments. The PCAL and TCAL both measure E_t. The distribution $\frac{dN}{dE_t}$ is related to the $\frac{d\sigma}{dE_t}$ by:

$$\frac{d\sigma}{dE_t} = \frac{S}{\sigma_0 B P_{int}} \frac{dN}{dE_t} \tag{4.4}$$

where S is the trigger down scale factor, $\sigma_0 = \pi(2R_{Au})^2$, the geometric cross section, B is the number of beam particles, and $P_{int} = \sigma_0 \cdot Target_{density} \cdot Target_{thickness}$, the interaction probability of beam and target. Then

$$Centrality(E_t^0)\% = \frac{\int_{E_t^0}^{\infty} \frac{d\sigma}{dE_t} dE_t}{\sigma_0} \tag{4.5}$$

4.2.3 Reaction Plane Angle Determination

The reaction plane angle is defined by the azimuthal asymmetry of the E_t distribution event by event. Since our calorimeters have nearly 4π coverage, together they are not biased in measuring this asymmetry. The technique is based on a Fourier analysis [42] of the measured E_t. By defining:

$$\begin{aligned} a_n &= \frac{\sum_{i=1}^{N} E_t^i cos(n\phi_i)}{\sum_{i=1}^{N} E_t^i} \\ b_n &= \frac{\sum_{i=1}^{N} E_t^i sin(n\phi_i)}{\sum_{i=1}^{N} E_t^i} \\ \psi_{reac} &= arctan(\frac{b_1}{a_1}) \end{aligned} \tag{4.6}$$

The summation is over the segmentation of the calorimeter. ϕ_i is the azimuthal angle of the i_{th} segment as measured in the lab frame. This method would work perfectly well for an azimuthally symmetric device. The PCAL is an azimuthally symmetric device in its closed configuration but it loses this feature because it has an opening (to let more particles stream forward into the spectrometer), especially an asymmetric opening shown in Fig. 4.1. (The TCAL does not have this problem because it is a box around the target, hence azimuthally symmetric.) When we use Eq. 4.6 above, we find that the a_1 vs. b_1 distribution measured by the PCAL, averaged over many events, is neither centered around zero nor isotropic (the ψ_{reac} distribution is not flat), as it should be. A methodology was developed [42, 39] based on the philosophy that we know the peak of the a_1 vs b_1 distribution should be at zero and the ψ_{reac} should be flat. The distortions we see are characteristics of the device in which we use to make the measurement. Thus there exists a mathematical transformation that will take the distorted distribution and map it into a non-distorted distribution. This is essentially the "smoothy" philosophy first mentioned in Sec. 4.1.3 and 4.1.4, extended from one dimension to two dimension distributions. To reduce the instability and to minimize tweaking in the methodology, it helps to start with the least distorted a_1 vs b_1 distribution as we can construct from basic measurements. With the opening, the PCAL $(ir_{fix}, iz_{fix}, i\phi = 1, 16)$ is asymmetric, because the internal coordinates is asymmetric due to the opening. However we can force symmetry around the beam axis by freeing the internal coordinates and utilize the external coordinates, $(r_{lab}, \theta_{lab}, \phi_{lab})$ where r_{lab}, θ_{lab}, ϕ_{lab} are external coordinates that are measured relative to and around the beam axis. The PCAL is also divided into three pseudorapidity (η) windows (for resolution measurement), which is a function of θ_{lab} (and in a sense a function of iz). For the η windows, there exists sets of:

$$
\begin{aligned}
&(r_{lab} = 0, r_{max}, \theta_{lab} = \theta_{min}^{win1}, \theta_{max}^{win1}, \phi_{lab} = -\pi, \pi) \\
&(r_{lab} = 0, r_{max}, \theta_{lab} = \theta_{min}^{win2}, \theta_{max}^{win2}, \phi_{lab} = -\pi, \pi) \\
&(r_{lab} = 0, r_{max}, \theta_{lab} = \theta_{min}^{win3}, \theta_{max}^{win3}, \phi_{lab} = -\pi, \pi) \qquad (4.7)
\end{aligned}
$$

that are azimuthally symmetric. By grouping the segments into Eq. 4.7, we regain some of the lost symmetry; the a_1 vs b_1 distributions averaged over many events are centered closer to zero and are less anisotropic. Due to imperfections of the calorimeter, such as dead segments - the optical fibers guiding the light out to phototubes and/or the phototubes were damaged - and the finite extent of the PCAL, symmetry cannot be totally regained and the "smoothy" methodology is still necessary as a small correction.

A more detailed description of dealing with the properties of the calorimeters and the determination of the resolution of $\psi_{reac}(=30°)$ can be found in Ref. [39, 43].

4.3 Track Reconstruction

Tracks must be formed by associating hits in the chambers. The pattern recognition algorithm, named Quanah, is based on a road finding method in the x-z plane. First the hits in DC2 and DC3 are constructed into line "elements." For the hits to be grouped into reasonable line elements, the slope of the line elements must be within a range such that it is consistent with originating from the target without hitting the collimator and magnet edges. Each line element must be made up of at least three wires from three different planes. Neighboring elements are not allowed to share more than one hit wire. Next, elements in DC2 are connected with straight lines to elements in DC3. A line gets promoted to a "segment" if there are at least 3 MWPC hits along the line. The segments are allowed to share elements in DC2 or DC3.

The segments are promoted to "candidates" if they can be pointed back to the target without hitting detector edges. The candidates are then associated with clusters in TOFU and/or DC2 and/or DC3. A candidate must have a cluster in TOFU but not necessarily clusters in DC2 and DC3. The list of candidates are reordered to minimize sharing in the elements and clusters. Finally this new list of candidates then becomes "tracks."

This method of track finding fails when the occupancy in the spectrometer is too great. Because our spectrometer is a forward spectrometer, i.e. it detects only particles in a small forward opening angle, the occupancy for the detectors (DC2/3, MWPCs, TOFU) decreases with increasing centrality. To quantitively determine the threshold where Quanah becomes unreliable, we examine the number of hits in MWPC4 as a function of PCAL E_t and the number of tracks Quanah found as a function of PCAL E_t, shown in Fig. 4.8. As the number of hits in MWPC4 increases, the number of tracks that are really there (and found by Quanah) increases, until Quanah begins to fail. The turn over of the number of tracks found occurs around PCAL E_t of 150 GeV and hits in MWPC4 of about 20. We can further quantify Quanah's failure rate as the number of events in which Quanah gives up and reports 0 tracks found divided by the total number of all events. This failure rate is plotted as a function of PCAL E_t in Fig. 4.9. Thus we choose PCAL $E_t > 150$ GeV as the threshold for Quanah to start tracking, tolerating $< 5\%$ Quanah failure rate. The number of MWPC hits is almost always greater than the number of tracks found because some tracks pass through deadened regions in the DCs and MWPCs and are disqualified as tracks. The overall efficiency

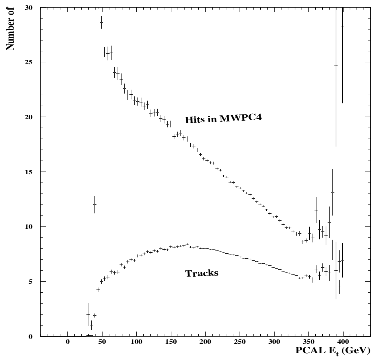

Figure 4.8: The number of hits in MWPC4 as a function of PCAL E_t and the number of tracks Quanah found as a function of PCAL E_t.

---

for finding an isolated track is $> 95\%$. The above track finding discussion has also been studied extensively in detailed simulations by Y. Kwon [36]. The results of the Monte Carlo are in agreement with our conclusion above.

4.3.1 Momentum Determination

Once the trajectory of a track is determined by Quanah, we can deduce its momentum. The claim of knowing the track's trajectory involves the assumptions that the track originates from the target and that the track follows a circular trajectory in the analyzing magnet. These assumptions are not unreasonable. The global event cuts and the collimator ensure that we are seeing reasonable reactions of beam particle impinging on the target. Our collimator also ensures that we are accepting particles that mostly traverse through the uniform area of the magnet field. Then, from the geometry in Fig. 4.10 we

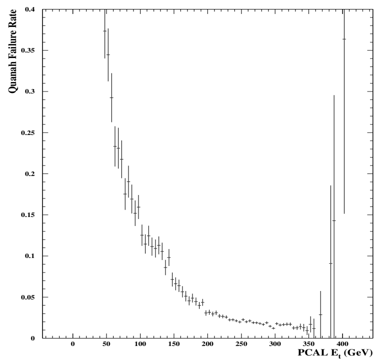

Figure 4.9: The failure rate of Quanah as a function of PCAL E_t is simply the ratio of those events which Quanah finds 0 tracks and all events.

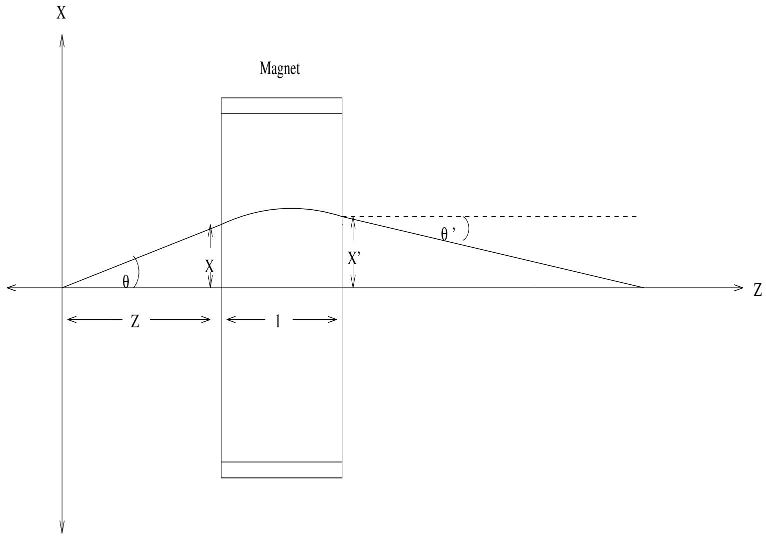

Figure 4.10: Bend plane geometry for a track in the E877 spectrometer

can see that:

$$R(sin\theta' - sin\theta) = -l \tag{4.8}$$

where R is the radius of curvature of in the bend (xz) plane; l is the *effective* length of the magnetic field (*effective* to account for the integral effects of the fringe fields at the magnet front and back face); θ and θ' are the entrance and exit angles of the track. The actual magnetic field was measured by S. Panitkin [49]. Comparison of exact field measurements and simple *effective* length estimates show that the error introduced in the approximation is negligible [44]. Thus for simplicity we choose to use the *effective* length estimates. Rigidity, p_{xz}/Z, then is:

$$\frac{p_{xz}}{Z} = \frac{\sqrt{p_x^2 + p_z^2}}{Z} = ReB \tag{4.9}$$

where Z is the charge of the track. The input from measurement is x' (which one uses to calculate θ'). The unknown is θ and consequently rigidity. The above set of equations are difficult to invert. Thus we first take a guess at $\theta_{guess} = x'/(z+l)$ and then propagate θ_{guess} to check x'. This is done iteratively by varying θ_{guess} slightly with each iteration until x' from the propagation differs less than $1\mu m$ from the x' measured. The check usually converges in under three iterations.

With p_{xz} known, p_x and p_z are trivially calculated and p_y follows as:

$$p_x = p_{xz}sin(\theta) \tag{4.10}$$

$$p_z = p_{xz}cos(\theta) \tag{4.11}$$

$$p_y = p_{xz}\frac{y_{TOFU}}{s} \tag{4.12}$$

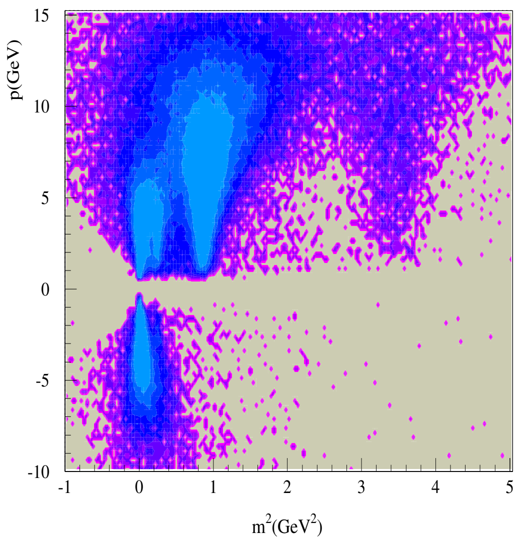

Figure 4.11: Momentum vs. $mass^2$

where y_{TOFU} is the y measured at TOFU and s is the path length traveled in the xz plane.

4.3.2 Particle Identification

A track becomes an identified particle when we calculate its $mass^2$, from its momentum and time of flight:

$$mass^2 = \frac{p^2}{(\beta\gamma)^2} = p^2 \cdot (\frac{1}{\beta^2} - 1) = p^2 \cdot ((\frac{tof}{t_{v=c}})^2 - 1) \tag{4.13}$$

where p is the momentum of the particle; tof is the time of flight of the particle; $t_{v=c}$ is the time a $v = c$ particle takes to traverse the same flight length. A plot of $mass^2$ vs. p is shown in Fig. 4.11. One can easily distinguish the different particles species. The features of the plot are not trivial and have been studied by Ref. [47], [40], and [46]. The low momentum limitation in particle identification is due to multiple scattering limiting our spectrometer's momentum resolution and the high momentum limitation is due to the finite time of flight resolution ($80psec$). Adding these resolutions in quadrature gives:

$$\sigma^2_{m^2} = 4m_0^4(\frac{\sigma_p}{p})^2 + 4\frac{p^4}{\beta}(\frac{\sigma_{tof}}{t_{v=c}})^2 \tag{4.14}$$

The time of flight resolution, σ_{tof} is assumed to be the same for all TOFU slats. The momentum resolution, σ_p, has two components. One component is due to the angular resolution of the spectrometer, and the other is due to multiple scattering in the spectrometer. These also add in quadrature.

$$(\frac{\sigma_p}{p})^2 = (\frac{\sigma_{p\theta}}{p})^2 + (\frac{\sigma_{pMS}}{p})^2 \tag{4.15}$$

$$(\frac{\sigma_p}{p})^2 = (C_1 p)^2 + (\frac{C_2}{\beta})^2 \tag{4.16}$$

Together then:

$$\sigma^2_{m^2} = 4m_0^4 p^2 C_1^2 + \frac{4m_0^4}{\beta_2}C_2^2 + 4\frac{p^4}{\beta}C_3^2 \tag{4.17}$$

where C_1 is related to the angular resolution; C_2 to the multiple scattering resolution; and C_3 to the time of flight resolution. Substituting $\beta_2 = \frac{p_2}{p_2+m_0^2}$, Eq. 4.17 then is purely a function of p:

$$\sigma^2_{m^2} = 4m_0^4 p^2 C_1^2 + 4m_0^4(1 + \frac{m_0^2}{p_2})C_2^2 + 4p^2(p^2 + m_0^2)C_3^2 \tag{4.18}$$

For each particle specie, we fit its $mass^2$ distribution to a Gaussian for a range of momentum slices. The widths of the Gaussians then are parameterized as a function of momentum according to Eq. 4.18. Protons give the most stable fit parameters, regardless of starting values of the fit parameters or a different data sample. This is only natural; protons are the heaviest particles that we detect in abundance. They are not statistics bound until the very high momentum where the proton sample is contaminated by the deuterons. The protons are also relatively "slow" and so do not run into the time of flight resolution limitation. Since we expect the same fit parameters for all particle species, we keep C_1 and C_2 fixed during the fitting procedure for π^+, π^-, K^+, and K^- to be the same as the proton values. For deuterons we keep only C_2 fixed in order to get reasonable C_3. From looking at the overlay of the fit function and the data points in Fig. 4.12 , we see that our fitting strategy does give good fits to the data. In addition, the fit parameters are in good agreement with those calculated from understood detector response [50]. The fit parameters are summarized in Table 4.2.

The standard particle identification for my analysis then is the following:

$$\begin{array}{lll}
\pi^+: & -1.5\sigma^2_{mass^2} < mass^2 < 1.5\sigma^2_{mass^2}; & p < 5.0 GeV; \\
\pi^-: & -1.5\sigma^2_{mass^2} < mass^2 < 1.5\sigma^2_{mass^2}; & p < 10. GeV; \\
K^+: & -1.0\sigma^2_{mass^2} < mass^2 < 2.0\sigma^2_{mass^2}; & p < 3.8 GeV; \\
K^-: & -1.0\sigma^2_{mass^2} < mass^2 < 2.0\sigma^2_{mass^2}; & p < 3.0 GeV; \\
proton: & -1.5\sigma^2_{mass^2} < mass^2 < 1.5\sigma^2_{mass^2}; & p < 10. GeV.
\end{array}$$

The maximum momentum cut off for each particle specie is to avoiding contamination from neighboring particle specie. It is estimated that with the above particle id, the contamination of a particle specie from neighboring particle species $< 2\%$ for pions and protons, $\sim 10\%$ for kaons. The acceptance of some of the identified particles in our spectrometer are shown in Fig. 4.13.

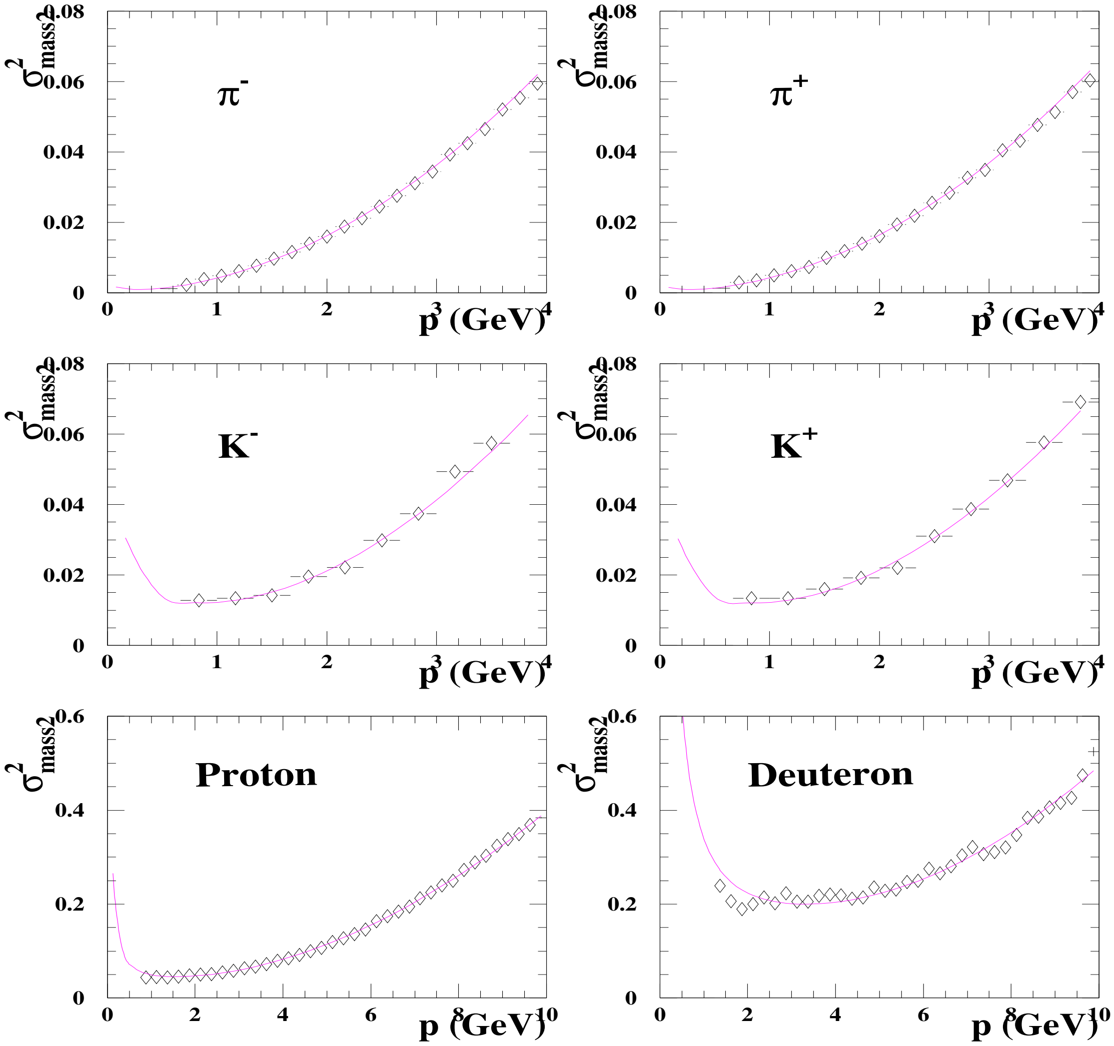

Figure 4.12: $\sigma^2_{mass^2}$ as a function of momentum for different particle species. The fit functions are overlaid on the data points. For the values of the fit parameters see Table 4.2.

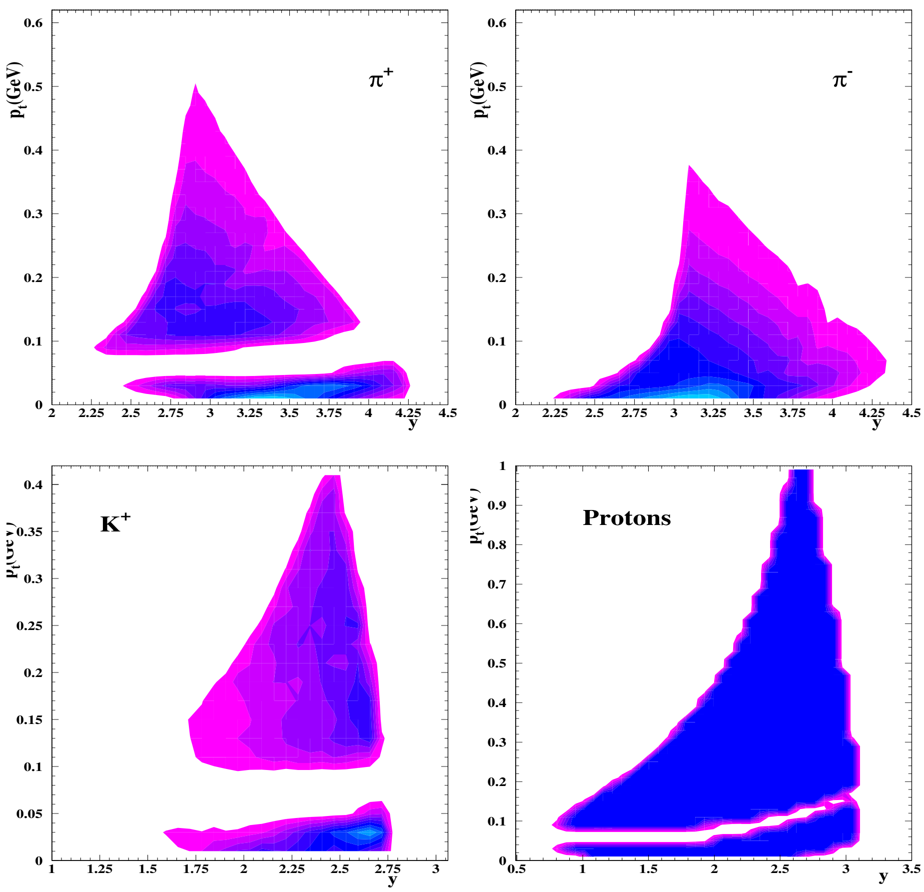

Figure 4.13: The acceptance of some of the identified particles in our spectrometer. The hole across the positively charged particles' acceptance is due to the deadened regions in the DCs.

	C_1^2	C_2^2	C_3^2
π^+	0.005704	0.02044	0.002051
π^-	0.005704	0.02044	0.002015
K^+	0.005704	0.02044	0.002197
K^-	0.005704	0.02044	0.002155
p	0.005704	0.02044	0.001909
d	0.002400	0.02333	0.002140

Table 4.2: Values of fit parameters characterizing the width of the $mass^2$ peaks for different particle species.

Background Cleanup with VTXs

Kaons are plagued with contamination from pions because the two particles' $mass^2$ are so close to one another and π^+s (π^-s) are created approximately five (ten) times more than K^+s (K^-s) in a typical collision. In addition to background from pions, another type of background around the kaons is from tracks whose momenta have been mismeasured due to the assumption that the tracks originated from the target. A requirement from the VTXs that

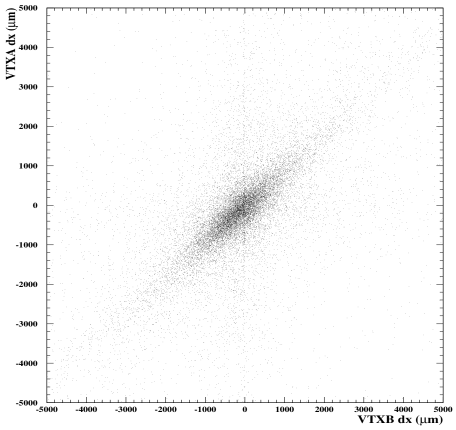

Figure 4.14: VTXA dx vs VTXB dx. There is a strong correlation between the two.

---

the track really originates from the target will reduced this type of background.

Hit clusters are formed in the VTX chambers during STEP1. Each track found by Quanah is looped through the VTX cluster list. The smallest residual, the difference between the calculated hit position of the track at the VTX chamber and the measured hit position, is saved as the VTX association for that track. The VTX chambers measure both x and y position of the hit clusters. But because the resolution in x is of the same order as the x resolution in the DCs, we find that it is useful to try to make cuts in only the x association of the tracks.

The VTXA dx versus the VTXB dx is plotted in Fig. 4.14. There is a correlation between the residual made in VTXA and the residual made in VTXB. To parameterize this correlation, we rotate the band from (dx_{VTXA}, dx_{VTXB})

to another set of orthogonal axes (dx_{narrow}, dx_{wide}):

$$dx_{narrow} = cos\theta dx_{VTXB} + sin\theta dx_{VTXA} \tag{4.19}$$

$$dx_{wide} = sin\theta dx_{VTXB} - cos\theta dx_{VTXA} \tag{4.20}$$

where θ is the rotation angle to make the band horizontal. θ is approximately $45°$, but not quite due to the physical displacement of the two chambers from one another in z. The narrow width is due to the intrinsic x resolution of the chambers because it does not have a strong momentum dependence. The wide width is due to the resolution as a result of multiple scattering and it exhibits a very strong momentum dependence. The dx_{narrow} and the dx_{wide} are divided into momentum slices. Each slice is then fitted to the sum of three different Gaussians. The tallest Gaussian is the true random distribution of error in correct track association. The other Gaussians are very flat and are only used in the fit so as to give a best fit of the tallest Gaussian. The widths of the tallest Gaussian are then parameterized as a function of $1/p$, typical momentum dependence of multiple scattering. The fit results are shown in Fig. 4.15. The fit parameters are:

$$\sigma_{narrow} = 199.7 + 1.67/p \tag{4.21}$$

$$\sigma_{wide} = 331.5 + 1358./p \tag{4.22}$$

Thus the x resolution of the chambers is $200\mu m$. We can rotate back to the (dx_{VTXA}, dx_{VTXB}) axes with:

$$\sigma_{VTXA} = (\sigma_{wide} sin\theta)^2 + (\sigma_{narrow} cos\theta)^2 \tag{4.23}$$

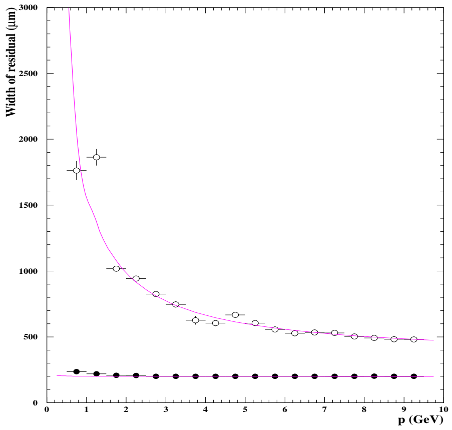

Figure 4.15: Fit results of the narrow (fill circle) and wide (open circle) components of the VTXA and VTXB correlation band. The nearly flat result of the narrow component indicated that this is the intrinsic resolution of the detectors, while the strongly $1/p$ dependent of the wide component indicates that it is caused by multiple scattering. The fit parameters are stated in the text.

$$\sigma_{VTXB} = (\sigma_{wide} cos\theta)^2 + (\sigma_{narrow} sin\theta)^2 \tag{4.24}$$

Then for any given track, with momentum p and a VTXA dx and a VTXB dx, we can calculate the σ_{VTXA} and σ_{VTXB} and make a decision to keep the track based on our tolerance of its VTX matching deviation. Because the two chambers are close together in z, and there exists some dead areas in both chambers, we choose to make an .OR. cut for any given track. An .OR. cut requires only information from one chamber to be good. This way we minimize throwing away tracks simply because they do not have good information in *both* chambers. By requiring a VTX chamber cut we do indeed lower the background around the kaon $mass^2$, as seen in Fig. 4.16 and Fig. 4.17. The plots are generated with an .OR. cut on the σ_{VTX}. Notice that some actual kaons are rejected in the process as well. Because the VTX chambers have a *deadened* region, purposely turned off because the beam goes through it, particles from this region a priori are rejected because they have *no* VTX information associated with them. There is also a region, same x-y extent, in both chambers that is dead, due to a dead wire. Particles from this region too, are rejected because they have not VTX information.

There is far less background in the positive particle $mass^2$ distribution in the 1995 run than in the 1994 run. See Fig. 4.18. The negative particle $mass^2$ distribution is unchanged. See Fig. 4.19. The thought of using the VTX chambers to clean up the kaon background started from the 1994 data set. But with the cleaner 1995 data set, not wanting to sacrifice statistics, we opted to not use the VTX cuts developed above for the analysis in this thesis.

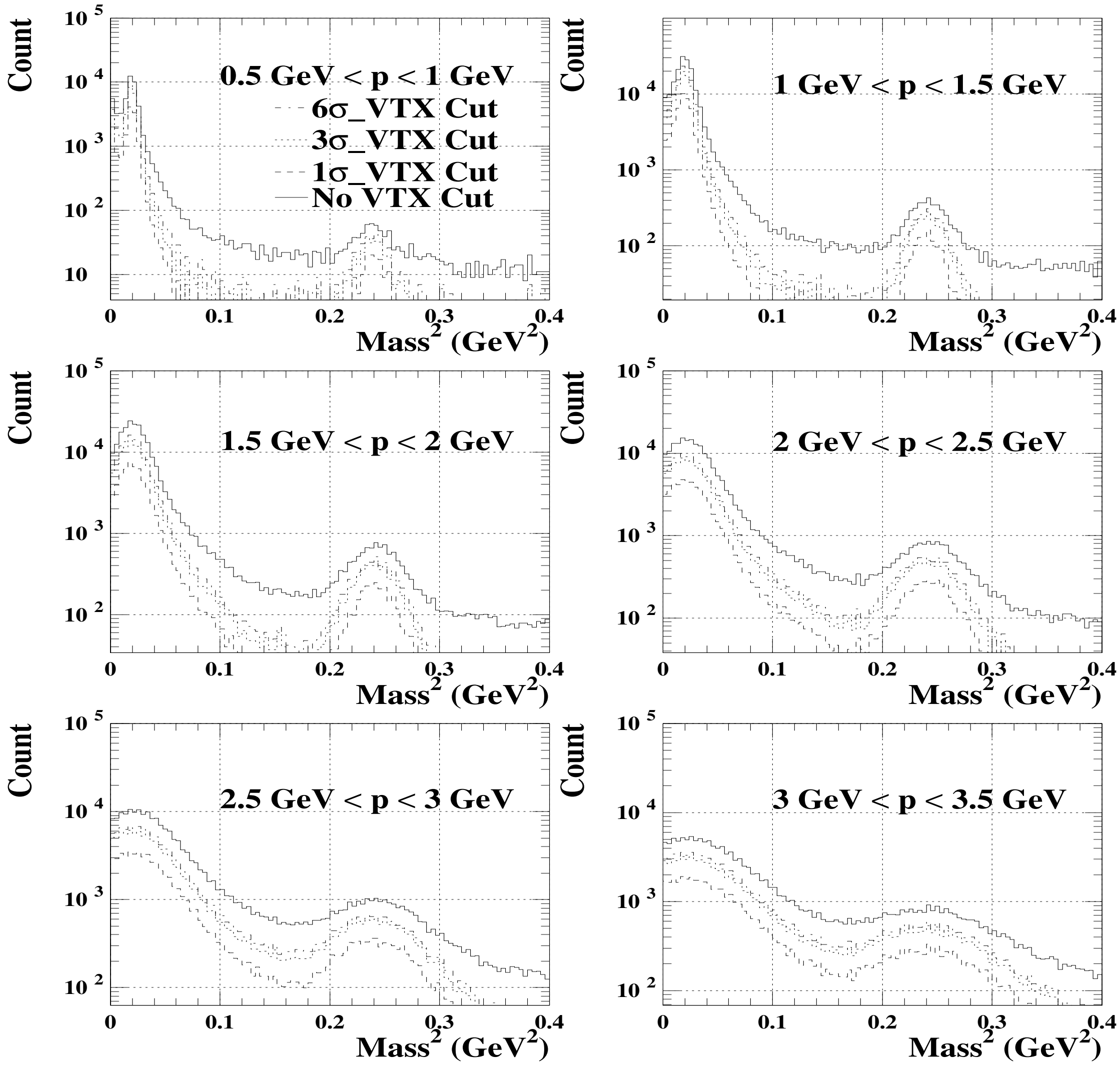

Figure 4.16: Different σ_{VTX} cuts $mass^2$ distribution for positively charged particles for different momentum slices. The $3\sigma_{VTX}$ and the $6\sigma_{VTX}$ cuts are virtually the same.

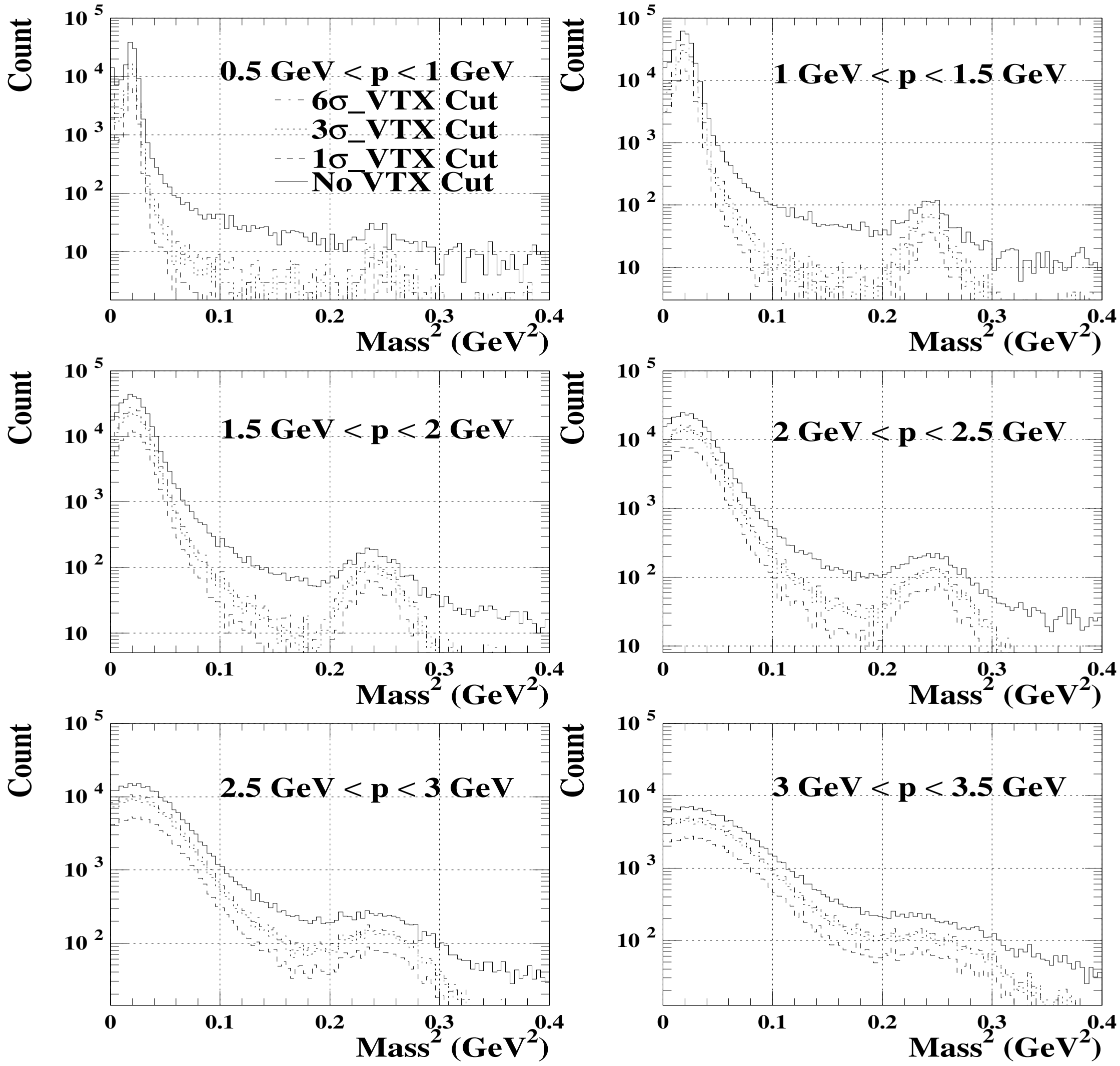

Figure 4.17: Different σ_{VTX} cuts $mass^2$ distribution for negatively charged particles for different momentum slices. The $3\sigma_{VTX}$ and the $6\sigma_{VTX}$ cuts are virtually the same.

With no VTX cuts, the 1995 K^+ sample contains $\sim 10\%$ background level.

4.3.3 Final Track Selection

Finally, for a track to be a good track of our desired specie, it must pass the spectrometer's fiducial cuts. These cuts are software cuts that reject any tracks that are too close to collimator edges, detector edges, detector deadened areas, and known bad/dead TOFU slats. A track's measured momentum is propagated forward using the single bend model, discussed in Sec. 4.3.1. At specific z coordinates of the collimator and the detectors, the x and y of the track is checked against a list of blacked-out regions. These edges and deadened areas have dramatically different and difficult efficiencies. Instead of making an intensive model study of these efficiencies, we opt for losing about 7% of all tracks by rejecting those tracks that do not make the cuts.

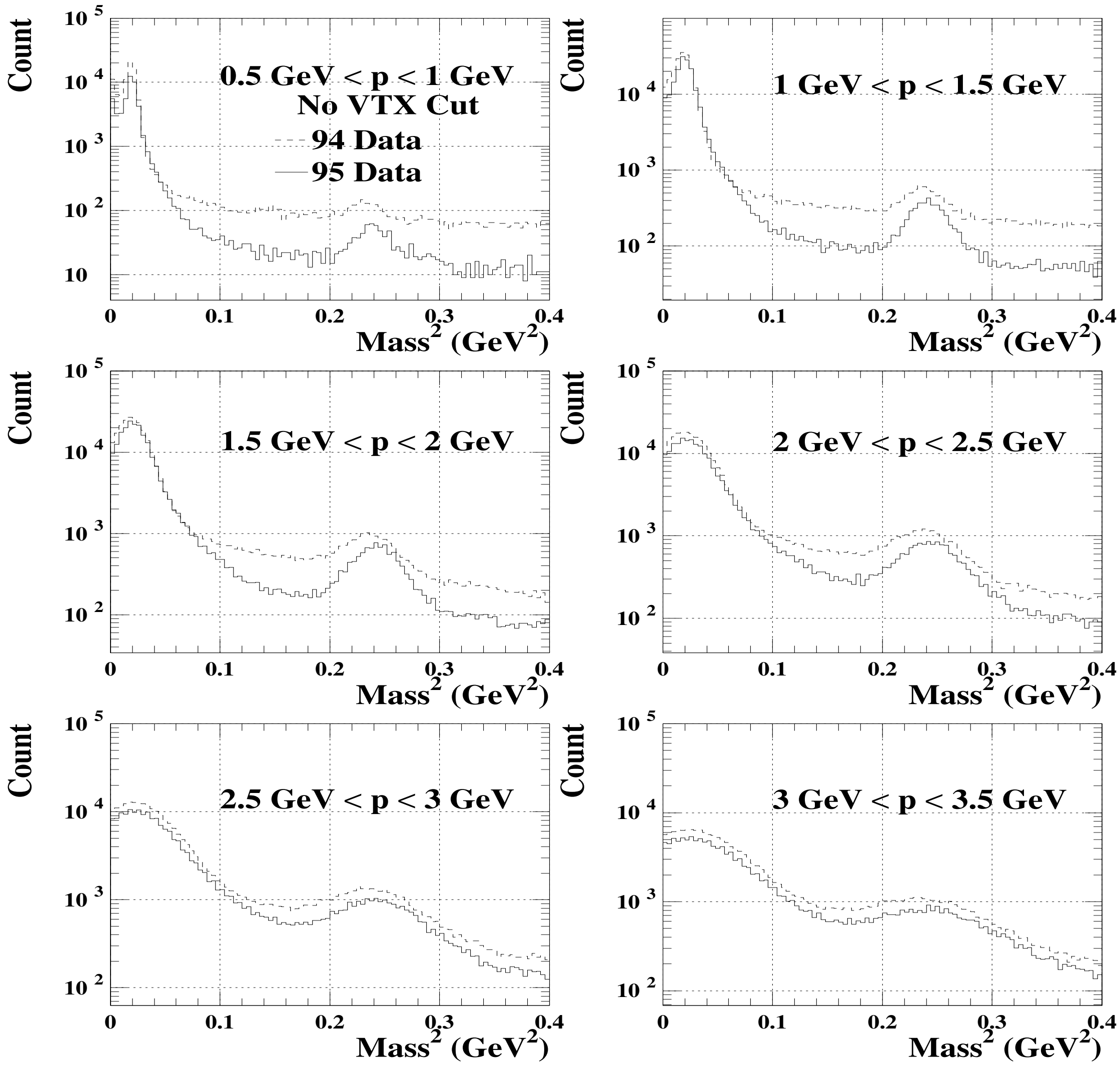

Figure 4.18: Overlay of 1994 with 1995 positive particles $mass^2$ distributions. There is far fewer background in the 1995 data set than the 1994.

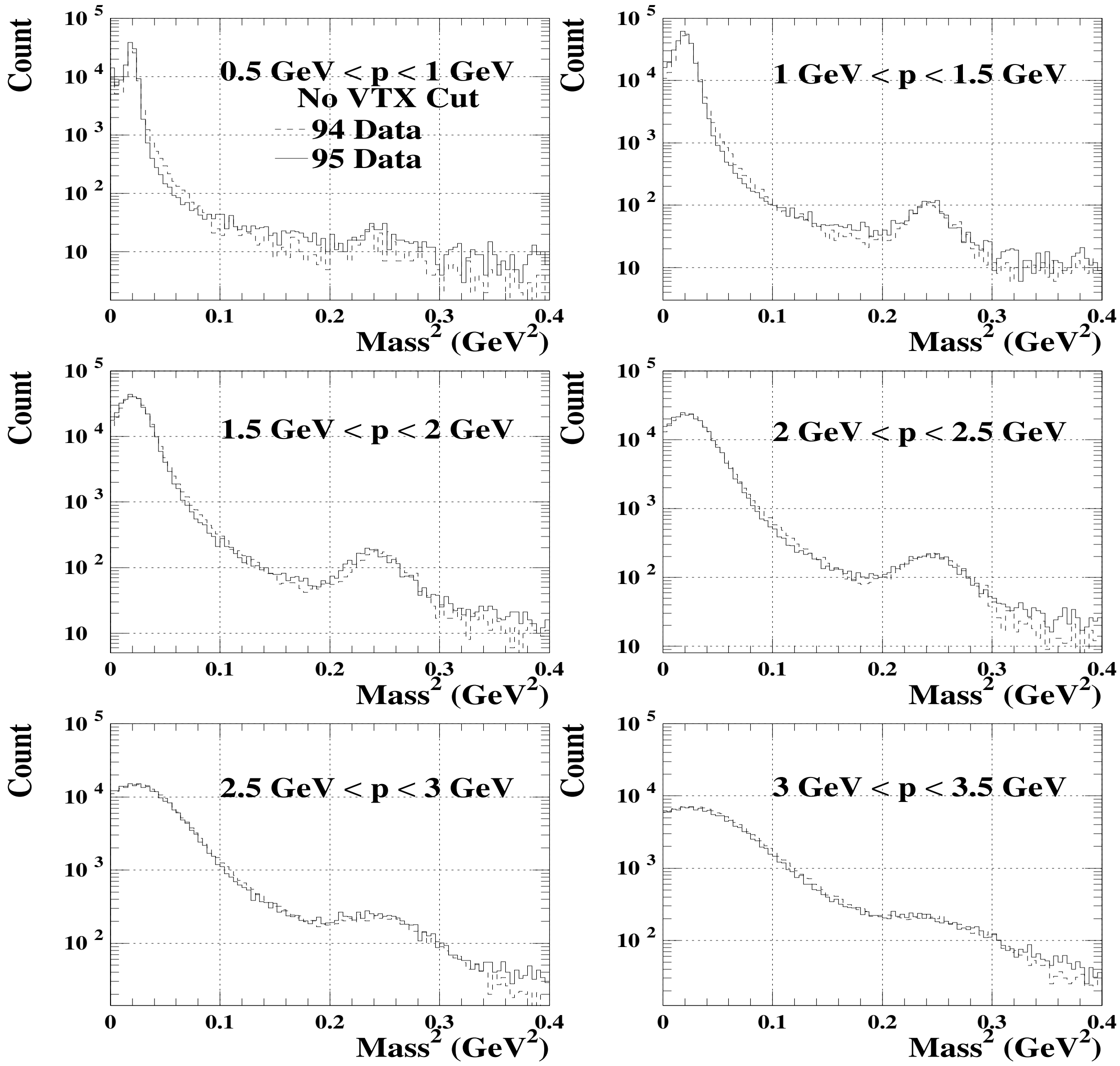

Figure 4.19: Overlay of 1994 with 1995 negative particles $mass^2$ distributions. The background level is about the same from 1994 to 1995.

Chapter 5

Measuring The Correlation Functions

The correlation function, C_2, is always measured the same way, regardless of particle species or global event selection cuts. Experimentally the definition of the correlation function is

$$C_2 = \frac{N_{true}(q_1 - q_2)}{N_{false}(q_1 - q_2)} Norm \tag{5.1}$$

where N_{true} is the count spectrum constructed of pairs from the same event while N_{false} is the count spectrum constructed of pairs from different events, via the event mixing method [48], and $Norm$ is the normalization constant that is fixed by requiring $C_2(large) = 1$. The variable of these spectra is $(q_1 - q_2)$, the momentum difference of the pair. The shape of the N_{true} spectrum is due to phase space, detector acceptance, detector response, and of course the correlation signal. The shape of the N_{false} spectrum is due to all but the correlations of the particle pairs. Thus dividing N_{true} by N_{false} we are canceling out the systematics of our measurement and isolating only the physics that causes true particle pairs to be correlated.

The statistical error of our measurement is dependent on the number of pairs in our N_{true} and N_{false} distributions:

$$\begin{aligned}
(\delta C_2)^2 &= \Big(\frac{\partial}{\partial N_{true}} C_2\Big)^2 + \Big(\frac{\partial}{\partial N_{false}} C_2\Big)^2 + \Big(\frac{\partial}{\partial Norm} C_2\Big)^2 \\
&= Norm^2\Big[\Big(\frac{\delta N_{true}}{N_{false}}\Big)^2 + \Big(\frac{-N_{true}}{N_{false}^2}\delta N_{false}\Big)^2\Big] + \Big(\frac{N_{true}}{N_{false}}\delta Norm\Big)^2 \\
\delta C_2 &= Norm\frac{N_{true}}{N_{false}}\sqrt{\Big(\frac{\delta N_{true}}{N_{true}}\Big)^2 + \Big(\frac{\delta N_{false}}{N_{false}}\Big)^2 + \Big(\frac{\delta Norm}{Norm}\Big)^2} \\
&= C_2\sqrt{\Big(\frac{\delta N_{true}}{N_{true}}\Big)^2 + \Big(\frac{\delta N_{false}}{N_{false}}\Big)^2 + \Big(\frac{\delta Norm}{Norm}\Big)^2}. \qquad (5.2)
\end{aligned}$$

The error in N_{false} is typically Gaussian error, $\sqrt{N_{false}}$ while the error in N_{true} is Poissonian for $(p_1 - p_2) \to 0$ and Gaussian for $(p_1 - p_2) \to \infty$. The error in $Norm$ is also typically Gaussian, $\sqrt{Norm}$, and is of the order of the number of false pairs. Then:

$$\delta C_2 = C_2\sqrt{\Big(\frac{\delta N_{true}}{N_{true}}\Big)^2 + \frac{1}{N_{false}} + \frac{1}{Norm}}. \qquad (5.3)$$

We can reduce our statistical error, and have it be dependent only on the number of true pairs, N_{true}, by mixing a very large number events to make our false pairs N_{false}, because the more events we "mix," the more false pairs that we get, a result from combinatorics. For $N_{false} \to \infty$ (and consequently $Norm \to \infty$):

$$\delta C_2 \approx C_2\sqrt{\Big(\frac{\delta N_{true}}{N_{true}}\Big)^2} \qquad (5.4)$$

This statistical error then reflects the real limitation of our apparatus and data set, because N_{true} is *the number of true pairs* that nature gave us during our data collection period.

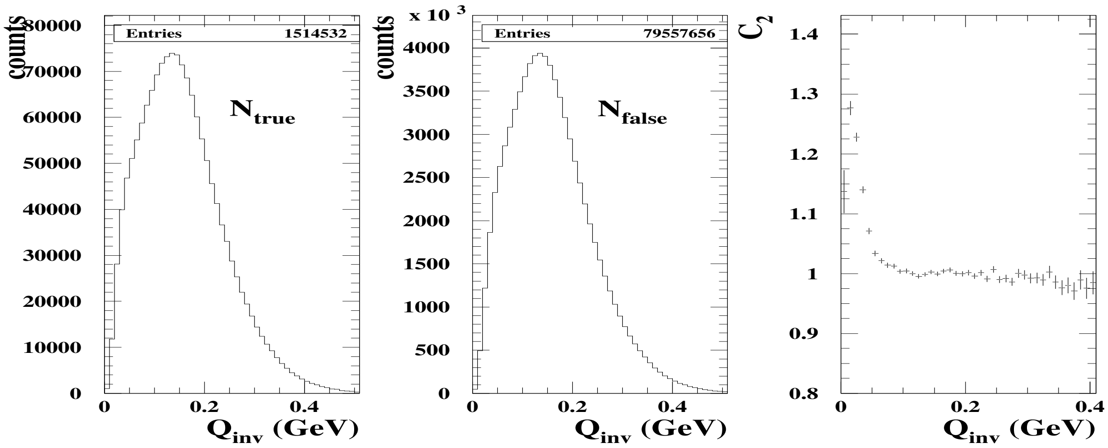

Figure 5.1: N_{true} and N_{false} have nearly the same shape except at very low Q_{inv}. This is clearly evident when we divide N_{true} by N_{false}.

Fig. 5.1 shows a sample of the N_{true} and N_{false} spectra. The two distributions look nearly the same. The drop at low Q_{inv} reflects both our spectrometer's limited ability to detect pairs of tracks that are close together in phase-space, i.e. the pairs that have nearly the same momentum. The fall off at high Q_{inv} reflects our track selection momentum cut off. For this particular particle specie, π^+s, we have a sharp track momentum cut off at 5 GeV, which translates to a gradual cut off in Q_{inv}. The physics that causes the true pairs to be correlated is evident when we divide the two distributions, as C_2 shows an excess of particle pairs near $Q_{inv} \approx 0$.

5.1 Two Close-By Tracks Inefficiency

We must be careful not to leave in any systematics of our apparatus when constructing the N_{true} and N_{false}. Our spectrometer has a limited capability to resolve two close-by tracks. This is an obvious consequence of the discrete wire spacing in the drift chambers. When two tracks are too close together spatially they will be identified as only one track. This point is clearly evident when we plot the separation in DC2 and DC3 for pairs of tracks, as in Fig. 5.2a and 5.3a. This inefficiency affects our N_{true} directly. But in the N_{false} distribution, since we construct pairs from different events, it is as if we have a different set of drift chambers for each track that makes up the pair. The inefficiency is not present in the N_{false}, see Fig. 5.2b and 5.3b. The simplest and most effective way of handling this inefficiency is to apply a minimum separation cut on each pair of tracks, regardless if the pair is a true pair or a false pair. We reject the pair of tracks if its spatial separation in DC2 $< 1.5cm$ or if its spatial separation in DC3 $< 3.0cm$. This way, we have a predictable inefficiency in the numerator, N_{true}, and we have the exact inefficiency in the denominator, N_{false}. The cut in pair separation space is sharp. But in q space, this cut is smeared out across small q. Therefore a sign of the miminum separation cut being applied to the N_{true} and N_{false} distributions is an overall reduction of low q pairs.

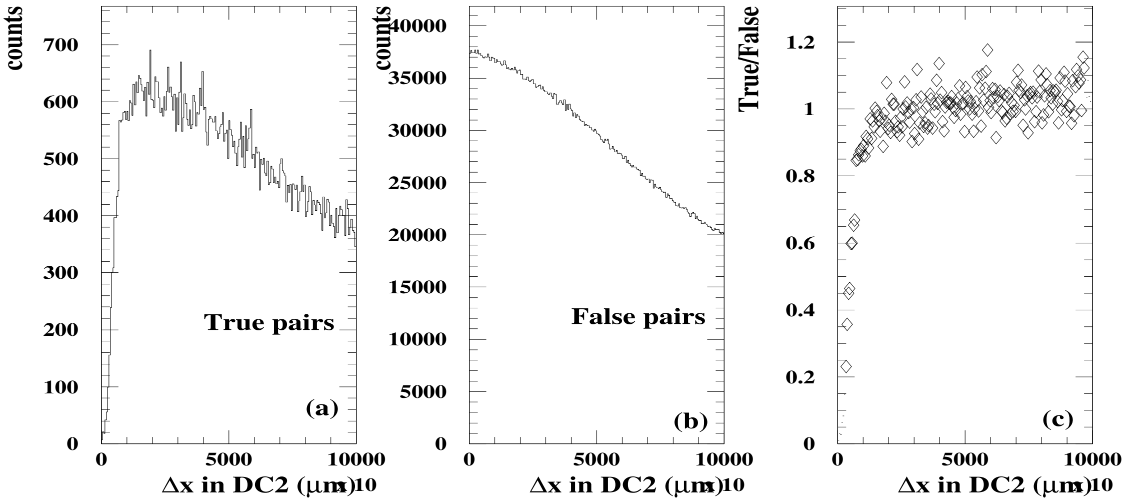

Figure 5.2: (a) Spatial separation for true pairs of tracks in DC2. (b) Spatial separation for false pairs of tracks in DC2. (c) The efficiency of detecting close-by tracks, or Fig. a/ Fig. b. The cut is a minimum spatial separation at least 1.5 cm in DC2.

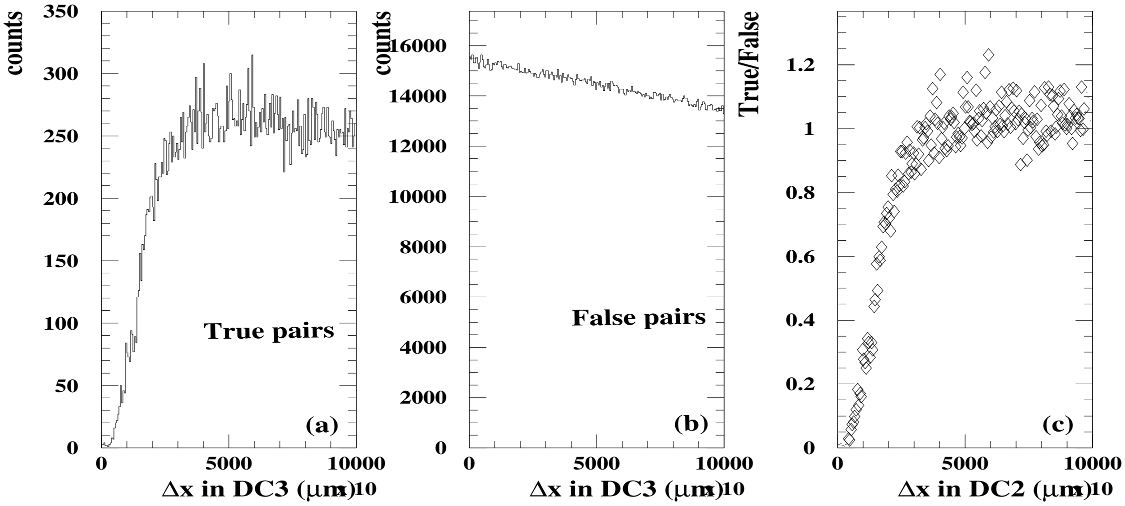

Figure 5.3: (a) Spatial separation for true pairs of tracks in DC3. (b) Spatial separation for false pairs of tracks in DC3. (c) The efficiency of detecting close-by tracks, or Fig. a/ Fig. b. The cut is a minimum spatial separation at least 3.0 cm in DC3.

5.2 Coulomb Correction

For π^+s, π^-s, and K^+s, we are interested in the Bose-Einstein nature of the particle pairs. Because these are not neutral particles however, a large distortion in their measured C_2 comes from their mutual Coulomb interaction with one another, i.e. the Coulomb repulsion one π^+ (π^-s or K^+) feels due to the presence of the other π^+ (π^-s or K^+) composing the pair. We thus want to remove the Coulomb interaction from our measured C_2. We can do this by weighing each false pair with a Coulomb factor that is calculated as though Coulomb were the only interaction of the particles. Presumably the true pairs intrinsically contain the same factor of Coulombic interaction. Thus the Coulomb factor in the numerator cancels with the one in the denominator of our C_2.

The Colomb interaction is greatest for particles that are close in phase-space to one another. Closeness in phase-space means closeness in momentum (and coordinate space); thus their motion relative to one another is non-relativistic. A system of two particles feeling each other's Coulomb fields can therefore be simplified to a system of one particle (with a reduced mass) in a central Coulomb field. This equation of motion is solvable and is worked out in many Quantum Mechanics textbooks. The solution and notation below are taken from Messiah [51].

The repulsive (since our case involves like sign particle pairs) trajectory of a particle traversing in a central Coulomb field is a Coulomb scattering wave whose amplitude is

$$| \Psi_c(\vec{k}, \vec{r}) |^2 = H(\vec{k}, \vec{r}) = \frac{2\pi\eta}{e^{2\pi\eta} - 1} \mid F(-i\eta; 1; ik(r - \frac{\vec{r} \cdot \vec{k}}{k})) \mid^2, \tag{5.5}$$

where:

$$\vec{k} = \frac{\vec{p_1} - \vec{p_2}}{2}; \quad \vec{r} = \vec{r_1} - \vec{r_2}; \tag{5.6}$$

$$\eta = \frac{m\alpha Z_1 Z_2}{Q_{inv}}; \quad Q_{inv} = \sqrt{-(p_1^\mu - p_2^\mu)^2}; \tag{5.7}$$

$$F(a; b; c) = \sum_{n=0}^{\infty} \frac{\Gamma(a+n)\Gamma(b)}{\Gamma(a)\Gamma(b+n)} \cdot \frac{c^n}{n!}. \tag{5.8}$$

If the relative separation between the particles is zero, $\vec{r} = 0$, then

$$H(\vec{k}, 0) = G(Q_{inv}) = \frac{2\pi\eta}{e^{2\pi\eta} - 1} \tag{5.9}$$

reduces to the Gamow factor. The Gamow factor is only an approximation as it is unphysical to have the relative separation between the particles to be zero. A more correct factor is to assume some separation between the particle pairs, after all this is what our C_2 is trying to measure. To first order, assuming a Gaussian source distribution, H in Eq. 5.5 can be averaged to obtain a more correct factor:

$$\frac{\int_{-\infty}^{+\infty} e^{-r^2/2R^2} H(\vec{k}, \vec{r}) d^3r}{\int_{-\infty}^{+\infty} e^{-r^2/2R^2} d^3r} \tag{5.10}$$

where $R^2 = R_1^2 + R_2^2 = 2R_0^2$ and R_0 is the Gaussian radius of the particle source distribution. Eq. 5.10 is called the extended source Coulomb correction factor.

Technically, to be absolutely correct, Eq. 5.5 when applied to a system of two bosons (that are close in phase space) must be symmetrized with respect to particle exchange [59]. The symmetrized version of Eq. 5.5 will greatly increase the complexity and computational time of the numerical integration of Eq. 5.10. However Eq. 5.10 has been shown to be a very good numerical approximation to the symmetrized version [52]. (At RHIC, where the number of pions in the system will increase, this approximation may be too crude. A symmetrized Eq. 5.5 may be necessary to calculate the extended source Coulomb correction factor.)

Since knowledge of the source size is necessary to correct for the Coulumb interaction in the measured C_2 (which tells us the source size), we are lead to an iterative procedure: measure C_2, extract a source size, measure C_2 again with a extended source size (that was just extracted) Coulomb correction factor, extract a source size, etc., until the extracted source size matches the input source size in the Coulomb factor. A simpler way is to measure C_2 with a variety of extended source Coulomb factors. Then find a match of input source size for the Coulomb factor and the extracted source size from the C_2, as illustrated in Fig. 5.4. The Coulomb factors are calculated once for a variety of input source sizes (for π pairs and K pairs) and stored as look up tables. The tables are then searched for a corresponding Coulomb factor for each false pair constructed with a given Q_{inv}. We limit our granularity of input source size to $1fm$ because Coulomb corrections of better than $1fm$ resolution do not affect our result significantly as compared to its statistical error.

In Fig. 5.5 we plot the Coulomb factors as a function of Q_{inv} for different input source sizes for pion and kaon pairs. The more correct extended Coulomb factor is even more crucial for higher particle masses, like the kaons, as seen in the figure. The extracted source size of Ks C_2 differ by more than 10% when one switches from a Gamow factor correction (input source size $= 0fm$) to an

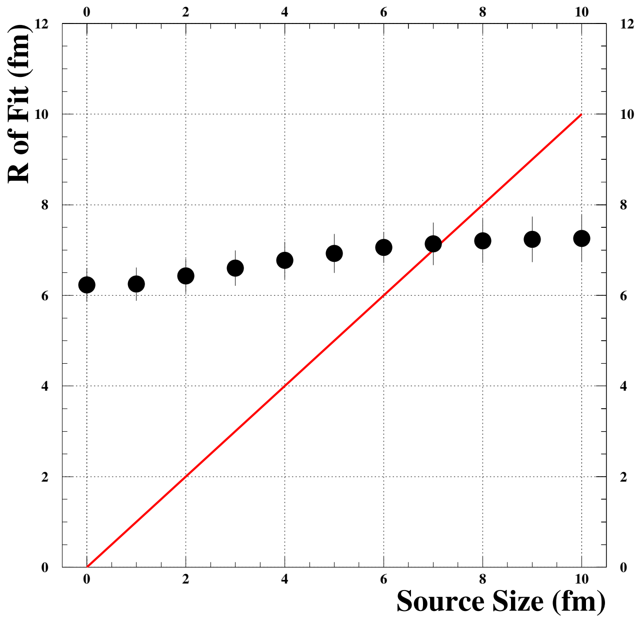

Figure 5.4: “Iterative” procedure of finding a match between input source size of the Coulomb factor and extracted source size of the measured C_2. For this particular example, an input source size of $7fm$ best matches the extracted source size of the measured C_2.

extended source size (input source size $\neq 0fm$) Coulomb correction. Thus it is important, particularly for Ks, to use the extended source Coulomb correction since it is a more accurate description.

5.3 Fitting C_2

As mentioned earlier in Chapter 2, we must fit our data to extract the source size parameters. The conventional fitting method is usually the least square method, derived from assuming a Gaussian distribution of the measured data points. But for C_2, because of the two close-by tracks inefficiency and simple phase-space considerations (Sec. 5.1), we have a depletion of data at low q, where the signal is. This depletion of data at low q follows Poisson, instead of Gaussian, statistics. Therefore the least squares method is not appropriate for fitting our measured C_2. An alternative fitting method, the maximum likelihood method, is instead employed. The maximum likelihood is equivalent to the least squares fit if one approximates the Poisson distribution that describes the data by a Gaussian distribution [53]. Our measurement is made up of bins of $C_2(n_i, N_i)$ where n_i and N_i are the number of true and false pairs in the i^{th} bin. The attempt is to try to find the best set of parameters $\vec{A}$ to describe the data such that $C_2(n_i, N_i) \equiv C_{2i}(\vec{A})$. For each bin the mean number of true pairs can be described by the set of parameters $\vec{A}$:

$$\bar{n}_i = C_{2i}(\vec{A})N_i \tag{5.11}$$

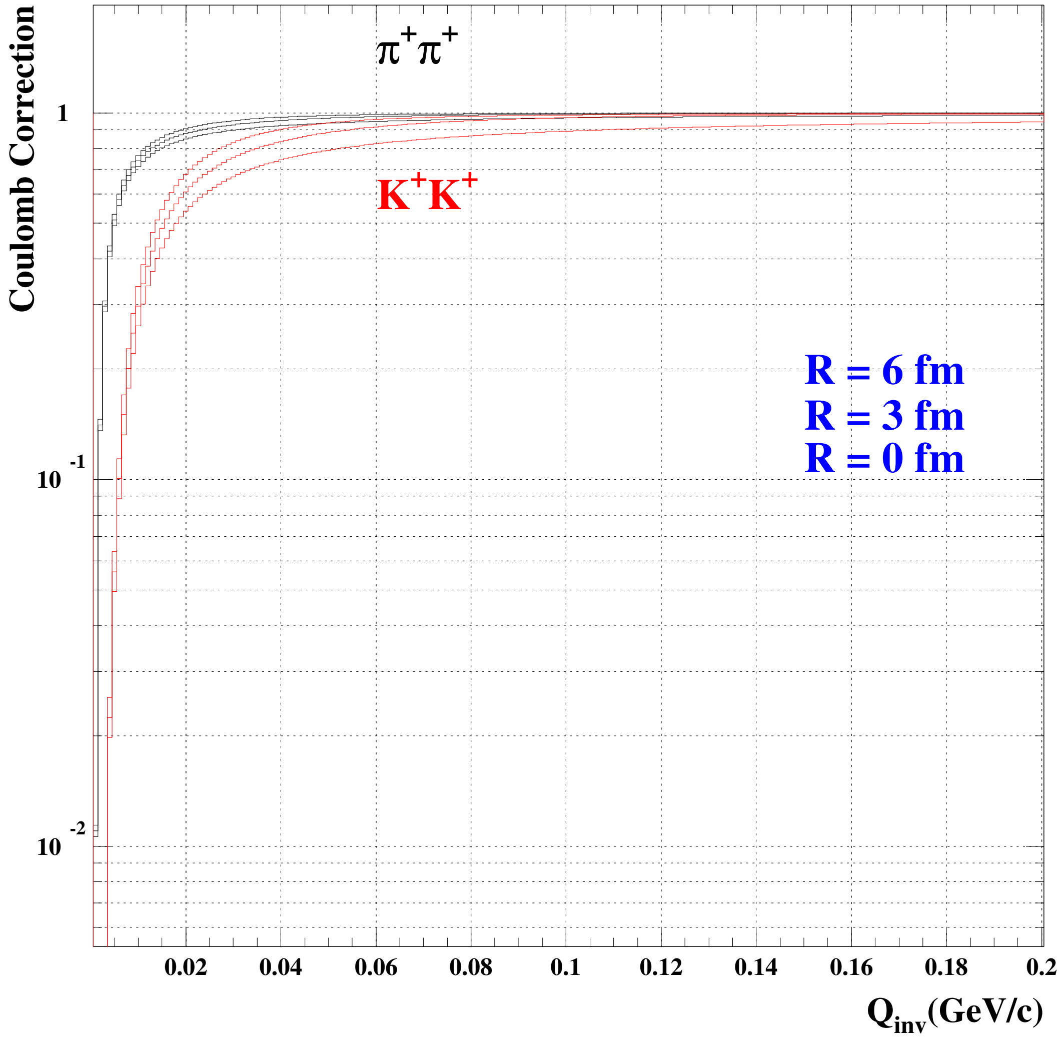

Figure 5.5: The Coulomb factor for $\pi^+\pi^+$ and K^+K^+ pairs. The upper set of three lines are corrections for $\pi^+\pi^+$ and the lower set are corrections for K^+K^+. The upper, middle, and lower lines of each set is the correction for Coulomb source size of 6 fm, 3 fm, and a point like source, respectively.

where $C_{2i}(\vec{A})$ is the hypothesized C_{2i}. Then the Poisson probability of measuring n_i true pairs is:

$$P(n_i; N_i, \vec{A}) = \frac{(C_{2i}(\vec{A})N_i)^{n_i}}{n_i!} e^{-C_{2i}(\vec{A})N_i} \tag{5.12}$$

The likelihood function is therefore the product of the i^{th} bin probabilities:

$$\mathcal{L}(\vec{A}) = \Pi_i P(n_i; N_i, \vec{A}). \tag{5.13}$$

The set of $\vec{A}$ that maximizes Eq. 5.13 is the best fit to the data. Or equivalently we can minimize the negative of Eq. 5.13. Because each P_i tends to be small, the product of many small numbers that make up the likelihood function will be even smaller. To avoid running into a precision problem of comparing two very small numbers (in the minimization process), we minimize the negative logarithm of the likelihood function instead:

$$\begin{aligned} -ln\mathcal{L}(\vec{A}) &= -ln(\Pi_i P(n_i; N_i, \vec{A})), \\ &= \sum_i C_{2i}N_i - n_i ln(C_{2i}N_i) + ln(n_i!). \end{aligned} \tag{5.14}$$

Since the last term in Eq. 5.14 is independent of $\vec{A}$, it can be dropped during the minimization process. The minimization is done via a CERN package called MINUIT [54]. The two methods of fitting, the least squares and the maximum likelihood, are equivalent for large n_i because there Poissonian and Gaussian distributions are indistinguishable. Since there is a correspondence between Eq. 5.14 and χ^2 of the least squares method [53, 54], namely:

$$\chi^2(\vec{A}) = -2ln(\mathcal{L}(\vec{A})) + constant, \tag{5.15}$$

we therefore, strictly speaking, minimize $-2ln(\mathcal{L}(\vec{A}))$ to find a set of best fit parameters $\vec{A}$.

5.4 Fit Functions for C_2

There are numererous forms of the function to which we can fit the measured C_2. We will state all that are used in this thesis here.

Ideally we would like to measure a six dimensional $C_2(\vec{q}, \vec{K})$. This procedure is impossible with today's limited statistics data sets. To combat this difficulty we can integrate or coarsely bin some of the coordinates. We will do both in this thesis. We will measure C_2 for the integrated range of $\vec{K}$. Additionally we will cut narrow windows of $\vec{K}$ ranges and measure C_2s in these windows (Sec. 6.3). As discussed in Chapter 2 there are two three dimensional parameterizations that one can construct C_2 in and fit to. The first is the BP parameterization. The three axes of C_2 in this parameterization are q_o, q_s, and q_l. The second parameterization is the YKP parameterization. The three axes of this are $q_\perp$, $q_{||}$,and $q_\emptyset$. The two parameterizations are connected in that $q_\perp = \sqrt{q_o^2 + q_s^2}$, $q_{||} = q_l$, and $q_\emptyset$ is not rewritten by Eq. 2.23. There are explicit relations connecting the two parameterizations, see Eq. 2.43. With the BP parameterization we can reduced it to two dimensions by grouping $Q_\perp = \sqrt{q_o^2 + q_s^2}$ and keeping $Q_l = q_l$. One last step to further improve the look of the C_2 is to reduced it to one dimension. In 1D, all the components of q are collapsed together to form $Q_{inv} = \sqrt{q_\emptyset^2 - \vec{q}^2}$. Please note that with the same data set, we are in effect diluting C_2 the more dimensions we go to. The disadvantage in this is that we are spreading the signal thin. The advantage, however, is that we are forming a more detailed picture of the signal. The functions to fit C_2 to is summarized below.

$$3D \quad BP \quad C_2(q_o, q_s, q_l) = 1 + \lambda e^{-R_o^2 q_o^2 - R_s^2 q_s^2 - R_l^2 q_l^2 - 2R_{ol}^2 q_o q_l} \tag{5.16}$$

dependent variables $(q_o, q_s, q_l) \rightarrow$ fit parameters $(\lambda, R_o, R_s, R_l, R_{ol}^2)$

$$YKP \quad C_2(q_\perp, q_{||}, q_\emptyset) = 1 + \lambda e^{-R_\perp^2 q_\perp^2 - R_{||}^2 \gamma^2 (q_{||} - v q_\emptyset)^2 - \Delta\tau^2 \gamma^2 (q_\emptyset - v q_{||})^2} \tag{5.17}$$

dependent variables $(q_\perp, q_{||}, q_\emptyset) \rightarrow$ fit parameters $(\lambda, R_\perp, R_{||}, \Delta\tau, v)$

$$2D \quad C_2(Q_\perp, Q_l) = 1 + \lambda e^{-R_T^2 Q_T^2 - R_L^2 Q_L^2} \tag{5.18}$$

dependent variables $(Q_T, Q_L) \rightarrow$ fit parameters (λ, R_T, R_L)

$$1D \quad C_2(Q_{inv}) = 1 + \lambda e^{-R_{inv}^2 Q_{inv}^2} \tag{5.19}$$

dependent variable $(Q_{inv}) \rightarrow$ fit parameters (λ, R_{inv})

5.5 RQMD Correlation Functions

Relativistic Quantum Molecular Dynamics (RQMD) [55] is a semi-classical cascade model that collides particles together and follow their propagation through stochastic interactions. The initial particles form color strings and hadronic resonances which in turn are excited through elementary collisions. The final produced particles are created from the fragmentation and decays of these strings and resonances. RQMD has been successful in reproducing data to first order, i.e. in terms of single particle spectras [40, 46] (and references therein). We employ RQMD(v2.3, cascade mode) here to study Bose-Einstein correlations and determine its accuracy in reproducing the data to second order. The output of RQMD contains identification (particle specie), momentum and freeze out position 4 vectors of each final particle. However RQMD does not include quantum statistics (i.e. Bose-Einstein) or explicit final state interactions (i.e. Coulomb and Strong). Thus taking the particles from RQMD to form C_2 will give no signal at all. A "CoRrelation After Burner" (CRAB) code was developed by S. Pratt [56] to create the signal that we want to compare with in our measured data. CRAB takes as its input the particle pair's identification, and their momentum and position 4 vectors. The output is a weight calculated from i) symmetrizing the pair's wave function, ii) the Coulomb interaction between the pair, and iii) the Strong interaction between the pair (not done for kaon pairs).

To make a C_2 from this model, we first calculate the transverse enregy of each event in E877's participant calorimeter geometrical acceptance to determine the centrality of the event. Particles are then filtered through E877 forward spectrometer's geometrical acceptance, including the close-by track cuts and momentum smearing (due to finite momentum resolution of our appartus). Pairs are then formed from the resulting sample. The pairs are passed to CRAB, which gives weights in accordance to quantum statistics, the Coulomb interaction, and the Strong interaction. The weights are then binned as a function of q so that the calculated C_2 can be easily overlayed with the data. Since we know the model pairs' coordinate configuration, instead of fitting the model C_2, we can just compare the Δx_i of the model pairs to the fit parameters of the data.

Chapter 6

Correlation Results I

The data are derived from $Au + Au$ collisions, with the beam momentum of $11.5AGeV$. The centrality and reaction plane angle of the events are determined using the calorimeters surrounding the target as discussed in Sec. 4.2.2 and 4.2.3. The tracks are identified as particles by calculating the mass from the momentum and time of flight measurements as discussed in Sec. 4.3.2. The two particle correlation signal is constructed and corrected for two-track resolution, extended source Coulomb interaction, and detector acceptance using procedures described in Chapter 5.

In this chapter we will first acquaint the reader with the general features of π^+, π^-, and K^+ C_2s. Once the features are familiar, we will study the C_2s as a function of reaction plane angle, and average pair momentum. Physical interpretations will be offered for the correlation fit radii and λ parameters as well as comparisons to the RQMD model.

All the C_2s are constructed in a fixed observer's frame of $y = 2.73$. This frame is chosen for the ease of fitting the three dimensional YKP parame-

K^+K^+	$\pi^+\pi^+$	$\pi^-\pi^-$
13K pairs with $Q_{inv} < 0.8GeV$	2.3M pairs with $Q_{inv} < 0.6GeV$	6.6M pairs with $Q_{inv} < 0.6GeV$
4K pairs with $Q_{inv} < 0.15GeV$	1.2M pairs with $Q_{inv} < 0.15GeV$	4.2M pairs with $Q_{inv} < 0.15GeV$

Table 6.1: Pairs statistics for 0-10% centrality K^+K^+, $\pi^+\pi^+$, and $\pi^-\pi^-$.

	K^+K^+	$\pi^+\pi^+$	$\pi^-\pi^-$
$\langle Y_K \rangle$	2.34	3.18	3.34
$\langle K_t \rangle (GeV)$	0.16	0.14	0.11

Table 6.2: K^+K^+, $\pi^+\pi^+$, and $\pi^-\pi^-$ averaged pair rapidity and transverse momentum for 0-10% centrality event sample.

terization of C_2. In this frame, q_0 is the least correlated with q_l given our spectrometer acceptance [57]. This point is clearly seen when we examine the two dimensional projection of the YKP parameterization C_2 in Fig. 6.1. It is not a coincidence that this frame is also very close to our measured pion source's rest frame. In the pion source's rest frame, there is no correlation between q_0 and q_l.

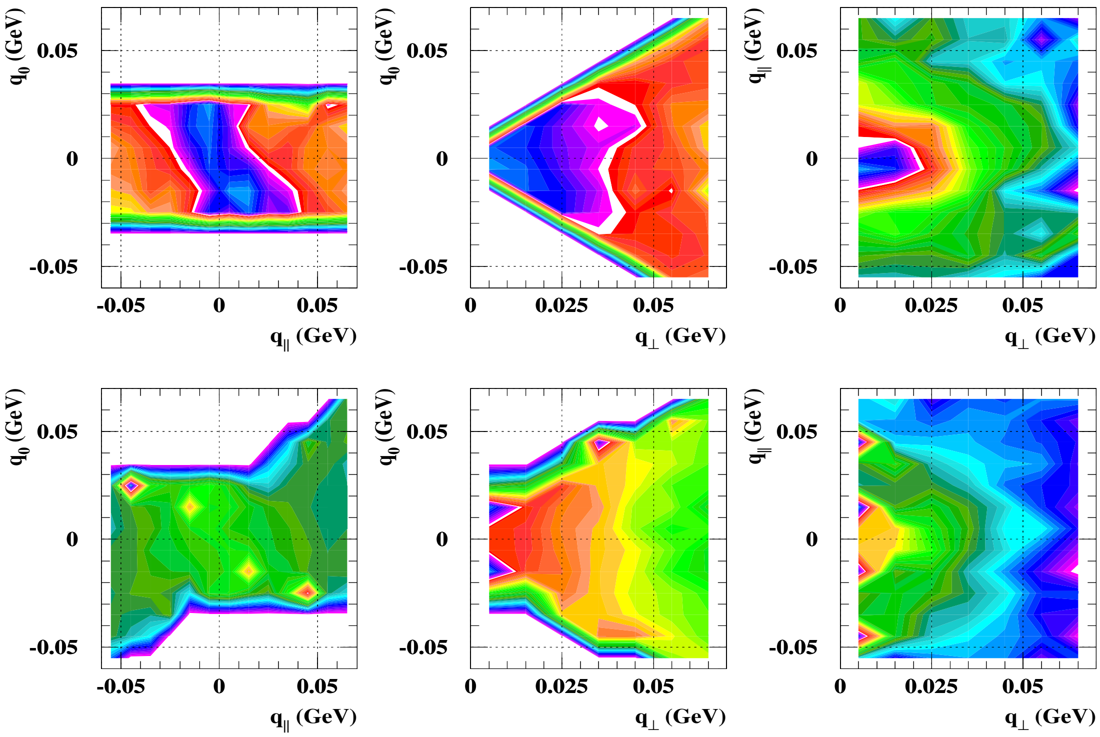

Figure 6.1: Two dimensional contours of $C_2(q_\perp, q_{||}, q_\emptyset)$. The other component is integrated over from -0.3 to 0.3 GeV. The top row is constructed in $Y_{analysis} = LAB$. We can see the tight correlation between q_o and $q_{||}$ in the first panel. The bottom row is constructed in $Y_{analysis} = 2.73$. The correlation between q_o and $q_{||}$ is decidely less pronounced.

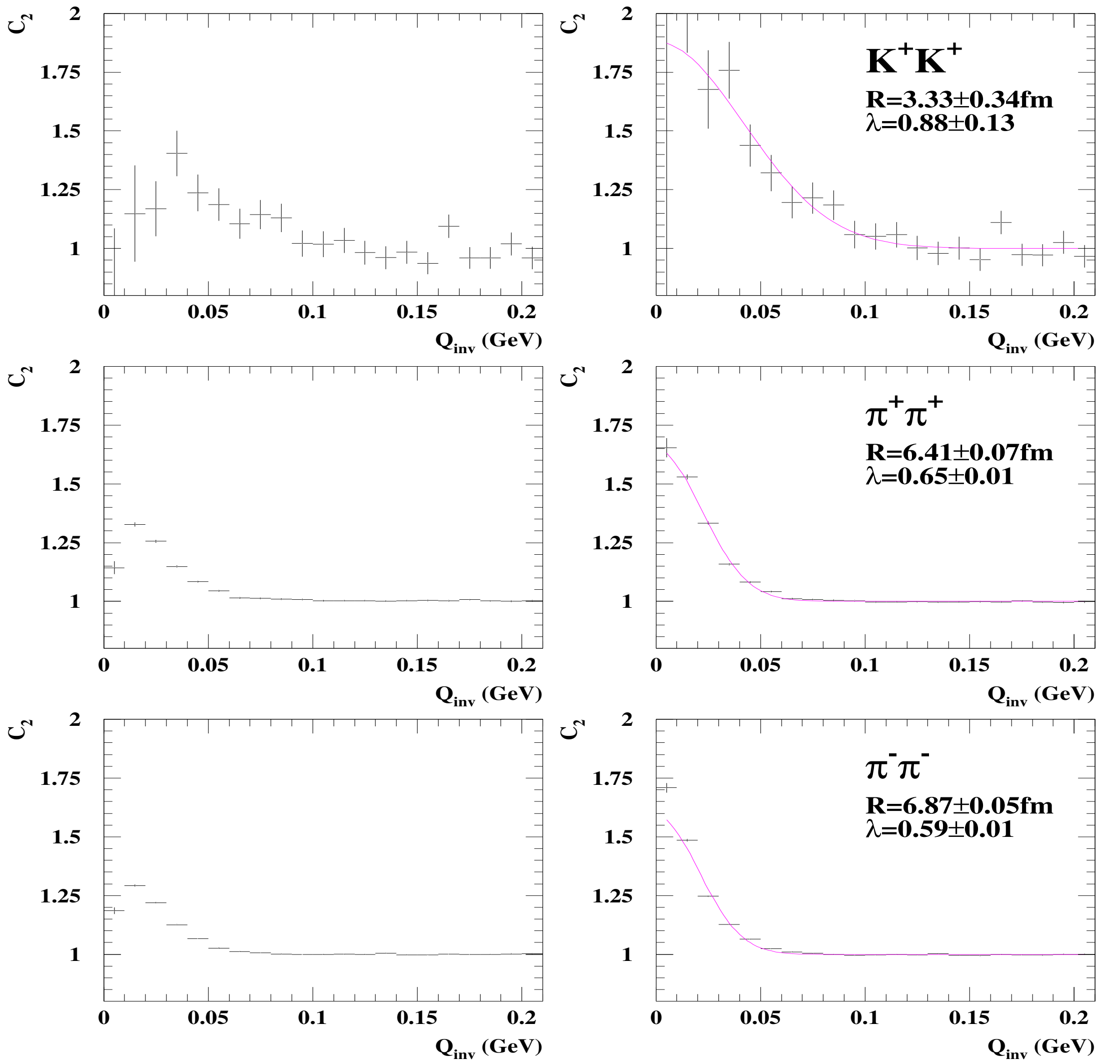

Figure 6.2: Comparison of one dimensional $\pi^+\pi^+$, $\pi^-\pi^-$, and K^+K^+ C_2 for 0-10% centrality events. The left column's C_2s has no Coulomb correction; the right column's C_2 has been divided by the respective extended Coulomb correction. The solid line indicates the resulting fit function. The error bars are statistical only.

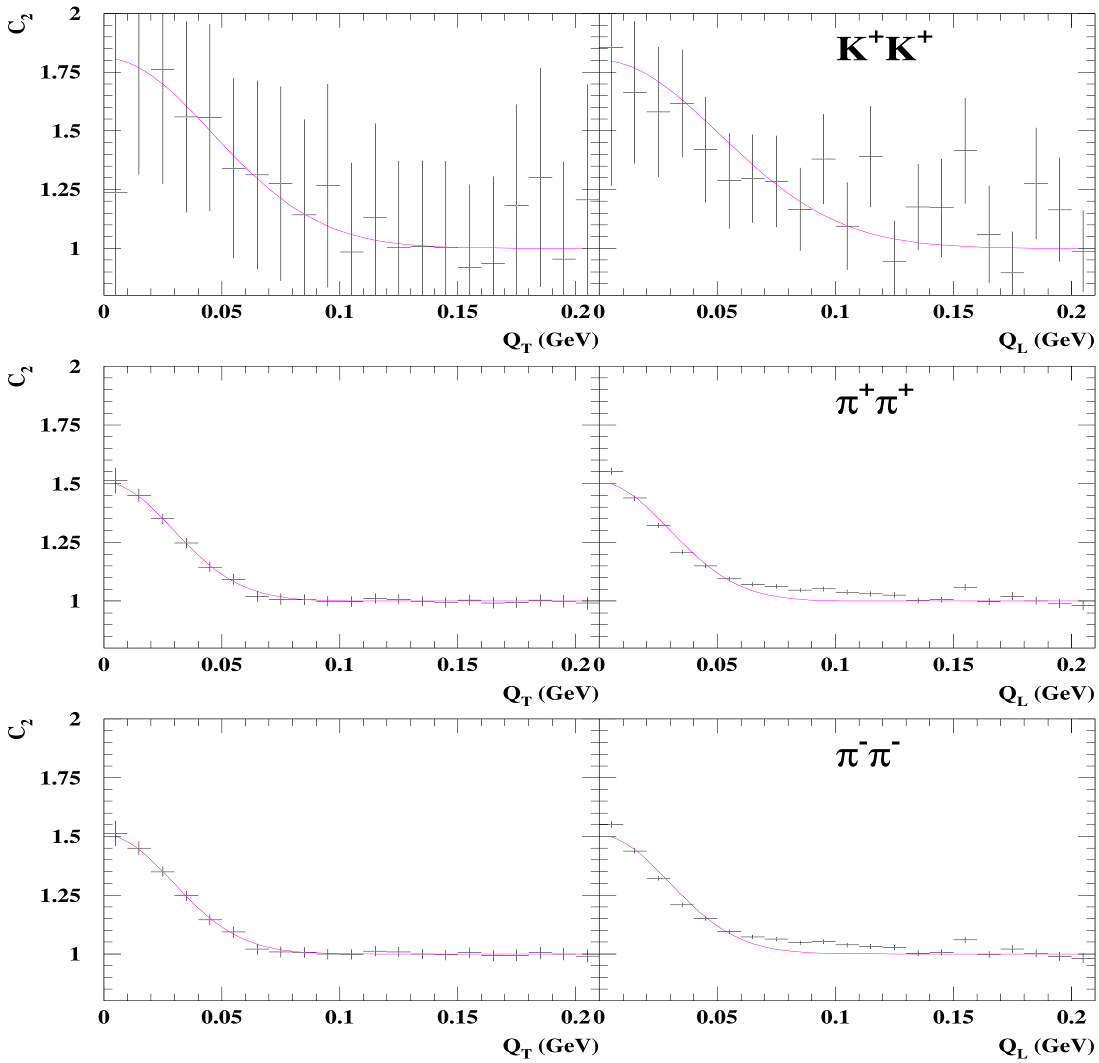

Figure 6.3: Comparison of the projections of the Coulomb corrected two dimensional $\pi^+\pi^+$, $\pi^-\pi^-$, and K^+K^+ C_2 for 0-10% centrality events. For each projection, the other axis has been integrated from 0 to 30 MeV. The values of the fit parameters are summarized in Table 6.3. The solid line indicates the resulting fit function. The error bars are statistical only.

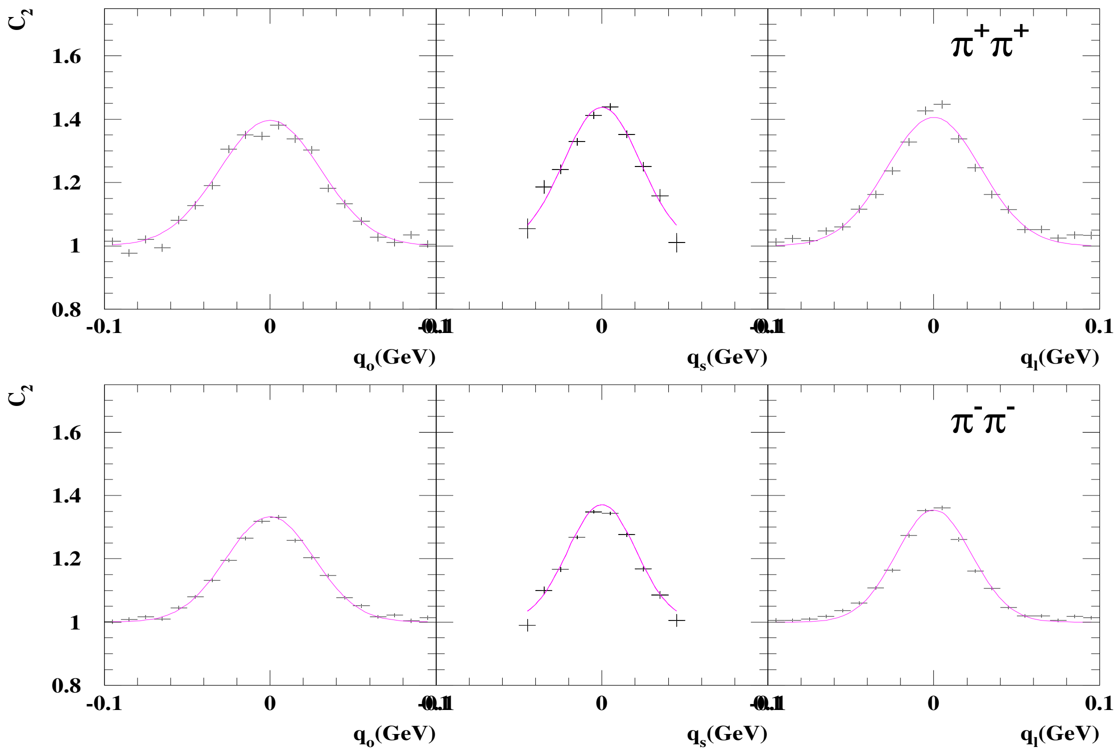

Figure 6.4: Comparison of the projections of the Coulomb corrected three dimensional $\pi^+\pi^+$ and $\pi^-\pi^- C_2$ for 0-10% centrality events using the BP parameterization. For each projection, the other axes has been integrated from -30 to 30 MeV. The values of the fit parameters are summarized in Table 6.4. The solid line indicate the resulted fit function. The error bars are statistical only.

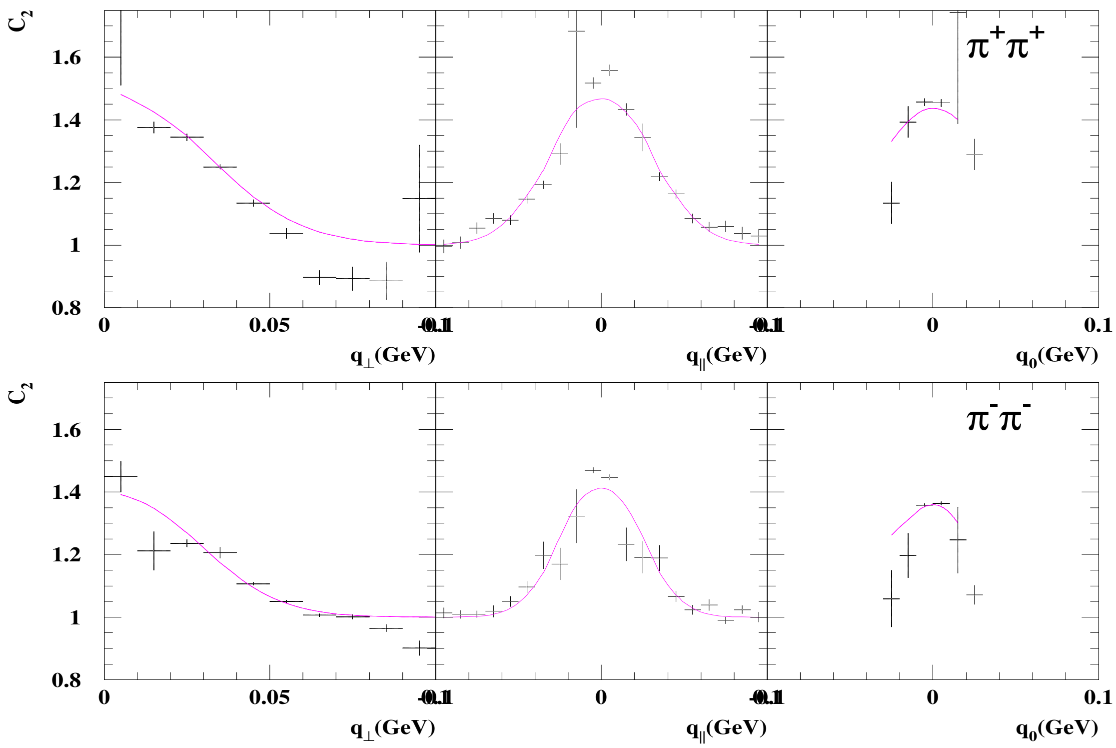

Figure 6.5: Comparison of the projections of the Columb corrected three dimensional $\pi^+\pi^+$ and $\pi^-\pi^-$ C_2 for 0-10% centrality events using the YKP parameterization. For each projection, the other axes has been integrated from -30 to 30 MeV. The values of the fit parameters are summarized in Table 6.5. The solid line indicate the resulted fit function. The error bars are statistical only.

	K^+K^+	$\pi^+\pi^+$	$\pi^-\pi^-$
$R_T(fm)$	3.04 ± 0.40	4.81 ± 0.07	5.70 ± 0.05
$R_L(fm)$	2.73 ± 0.47	4.74 ± 0.08	6.11 ± 0.06
λ	0.86 ± 0.13	0.60 ± 0.01	0.60 ± 0.01

Table 6.3: Parameters from two dimensional fits to $C_2(Q_T, Q_L)$ for K^+K^+, $\pi^+\pi^+$, and $\pi^-\pi^-$ pairs in 0-10% centrality events.

6.1 General Features of $\pi\pi$ and K^+K^+ C_2s

From Chapter 2 we anticipate the C_2s to be of Gaussian shaped peaking at or below 2 at low q and falling off to 1 at large q. The rate of falloff is inversely proportional to the size of the Gaussian source that emitted the particles. Thus we expect a more rapid falloff in these $Au + Au$ data C_2 than the previously observed $Si + A$ C_2 from E814 [58] (E877's predecessor) and E802/859 [59] at roughly the same beam energies. The data that we used to construct C_2s for this sections are from 0-10% centrality events. The statistics of the data are summarized in Table 6.1. The pair kinematics are summarized in Table 6.2.

The one dimensional correlations for K^+, π^+, and π^- are shown in Fig. 6.2. The left panel shows the data prior to Coulomb correction. The right panel shows the data after Coulomb correction overlaid with fit results to Eq. 5.20. The converged fit parameters are written on the plots. The two dimensional correlations for K^+, π^+, and π^- are shown in Fig. 6.3. It is always challenging to show higher dimensions objects on a two dimensional piece of paper. The standard way of displaying higher dimensional correlations is to

	Directly fitted from BP (With no cross terms)		Calculated or directly fitted from YKP	
	$\pi^+\pi^+$	$\pi^-\pi^-$	$\pi^+\pi^+$	$\pi^-\pi^-$
$R_o(fm)$	4.63 ± 0.08	5.31 ± 0.05	4.86 ± 0.10	5.46 ± 0.05
	(4.53 ± 0.08)	(5.26 ± 0.05)		
$R_s(fm)$	6.04 ± 0.15	6.76 ± 0.10	4.79 ± 0.07	5.45 ± 0.05
	(6.04 ± 0.15)	(6.77 ± 0.10)		
$R_l(fm)$	5.00 ± 0.09	6.18 ± 0.06	5.11 ± 0.36	6.16 ± 0.16
	(4.81 ± 0.09)	(6.08 ± 0.06)		
$R_{ol}(fm^2)$	7.19 ± 0.60	6.66 ± 0.45	2.19 ± 1.75	-1.88 ± 1.17
$R_{sl}(fm^2)$	-0.56 ± 0.79	-0.26 ± 0.66	-	-
$R_{os}(fm^2)$	0.22 ± 0.77	0.38 ± 0.58	-	-
λ	0.61 ± 0.01	0.58 ± 0.01	0.60 ± 0.01	0.57 ± 0.01
	(0.60 ± 0.01)	(0.58 ± 0.01)		

Table 6.4: Parameters from three dimensional fits to $C_2(q_o, q_s, q_l)$ (BP parameterization) for 0-10% centrality $\pi^+\pi^+$ and $\pi^-\pi^-$ pairs and comparison to parameters calculated or directely fitted from the YKP parameterization fits to $C_2(q_\perp, q_{||}, q_\emptyset)$.

---

show projections of C_2 onto each of its parameterization axis, with the other axes as near to zero as possible because that is where the signal is. For a two dimensional correlation, $C_2(Q_T, Q_L)$, we choose the projections to be $C_2(Q_T) = \int_0^{Q_L=0.3GeV} C_2(Q_T, Q_L)dQ_L$ and $C_2(Q_L) = \int_0^{Q_T=0.3GeV} C_2(Q_T, Q_L)dQ_T$. In Fig. 6.3, the projection onto the Q_T axis is on the left column; the projection onto the Q_T axis is on the right column. The projections of the fit results to Eq. 5.19 are also overlaid on the data plots. The converged fit parameters are summerized in Table 6.3. The projections of the three dimensional correlations for π^+ and π^- are shown in Fig. 6.4 for the Bertsch-Pratt parameterization, Fig.

	$\pi^+\pi^+$	$\pi^-\pi^-$
$R_\perp(fm)$	4.79 ± 0.07	5.45 ± 0.05
$R_{\|\|}(fm)$	4.22 ± 0.11	5.85 ± 0.07
$\Delta\tau(fm)$	0.00 ± 0.39	0.00 ± 0.37
$(1/\Delta\tau^2(fm^{-2}))$	(38.93 ± 1.41)	(1.85 ± 1.41)
Y_{source}	2.37 ± 0.03	2.64 ± 0.02
λ	0.60 ± 0.01	0.57 ± 0.01

Table 6.5: Parameters from three dimensional fits to $C_2(q_\perp, q_{\|\|}, q_\emptyset)$ (YKP parameterization) for $\pi^+\pi^+$ and $\pi^-\pi^-$ pairs in 0-10% centrality events.

6.5 for the Yano-Koonin-Podgoretskiǐ parameterization. The projections are defined similiarly to the the two dimensional ones above. Overlay with the data are projections of the fit results to Eq. 5.17 (BP) and 5.18 (YKP). The converged fit parameters are summerized in Tables 6.4 (BP) and 6.5 (YKP). Unfortunately, there is not sufficient statistics to construct a three dimensional kaon correlation.

The following features are immediately noticeable from the one, two, and three dimensional C_2 plots. The pion correlation peaks at $q \approx 0$ and falls off to unity at about $q \approx 0.06GeV$. The chaoticity parameter $\lambda \approx 0.6$. The kaon correlation peaks at $q \approx 0$ and falls off to unity further out than the pions, at $q \approx 0.10GeV$. Its $\lambda \approx 1.0$. The location of the peak and the value of the λ for all correlations are the same for one, two, and three dimensions. The shape of the correlations seems approximately Gaussian.

Let us first examine the λ parameter.

The λ parameter is often called the “fudge factor” of correlation measurements because it was not anticipated, but rather found to be *necessary* to fit the first pion correlation data. One explanation to its necessity is that there could exist a component of coherent pion production in the source. For this reason, the λ parameter is called the chaoticity parameter. An alternative explanation is that the initial source shape is not describable by a single Gaussian position space and thus to describe the measured C_2 by a single Gaussian in momentum space is insufficient. We will use our data (and RQMD) to support the latter explanation. An interesting observation is that the pion correlations need a λ parameter to fit the data while the kaon correlations do not. The kaon correlation when fitted with and without the λ parameter resulted in the same χ^2/N_{dof}. For example, for the one dimensional C_2, $\chi^2/N_{dof} = 0.79$ when fitted with λ; $\chi^2/N_{dof} = 0.78$ when fitted without λ (λ is fixed to be 1). This difference can be understood as a result of the πs having a direct and a *long-lived* resonance decay production mechanisms, while the K^+s have a direct production and a *short-lived* resonance decay production mechanisms. Let us first consider the pions:

Pions are the lightest mesons. They are readily produced in any heavy ion collisions, directly and from resonance decays (Δs, Ns, Λs, ηs, and ωs). The direct pion production is in the central region of the collision zone, dubbed the "core," and ceases once the system becomes sufficiently dilute. The "halo" pions, are pions that come mostly from long-lived resonance decays. These resonances remain excited after freezeout, and traverse some distance before decaying, thus releasing the pions in a "halo" region. In this scenario the pion source then is really two sources, a "core" (small radius) and a "halo" (large radius) source, similar to the discussion in Sec. 2.3 and Fig. 2.3. The

λ parameter for the pion correlations then may not be one and is indeed consistently ≈ 0.6. The kaons however, are much heavier in mass than the pions and their interaction cross section with the nucleons is smaller. At our beam energy they can only form K^* resonances. The K^* is short-lived ($\tau c \sim 4fm$) and is incapable of generating a large "halo." The number of kaons produced in heavy ion collisions is small, but they are mostly "core" region kaons. The λ parameter for K^+K^+ C_2 then should be much closer to 1 and it is indeed (see Fig. 6.2 and Fig. 6.3). These remarks are only qualitative. However, as will be shown in Sec. 6.1.1, calculations of the resonance "halo" using the RQMD model reproduce the effect quantitatively. RQMD, by its nature, cannot have coherent production of pions and yet it reproduces both the pion and kaon correlations well *including* the λ parameter. Therefore we see no evidence for coherence production of pions in our data.

Now let us turn the discussion to the radius parameters.

As expected, the one dimensional radius parameter for the πs are larger by approximately a factor of two than those obtained from $Si + A$ collisions [58, 59]. For our $Au + Au$ system, $R_{inv} = 6.41 \pm 0.07fm$ for $\pi^+\pi^+$ and $R_{inv} = 6.87 \pm 0.05fm$ for $\pi^-\pi^-$, while for $Si + Pb$ system $R_{inv} = 3.4 \pm 1.2fm$ for $\pi^+\pi^+$ and $R_{inv} = 4.4 \pm 0.6fm$ for $\pi^-\pi^-$ [58]. This implies that the system we created in a $Au + Au$ collision is larger than that created in $Si + A$. The implication is not surprising since a Au nucleus is bigger than a Si nucleus. However it is interesting to note that the geometrical radius of a Au nucleus ($\approx 7fm$) is about a factor of two larger than the radius of a Si nucleus ($\approx 3.5fm$).

The $\pi^-\pi^-$ radius parameters are consistently on the order of $\approx 10\%$ larger than the $\pi^+\pi^+$ radius parameters. This is indeed curious. One can imagine that if the π^-s have a larger cross section for re-interaction in the collision zone, then it may have a larger "core" emission zone than the π^+s. From the strong interaction point of view, this is unlikely. Even though the system is not isospin symmetric (there are more neutrons in the initial state than protons), the re-interaction of the pions with themselves and with the surrounding nucleons does not differ strongly between π^+ and π^-. However, the π^+s do see the collision zone differently than the π^-s through the Coulomb interaction. The collision zone is not electrically neutral; it is positively charged because the initial beam and target that interacted are positively charged (and electric charge is conserved). Although the Coulomb interaction is far weaker than the strong interaction, its effects are integrated over a long time due to its infinite range. The collision zone is composed of other particles and can be simplified by a third body that is overall of positive charge Z_{eff}. This third body's central Coulomb field accelerates the $\pi^+\pi^+$ pairs and decelerates the $\pi^-\pi^-$ pairs. The π^+s momenta, absolute and relative, are then larger in magnitude than they were initially while the π^-s momenta are smaller. Thus the radius parameters (average separations) extracted from the $\pi^+\pi^+$ pairs are smaller than those extracted from the $\pi^-\pi^-$ pairs (a more pictorial explanation of $\vec{K}_{small} \rightarrow R_{large}$ and $\vec{K}_{large} \rightarrow R_{small}$ is discussed in Sec. 6.3). This effect has been quantitatively calculated in Ref. [60] and the $\pi^-\pi^-$ radius parameters being $\approx 10\%$ larger than the $\pi^+\pi^+$'s is consistent with the influence of a central Coulomb field of a third body of $Z_{eff} \approx 150$.

Another observation concerning the one and two radius parameters is that they are dramatically different from pions to kaons. The possible explanations for this difference are difficult to distinguish. Phase space acceptance due to our spectrometer is different between πs and K^+s, see Fig. 4.13. As will be discussed in Sec. 6.3, the radius parameters are highly dependent on the average momentum $\vec{K}$ of the pairs. However, because the kaon average rapidity in our acceptance is lower than the pion's, this observation makes the difference in the π and K^+ radii even more striking. On the other side of the same coin, momentum-position correlation as a consequence of collective motion will exhibit smaller radii parameter as measured by the particles with the larger mass. Because the kaon mass is much larger than the pion mass (therefore the kaon transverse mass is larger than the pion transverse mass), the kaon radius parameter should be smaller than the pion's. On a completely different avenue, because the kaon does not contain any $\bar{u}$ or $\bar{d}$ quarks, its interaction cross section with the surround nucleons is therefore smaller than the pion. The kaons then can decouple from the system sooner [25] than the pions, giving a smaller kaon correlation radius parameter. The distinction between the explanations discussed here require one to disentangle the effects of a flowing source on the extracted radius parameters for *both* the pions and the kaons. This task will be done in Sec. 7.2 with the help of a model. Summarizing the work in Sec. 7.2, the ambiguity in the kaon flow is sufficient to tolerate results ranging from the kaon's full geometrical source size being 0.5 to 1.2 times the pion's full geometrical source size.

The one dimensional correlation has the disadvantage in that its radius parameters can only be interpreted as an average of the spatial and temporal separation of the particle pair. The details of the separate three spatial and temporal dimensions cannot be examined from the one dimensional correlation. The two dimensional correlation has a similar disadvantage. In addition, the cross term of $q_o q_l$ in the one and two dimensional fits is omitted. Therefore the one and two dimensional correlations are incomplete.

The three dimensional correlation, naturally, is more complete and better understood. However, with the increase in information we also have drawbacks. We need high statistics data to calculate a three dimensional correlation. Here the kaons suffer; because of our limited statistics, no three dimensional kaon correlation can be calculated. The pions, on the other hand, are abundant. Let us examine the three dimensional BP and YKP parameterizations' convergence of the correlations and their consistency with one another.

From the summary of the converged BP parameters for pions in Table 6.4, we see that the source appears to be azimuthally symmetric because the R_{os} and R_{sl} terms are consistent with zero. When all the cross terms, including R_{ol}, are omitted from the fit altogether, the numbers in parentheses in Table 6.4, the other fit parameters remain the same within their error bars. This implies that the cross terms are independent, i.e. not correlated, with the other fit parameters. Due to E877 apparatus' limited opening, R_s is not a well measured quantity (see Appendix A). The cut off of the q_s component is $\approx 0.05GeV$ (i.e. all measurable q_s is less than $0.05GeV$), right where the correlation turns to unity for *all* values of the other q components (see Fig. A.8). The data points at the limits of our spectrometer acceptance, though corrected for all known deficiencies, often suffer from systematic errors. The fit in the q_s direction, due to its unfortunate cutoff, is driven entirely by the data points at the limit of our acceptance (for a detailed discussions that lead us to this conclusion see Appendix A). Additional supporting evidence of this conclusion lies in the examination of the same correlation in the YKP parameterization. Here, the limit in q_s is masked by q_o since the YKP parameterization combines $\sqrt{q_o^2 + q_s^2}$ into one quantity $q_\perp$. Thus $R_\perp$ is more influenced by q_o (than q_s) because its range of coverage extends well beyond $0.1GeV$. The most compelling evidence is the consistency check, Eq. 2.43, of the BP parameters calculated from the fitted YKP parameters. R_o from the BP fit is consistent with R_o calculated from the parameters of the YKP fit. From this check, one has to conclude that $R_o \approx R_\perp(= R_s)$, and $\Delta\tau = \frac{R_o^2 - R_s^2}{\beta_\perp^2} \approx 0$. This conclusion is consistent with the $\Delta\tau$ that is fitted in the YKP parameterization. When looking at the one dimensional projection of the YKP parameterization, one may be quick to point out that the $q_\emptyset$ component suffers the same pitfall as the q_s component in the BP parameterization. But this fear is demonstrated to be unfounded, see Appendix C. Additionally, the R_l calculated from the YKP fit parameters is also consistent with the R_l that is directly fitted in the BP parameterization. The calculated R_{ol}^2 is not consistent with and very much smaller than the directly fitted R_{ol}^2. In calculating the BP parameters from the YKP parameters, we take the mean values (from the pairs that make up our data sample) for $\beta_\perp$ and $\beta_{||}$. This is an inherent approximation because the consistency formulas, Eq. 2.43, are meant to be used pair by pair (or very narrow kinematics window of pairs sample).

	$R_{inv}(fm)$ RQMD (Data)	λ RQMD (Data)
K^+K^+	2.78 ± 0.25 (3.33 ± 0.34)	1.08 ± 0.16 (0.88 ± 0.13)
$\pi^+\pi^+$	5.76 ± 0.19 (6.41 ± 0.08)	0.84 ± 0.03 (0.65 ± 0.01)
$\pi^-\pi^-$	5.90 ± 0.23 (6.87 ± 0.05)	0.75 ± 0.04 (0.59 ± 0.01)

Table 6.6: Comparision of the one dimensional C_2's fit parameters from RQMD and data for $0 - 10\%$ centrality.

6.1.1 Comparison to RQMD

We can compare our observations of the data to observations in RQMD. (Construction of C_2 from RQMD+CRAB is described in Sec. 5.5.) RQMD has, among its many outputs, the spatial and temporal freeze out position of each particle, and the last interaction that created each particle. We compare the RQMD derived C_2s with the data C_2s, and where we observe agreement we then examine the RQMD coordinate distributions and particles' last interaction to gain insight into the RQMD source and how it relates to reality.

Fig. 6.6 shows an overlay of the uncorrected (no Coulomb correction) data C_2s with RQMD derived ones for $0 - 10\%$ σ/σ_{geom}. Overall, we see that RQMD reproduces the shape of the data well. The kaon data correlation look consistent with RQMD's. There is not much difference between the RQMD π^+ and π^- correlations while there is a difference between them in the data. RQMD pion source seems slightly smaller than the data for both the π^+s

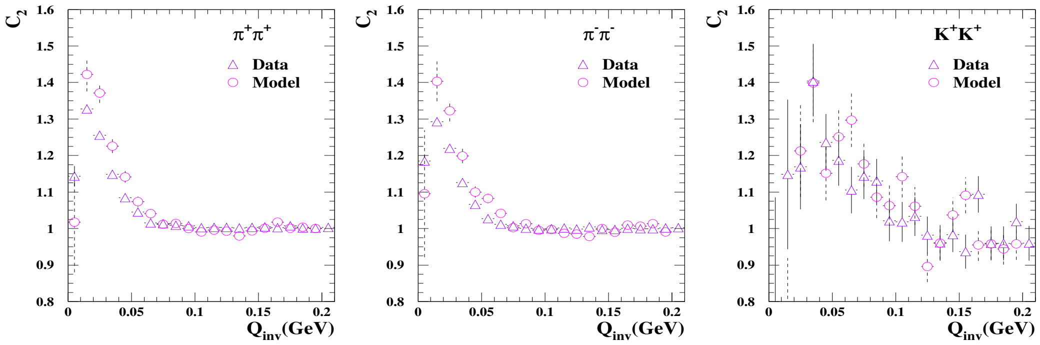

Figure 6.6: Overlay of RQMD+CRAB and data C_2s for $\pi^+\pi^+$, $\pi^-\pi^-$, and K^+K^+ for $0-10\%$ centrality events.

---

and the π^-s. Additionally, the pion λ parameter of RQMD is slightly higher than the data. If anything, the λ parameter would be reproduced better with an even higher concentration of long-lived resonance decays in the RQMD final state. Table 6.6 shows a comparison of the fit parameters of the one dimensional correlations between RQMD and data. The fit parameters in the table support the observation made with the overlay plots in Fig. 6.6. Because RQMD's pion radius parameter is smaller for both the π^+s and the π^-s, the mechanisms of π^+ and π^- production in RQMD are not so correct. The expectation of RQMD(+CRAB) inability to fit the data due to the neglect of Coulomb interaction with a third body source alone is not sufficient to explain for this inconsistency.

For completeness we now discuss the RQMD pion and kaon sources. In Table 6.7 we have summarized the last interactions that produced the low q π^+, π^-, and K^+ that contributed to the corresponding RQMD derived correlations.

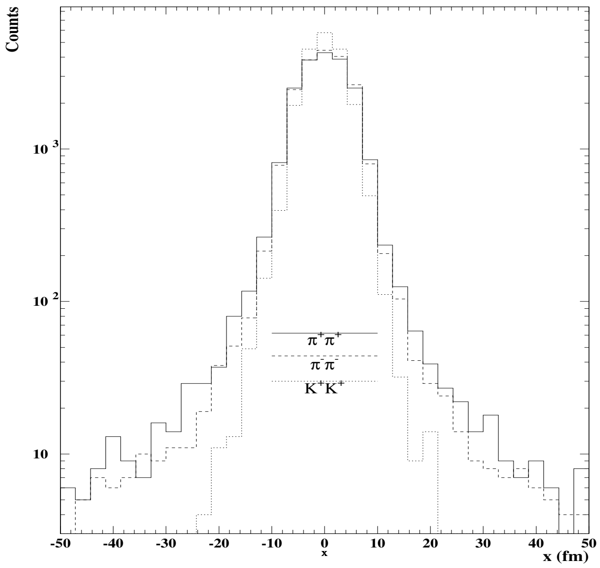

Figure 6.7: x distributions of low q $\pi^+\pi^+$,$\pi^-\pi^-$, and K^+K^+ pairs from RQMD for $0-10\%$ centrality events. x is measured in the center of mass frame of the colliding system $(Au+Au)$. Solid line is from π^+. Dash line is for π^-. Dotted line is for K^+.

Character of Final Interaction	π^+	π^-	K^+
collision	9.0%	7.9%	39.0%
string	5.1%	5.2%	7.3%
Δ	53.5%	56.9%	-
heavy resonances (excluding Δs)	13.1%	12.7%	15.5%
K^{*+}	7.0%	0.3%	11.8%
K^{*0}	-	1.8%	26.8%
vector mesons	10.1%	13.3%	-
η_c	1.1%	-	-
Σ^*,Ξ,and Ω^-	1.0%	1.0%	-

Table 6.7: Character of final interactions that produced the π^+, π^-, and K^+ that make low q pairs for $0-10\%$ centrality events.

It is interesting to note that only 10% of our low q πs comes from elementary collisions, over $\sim 50\%$ comes from Δ resonances, and $\sim 10\%$ comes from the longer lived vector mesons (η, ω, ρ). On the other hand, $\sim 40\%$ of low q K^+s comes from elementary collisions and another $\sim 38\%$ comes from the decay of the K^*s. The fact that $\sim 40\%$ of K^+s and only $\sim 10\%$ of πs come from elementary collisions, coupled with virtually no K^+s come from long lived resonances while $\sim 10\%$ of pions do, seems to be an adequate mechanism to account for the λ parameter difference between the two ($\pi^\pm$ and K^+) particle species' C_2s.

In Fig. 6.7 is a collection of the low q particles' (those that we use to calculate the RQMD+CRAB correlations) x spatial distribution from RQMD. The x is measured in the center of mass frame of the colliding system. The distribution in y, not shown, is similiar. The feature to notice is that for x distributions for pions has decidely non-Gaussian tails, while the kaon's x distribution does not. The r.m.s. of the pions' x distributions is $\sim 6fm$ while for the K^+s it is $\sim 4fm$. The full r.m.s. of (mid-rapidity) pions x distribution $\sim 7fm$ is larger. The full r.m.s. of (mid-rapidity) kaons $\sim 4.5fm$. This illustrates that $R_{fit} < r.m.s._{accept} < r.m.s._{full}$, as a consequence of flow (x-p correlation discussed in Sec. 2.2). RQMD's flow is caused by binary collisions between the particles of the system that results in a natural self ordering of the system - collective motion. This mechanism creates a similar flow (an integrated effect) observed in the data (though a more thorough study showed that the details of the flow do not quite match but are improved with mean field potentials) [39, 61]. The same flow mechanism is quite sufficient to match the correlations data as well.

6.2 Reaction Plane Dependence of C_2

The source created during heavy ion collisions is extremely complex. Our measured pion pairs trace back to only the pion source, a part of the "whole" source. Interesting observations have been made concerning the momentum distributions of the source [39, 61]. Specifically, the most relevant to this thesis is the momentum distributions of the pion source. The directed and elliptic flow [1] are measured to be non-zero for pions. Even though momentum

---

[1]In the language of Fourier analysis, directed flow = 1^{st} moment; elliptic flow (in plane expansion/squeeze out) = 2^{nd} moment.

is a conjugate variable to the spatial coordinate, the anisotropy observed in momentum space does not necessarily mean that an anisotropy also exists in coordinate space. But since the objective of correlation measurements is to gain insight into the spatial distribution of the source, it is tempting to measure specific correlations that aim to investigate anisotropy in coordinate space. Another motivation is that such a study is a test for memory of the initial spatial configuration of the system. For any non-central collision, the initial overlapping region between beam and target particles is an "almond" shape. The degree of this "almond"-ness, depends on how peripheral the collision we are examining. Because the source is dynamic, this initial state asymmetry will be somewhat smeared. An investigation using correlation functions will let us assess to what degree the system has established spatial equilibrium.

The observation of anisotropy in momentum space in Ref. [39, 61] was possible thanks to the E877 calorimeters' ability to determine the reaction plane angle (ψ_R) for each event. The best resolution for ψ_R, at the semi-peripheral events, is $\sim 30°$ [39]. For central events, since $|\vec{b}|$ is small, its direction is more difficult to determine with certainty. Thus, the dependence of any quantity on ψ_R is studied using mostly semi-peripheral events. We choose the centrality window for correlations with respect to ψ_R to be $9-16\%$. Since there are less particles produced in the less central events, this centrality window is a balance between the best ψ_R resolution and statistics of true pairs. The $9-16\%$ pion pair data set is further divided into four subsets: "same," "opposite," "per1," and "per2." "Same" refers to the pair's $\vec{K}_t$ being mostly parallel to $\vec{b}$, i.e. $-45° < \phi_{K_t} - \psi_R < 45°$ where $\phi_{K_t} = \arctan(\frac{K_y}{K_x})$. "Opposite" is where $135^\circ < \phi_{K_t} - \psi_R < 225^\circ$. "Per1" refers to $45^\circ < \phi_{K_t} - \psi_R < 135^\circ$. "Per2" refers to $-135^\circ < \phi_{K_t} - \psi_R < -45^\circ$. A pictorial guide for these four cuts is drawn on the left panel of Fig. 6.8. When we combine "same" and "opposite" we get the "in" plane subset. Combining "per1" with "per2" we get the "out" of plane subset. See the right panel of Fig. 6.8. Because of the periodic nature of angles, an absolute way of defining these cuts is via sines and cosines:

$$
\begin{aligned}
\text{“Same”} &: \cos(\phi_{K_t} - \psi_R) > 1/\sqrt{2}; \\
\text{“Opposite”} &: \cos(\phi_{K_t} - \psi_R) < -1/\sqrt{2}; \\
\text{“Per1”} &: \sin(\phi_{K_t} - \psi_R) > 1/\sqrt{2}; \\
\text{“Per2”} &: \sin(\phi_{K_t} - \psi_R) < -1/\sqrt{2}; \\
\text{“In”} &: |\cos(\phi_{K_t} - \psi_R)| > 1/\sqrt{2}; \\
\text{“Out”} &: |\cos(\phi_{K_t} - \psi_R)| < 1/\sqrt{2}.
\end{aligned}
\tag{6.1}
$$

Comparing "same" with "opposite" C_2s probes the 1^{st} moment of the anisotropy in coordinate space, if any. Comparing "per1" with "per2" C_2s is a test of the systematics of our cuts and correlation constructions since we expect no difference in the "per1" and "per2" C_2s because the "per1" subset should contain the same admixture of "same" and "opposite" as the "per2" subset. Comparison of "in" with "out" is a probe of the 2^{nd} moment of the anisotropy in coordinate space, if any.

The ϕ_{K_t} of each true pair is calculated and compared to the ψ_R of the event to decide which category (Eq. 6.1) the pair belongs to. For false pairs, the decision is not so straightforward. The complication comes from the fact

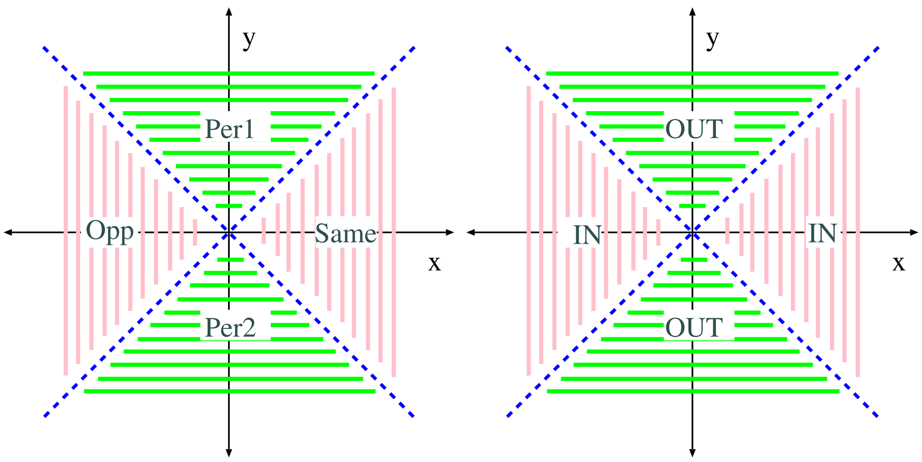

Figure 6.8: Schematic of cuts made relative to ψ_R. The left panel shows the "same-opposite-per1-per2" cuts. The right panel shows the "in-out" cuts.

---

that a false pair is made up of two singles from two different events. There is no common "ψ_R of the event" to compare to the calculated ϕ_{K_t}. To account for this, false pairs include an additional check to make sure that the singles in the pair come from similar events. "Similar events" means that $|\psi_{R_1} - \psi_{R_2}|$ must at least be less than ψ_R's resolution. We choose $|\psi_{R_1} - \psi_{R_2}| < 10°$. The number of $\pi^+\pi^+$ pairs that fall into each subsets are shown in Fig. 6.9; for $\pi^-\pi^-$ pairs are shown in Fig. 6.10. Note that in the figures there are many false pairs that do not meet the requirement that their parent events are similar, as defined above. Observations made in Ref. [39, 61] are also made here. Pions exhibiting anti-flow is evident in having more pion pairs in the "opposite" than the "same" direction. Pions exhibiting in plane expansion is evident in having more pion pairs in the "in" than the "out" direction. Another simple way to observe this is to plot the event count that have at least two π^+s (π^-s) in the event as a function of ψ_R. This is shown in Fig. 6.11 in the left (right) panel. The plots are constructed with two independent sets of devices: the vertical axis, the event count, is based upon the spectrometer to track at least two pions, while the horizontal axis, the ψ_R relative to lab coordinate, is based upon the calorimeters to determined transverse energy asymmetry. Because of our spectrometer opening, most of the events that we record are events with $\psi_R = \pm 180°$. From the plots, there is clearly an excess of events with more than two pions at the $\psi_R = 0$ type of events. The pions are anti-flowing.

One dimensional correlations are constructed from the subsets of pion pairs. If there is any anisotropy in coordinate space, we expect to see a difference in the "same" and "opposite" C_2s, and/or the "in" and "out" C_2s. The results of the different cuts with respect to ψ_R are shown in Fig. 6.12 for $\pi^+\pi^+$, and in Fig. 6.13 for $\pi^-\pi^-$. The C_2 referred to in each figure is the uncorrected (no Coulomb correction) C_2. This choice minimizes any error that may be introduced with a Coulomb correction. The first row in each figure is an overlay of C_2s with the relevant cuts to one another, i.e. "in" with "out", "same" with "opposite", and "per1" with "per2". It conveys that there is no difference between the cuts. The second row shows the ratio of the C_2s seen in the first row. It reconfirms the conclusion reached by looking at just the first row. The collision zone has lost its initial asymmetry almost entirely.

As discussed in Sec. 6.1, one dimensional C_2 is an average of the four components of q. A more direct study is to construct higher dimensional C_2s. To explore the differences between "same" and "opposite" side effects, we

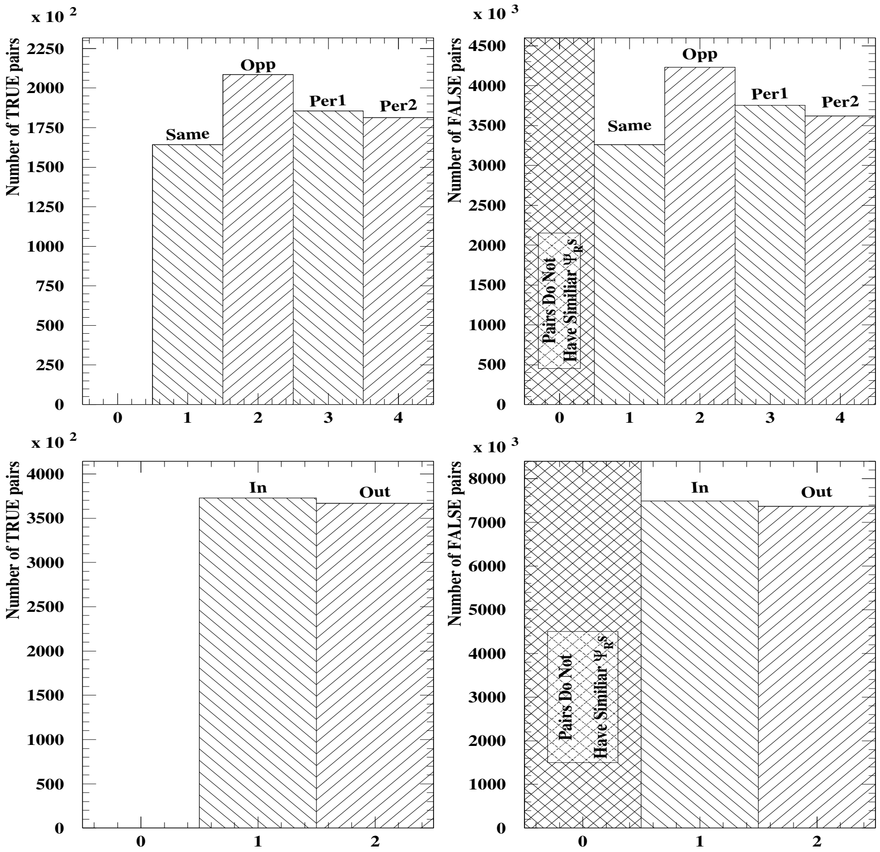

Figure 6.9: Proportions of $\pi^+\pi^+$ pairs that make the various cuts with respect to ψ_R, as defined in the text.

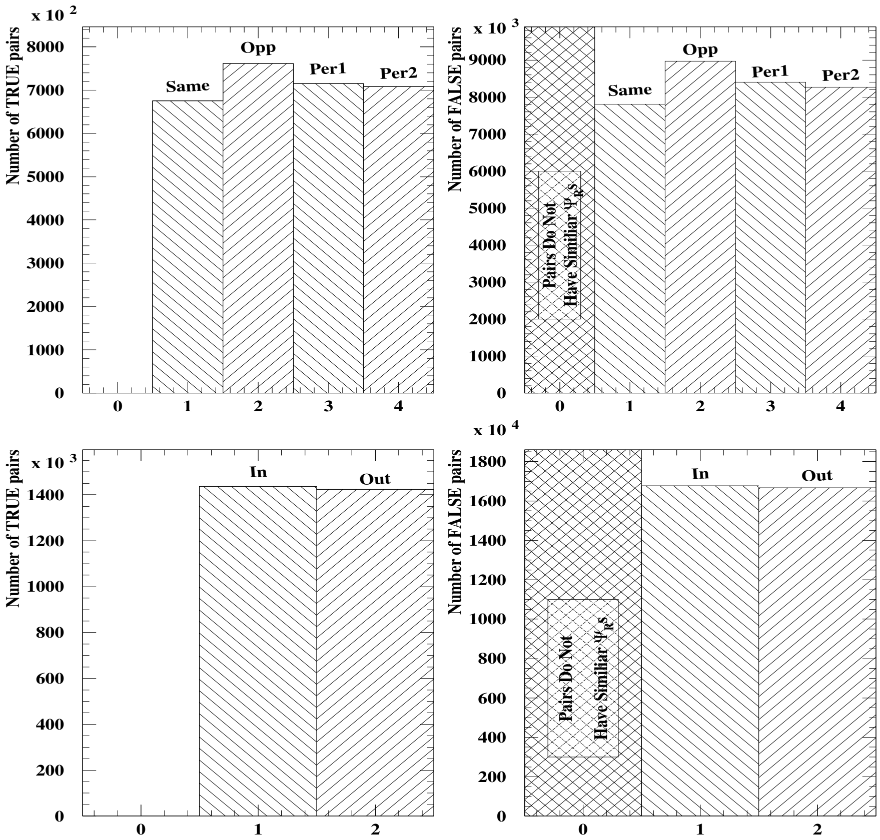

Figure 6.10: Proportions of $\pi^-\pi^-$ pairs that make the various cuts with respect to ψ_R, as defined in the text.

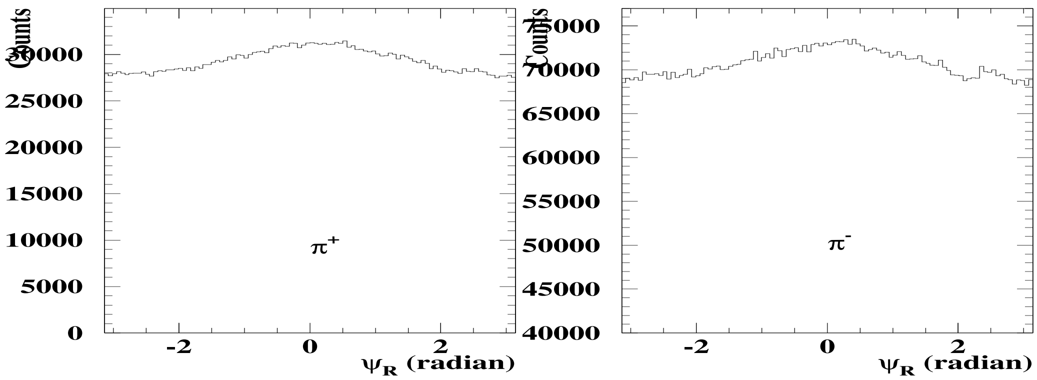

Figure 6.11: Event counts for events with more than two pions as a function of ψ_R for π^+ on the left panel, for π^- on the right panel. The pions are clearly anti-flowing.

---

compare $R_\perp$ from each subset's $C_2(q_{||}, q_\perp, q_\emptyset)$ [2]. The fit results are summarized in Tables 6.8 and 6.9. As one can see, there is no difference between any of the subset's fitted $R_\perp$, for this $9-16\%$ centrality window within our sensitivity. (It is also encouraging that there is no difference between the subset's other fit parameters, because there should not be any.) This reconfirms the one dimensional result discussed above.

To explore the differences between "in" and "out" of plane effects, we constructed a four dimensional correlation:

$$C_2(q_x, q_y, q_z, q_\emptyset) = 1 + \lambda e^{-R_x^2 q_x^2 - R_y^2 q_y^2 - R_z^2 q_z^2 - \tau^2 q_\emptyset{}^2}, \tag{6.2}$$

[2]In theory, we can also compare R_{side} from each subset's $C_2(q_o, q_s, q_l)$. But due to our limited coverage in q_s (as discussed in Appendix A), the YKP parameterization is the only choice we have.

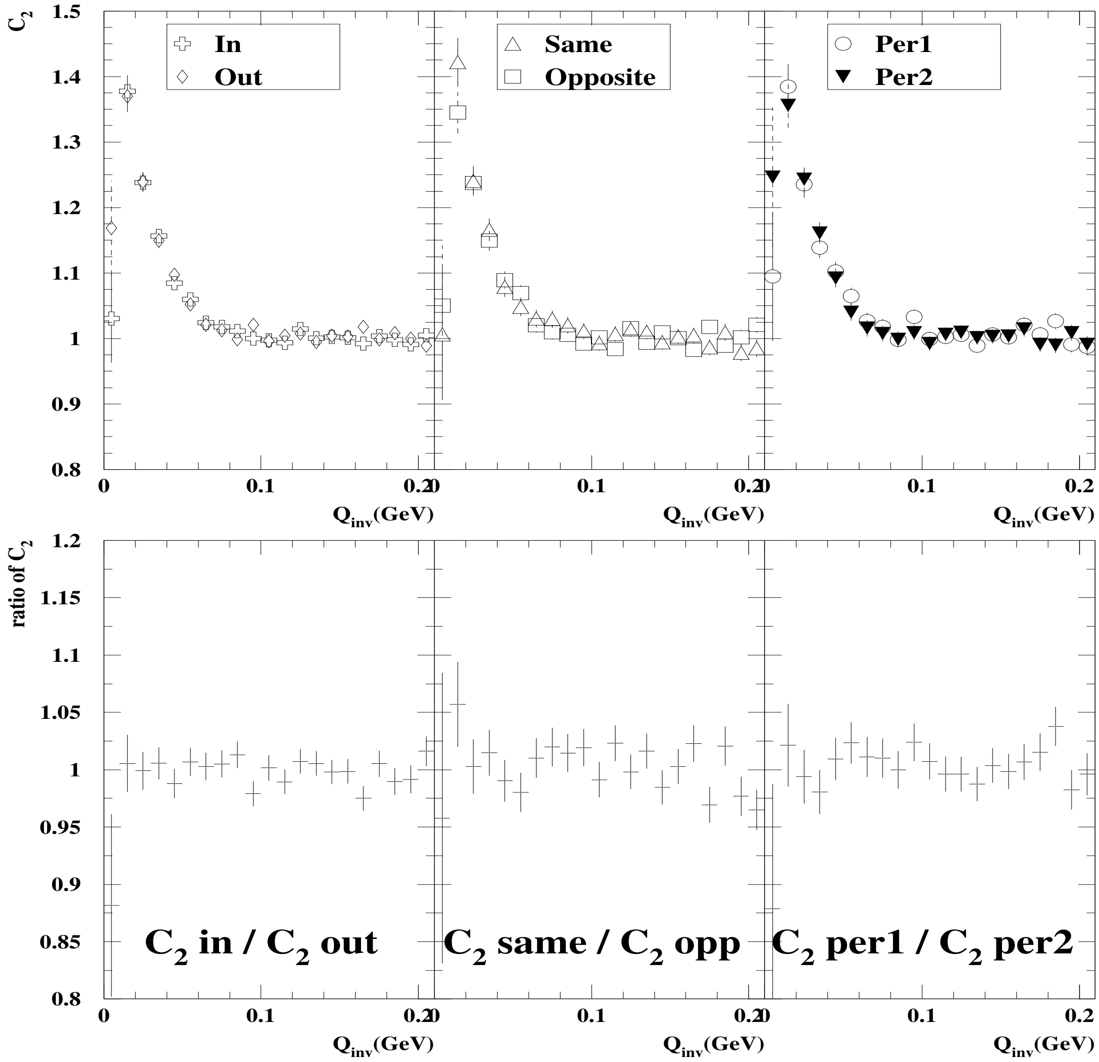

Figure 6.12: For $9-16\%$ centrality $\pi^+\pi^+$ pairs: Top row - overlay of C_2s with different cuts with respect to ψ_R. Bottom row - ratio of C_2s with different cuts with respect to ψ_R.

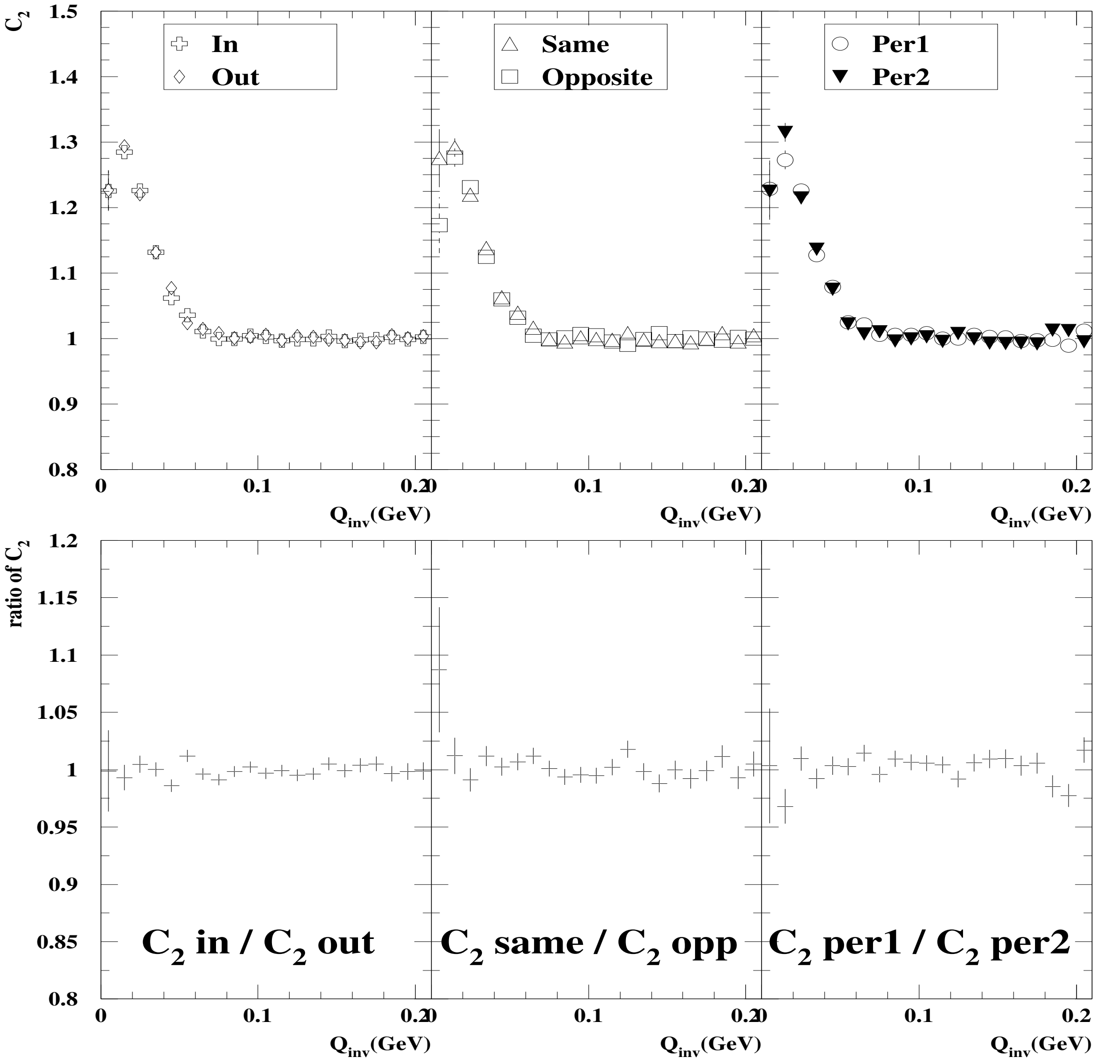

Figure 6.13: For $9-16\%$ centrality $\pi^-\pi^-$ pairs: Top row - overlay of C_2s with different cuts with respect to ψ_R. Bottom row - ratio of C_2s with different cuts with respect to ψ_R.

$\pi^+\pi^+$	"Same"	"Opposite"	"Per1"	"Per2"
$R_\perp(fm)$	4.47 ± 0.27	4.94 ± 0.24	4.79 ± 0.25	5.15 ± 0.28
$R_{\parallel}(fm)$	3.63 ± 0.38	3.73 ± 0.31	4.18 ± 0.37	3.74 ± 0.39
$\Delta\tau(fm)$	0.00 ± 1.09	0.00 ± 1.35	0.00 ± 2.42	0.00 ± 1.90
Y_{source}	2.44 ± 0.13	2.37 ± 0.12	2.53 ± 0.13	2.31 ± 0.14
λ	0.53 ± 0.04	0.60 ± 0.04	0.57 ± 0.04	0.60 ± 0.04

Table 6.8: The fit parameters for $\pi^+\pi^+$ $C_2(q_{\parallel}, q_\perp, q_\emptyset)$ with respect to the reaction plane angle.

$\pi^-\pi^-$	"Same"	"Opposite"	"Per1"	"Per2"
$R_\perp(fm)$	5.45 ± 0.14	5.51 ± 0.14	5.55 ± 0.14	5.64 ± 0.14
$R_{\parallel}(fm)$	5.70 ± 0.23	6.08 ± 0.20	5.71 ± 0.22	5.70 ± 0.25
$\Delta\tau(fm)$	0.00 ± 1.09	0.00 ± 1.22	0.00 ± 1.15	0.00 ± 0.99
Y_{source}	2.64 ± 0.07	2.80 ± 0.06	2.74 ± 0.07	2.60 ± 0.08
λ	0.56 ± 0.02	0.56 ± 0.02	0.56 ± 0.02	0.59 ± 0.02

Table 6.9: The fit parameters for $\pi^-\pi^-$ $C_2(q_{\parallel}, q_\perp, q_\emptyset)$ with respect to the reaction plane angle.

---

for the whole data set of $9-16\%$ centrality. The components of q are broken down as follows: q_x is in the direction of ψ_R; q_y is in the transverse direction perpendicular to q_x; q_z is in the beam direction; $q_\emptyset$ is the energy component of q. This parameterization has the advantage that it utilizes the $9-16\%$ centrality data set as a whole. It also does not suffer the pitfall of the *out-side-long* parameterization. Since there is no preferred $\vec{b}$ for any reactions ($Au+Au$ or others), ψ_R is a flat distribution when averaged over many events. Consequently the x (and y) direction is also a flat distribution (relative to lab coordinates) when averaged over many events. R_x then is the dimension of the

	$\pi^+\pi^+$	$\pi^-\pi^-$
$R_x(fm)$	5.03 ± 0.19	5.56 ± 0.10
$R_y(fm)$	5.14 ± 0.19	5.79 ± 0.10
$R_z(fm)$	4.35 ± 0.16	5.95 ± 0.10
$\Delta\tau(fm)$	0.00 ± 3.65	0.00 ± 1.27
Y_{source}	2.49 ± 0.08	2.70 ± 0.03
λ	0.60 ± 0.003	0.59 ± 0.010

Table 6.10: Best fit parameters to $C_2(q_x, q_y, q_z, q_\emptyset)$ for 9-16% centrality pions. $q_\emptyset$ is the energy difference of the pair. The $\vec{q}$ is parameterized as follows: q_z is the component along the beam direction; q_x is the component of $\vec{q}_t$ that is aligned with the reaction plane angle of the events; q_y is the component perpendicular to q_x and q_z.

---

source in the reaction plane ("in"), while R_y is the dimension of the source out of the reaction plane ("out"). The energy component, $q_\emptyset$, is kept explicitly in the parameterization in Eq. 6.2 (instead of replacing it by an equation similar to Eq. 2.23) so as not to complicate the R_x and R_y parameters with a time ($\Delta\tau$) component. The projections of this C_2 for $\pi^+\pi^+$ and $\pi^-\pi^-$ are shown in Fig. 6.14 and the extracted fit parameters are summarized in Table 6.10. It is not surprising that $R_x \approx R_y$ for both $\pi^+\pi^+$ and $\pi^-\pi^-$ C_2s. This confirms the one dimensional results discussed previously.

6.2.1 Comparison to a Geometrical Model

In a naive geometrical model of the collision, we would expect to see a difference between R_x and R_y if the source were to retain its relative dimensions

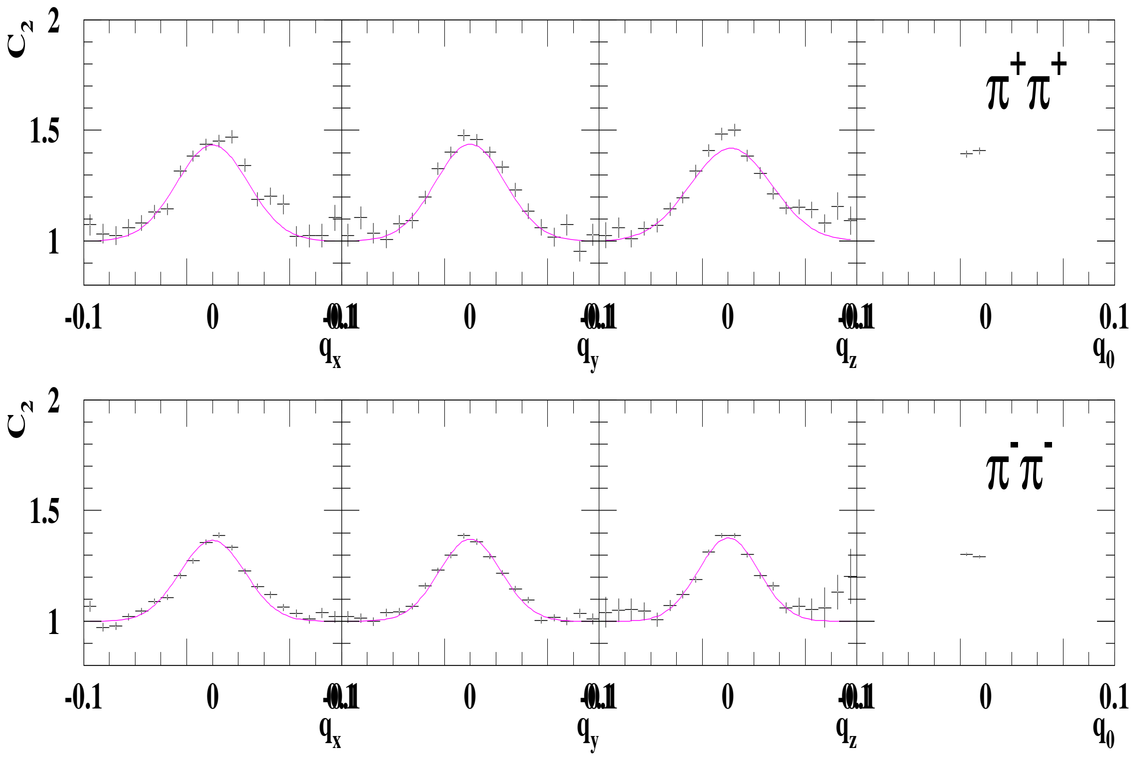

Figure 6.14: One dimensional projection of $C_2(q_x, q_y, q_z, q_\emptyset)$ with overlay of the resulted fit function for $\pi\pi$ pairs. The other axes are integrated over $\pm 0.30 GeV$.

during expansion. This expectation comes from a simple picture of the spatial asymmetry in the initial overlapped region of the two colliding nuclei, see Fig. 6.15. If the Au nucleus is modeled to be a billiard ball with radius $\sim 7fm$ ($R = 1.2A^{1/3}$,$A = 197$), then for a 9% σ/σ_{geom} event, $R_x \approx 5.5fm$ and $R_y \approx 7fm$. For a 16% σ/σ_{geom} event, $R_x \approx 4.5fm$. In this model, if the asymmetry in R_x and R_y were to be maximal - what they are at the initial moment of overlap, because expansion and/or temperature can "equilibrate" the spatial configurations of the particles - then the ratio of $C_2^{``in"}/C_2^{``out"}$ would deviate noticeably from unity. This billiard ball model's ratio is:

$$\frac{C_2^{``in"}}{C_2^{``out"}} = \frac{1+\lambda e^{-R_x^2 Q_{inv}^2}}{1+\lambda e^{-R_y^2 Q_{inv}^2}} \tag{6.3}$$

where $\lambda = 0.6$;

for 9% $R_x \approx 5.5fm$, $R_y \approx 7fm$;

for 16% $R_x \approx 4.5fm$, $R_y \approx 7fm$.

The overlays of this ratio for 9% and 16% with the data are shown in the left panels of Fig. 6.16 and 6.17. For a generic difference in the ratios of the C_2s' Rs, we have constructed curves to indicate the degree of difference in the measured radii as follows:

$$Ratio\Big(\frac{C_2(R_1)}{C_2(R_2)}\Big)\% = \frac{R_1 - R_2}{R_1} \times 100\%. \tag{6.4}$$

The curves in the right panels of Fig. 6.16 and 6.17 show *ratio* of -20% (lower most curve), -14%, -8%, -2%, 4%, 10%, and 16% (top most curve). (Negative *ratio* just means that $R_2 > R_1$.) For the $\pi^+\pi^+$ pairs, we can exclude a radii difference between "same" and "opposite", and "in" and "out", of greater than

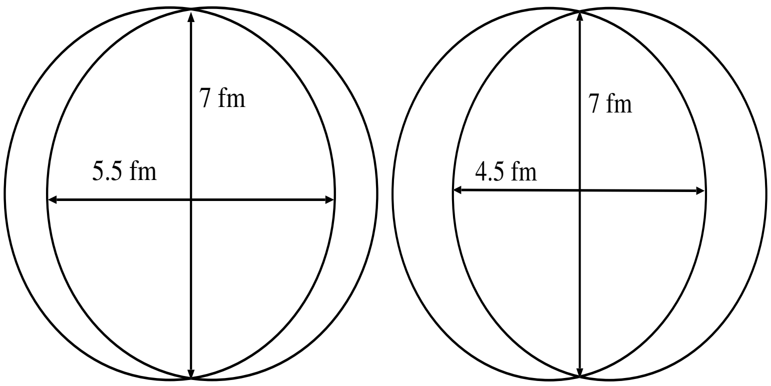

Figure 6.15: Geometric overlap of $Au + Au$ at 9% (left panel) and 16% (right panel) σ/σ_{geom}.

8%. For the $\pi^-\pi^-$ pairs, we can exclude a radii difference between "same" and "opposite", and "in" and "out", of greater than 6%. The upper limits of the difference between "same" and "opposite" radii, and "in" and "out" radii, for both charges of pion pairs are consistent with the multidimensional analysis of the data.

6.3 $\vec{K}$ Dependence of C_2

Average pair momentum, $\vec{K}$, dependence of C_2 is a consequence of x-p correlations. There is a preferred particle momentum direction depending on where the particle is emitted from. A simple way to see how this affects our correlation measurements of radius parameters is to think of the following, keeping in mind that the radius parameters are a measure of the average separation of particle pairs. Assuming for simplicity that freezeout is instan-

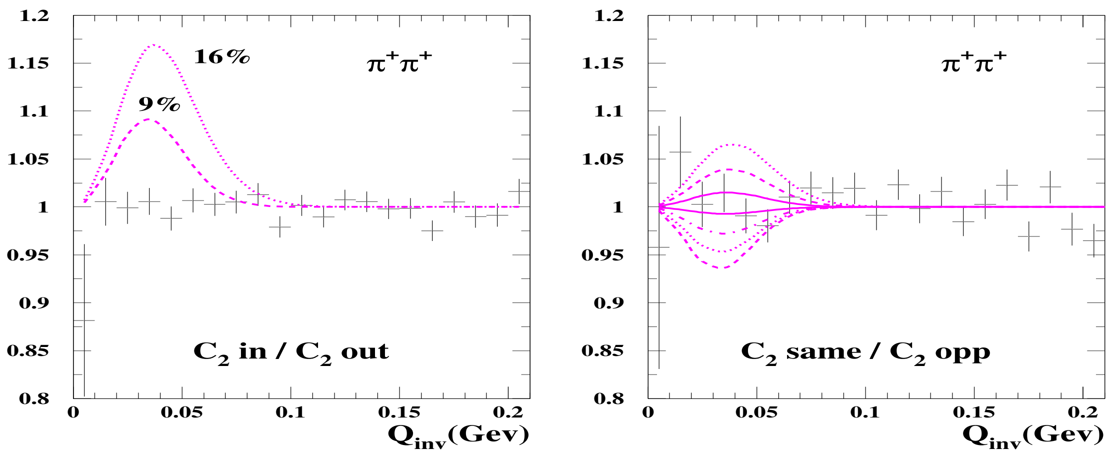

Figure 6.16: Left panel: Ratios of $C_2^{``in"}/C_2^{``out"}$: the data's $\pi^+\pi^+$ C_2 ratio overlay with a geometrical expectation of a 9% σ/σ_{geom} events' ratio and a 16% σ/σ_{geom} events' ratio. Right panel: Ratios of $C_2^{``same"}/C_2^{``opposite"}$, the data's $\pi^+\pi^+$ C_2 ratio overlay with geometrical expectations of $Ratio\left(\frac{C_2(R_1)}{C_2(R_2)}\right)\%$ (as defined in the text) of -20% (lower most curve), -14%, -8%, -2%, 4%, 10%, and 16% (upper most curve).

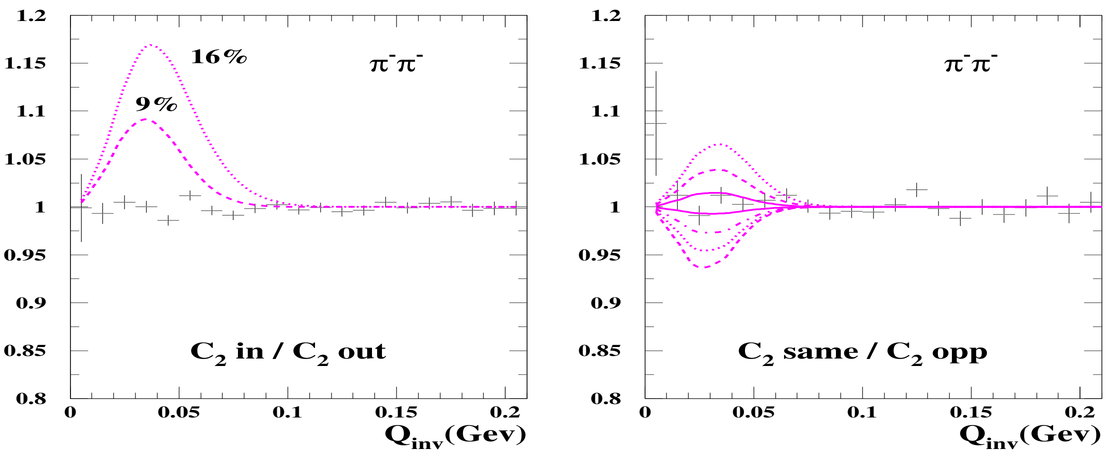

Figure 6.17: Left panel: Ratios of $C_2^{\text{``}in''}/C_2^{\text{``}out''}$: the data's $\pi^-\pi^-$ C_2 ratio overlay with a geometrical expectation of a 9% σ/σ_{geom} events' ratio and a 16% σ/σ_{geom} events' ratio. Right panel: Ratios of $C_2^{\text{``}same''}/C_2^{\text{``}opposite''}$, the data's $\pi^-\pi^-$ C_2 ratio overlay with geometrical expectations of $Ratio\left(\frac{C_2(R_1)}{C_2(R_2)}\right)\%$ (as defined in the text) of -20% (lower most curve), -14%, -8%, -2%, 4%, 10%, and 16% (upper most curve).

taneous, and we are creating an expanding source in our heavy ion collisions, then the particles that are on the outer most surface at the instant of freeze-out, will have, on average, a higher momentum, $|\vec{p}|$, than the particles that are on the inner surface. A pictorial guide is drawn in Fig. 6.18. When we make pairs to construct our C_2, the high momentum singles can make low q pairs only with close neighbors. But the low momentum singles have more choices and can make low q pairs with close and distant neighbors. Hence for high momentum singles (i.e. high average momentum pairs) that form low q pairs, the average separation between pairs will in general be small since they are made up of close neighbors. For low momentum singles (i.e. low average momentum pairs) that form low q pairs, the average separation between pairs will be in general large (larger than high average momentum pairs) because they are made up of close and distant neighbors. Thus in this simplistic picture, the radius parameters measured from C_2 will be dependent on the average pair momentum $\vec{K}$. In a more complex picture, the focusing of particles due to expansion of the source, i.e. the collective motion due to expansion, will be smeared out somewhat by the random motion imparted to each particle from an overall temperature of the source. If there is no collective motion and only random motion, $\beta_t = 0$ and $T \neq 0$, then R does not depend on $\vec{K}$. On the other extreme, if there is only collective motion and no random motion, $\beta_t \neq 0$ and $T = 0$, then R has a linear dependence on $\vec{K}$. The source that we create in heavy ion collisions lies somewhere between these two extremes. There is some degree of collective *and* random motion. Therefore when we can determine *how* R depends on $\vec{K}$, we can in principle determine the amount of

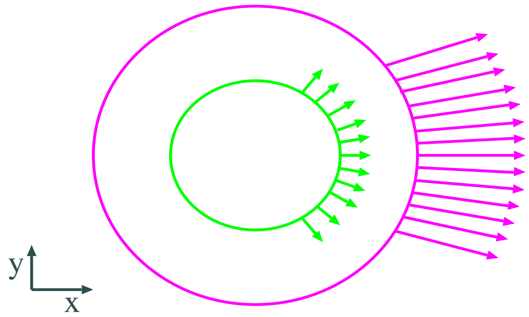

Figure 6.18: Assuming instantaneous freezeout time, the particles that are emitted from an expanding source will have different $|\vec{p}|$ depending where they are in the source at the instance of freezeout. The outer most particles will in general have a larger $|\vec{p}|$ than the inner most particles.

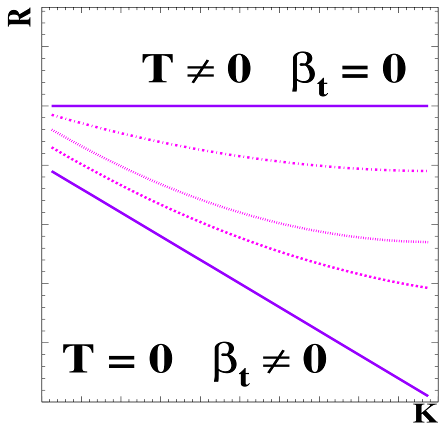

Figure 6.19: Schematic of R as a function of $\vec{K}$ for different combinations of T and β_t.

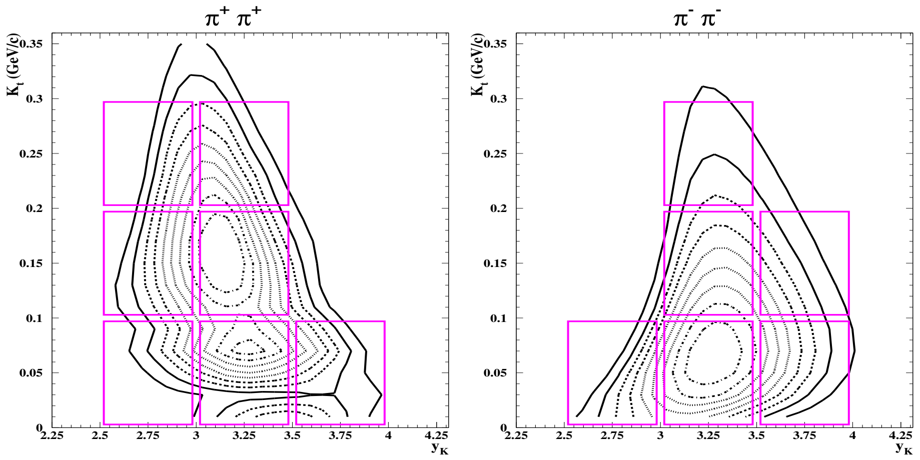

Figure 6.20: Phase space cuts of pion data set.

---

random and collective motion that exists in our source.

For our $0-10\%$ centrality data set, we divide our pion sample into ranges of $\vec{K}$ subsets. Each subset's has a width of 0.5 unit in y_K and $0.1GeV$ in K_t where:

$$y_K = \frac{1}{2} ln \frac{K_{\emptyset} + K_z}{K_{\emptyset} - K_z} \tag{6.5}$$

$$K_t = \sqrt{K_x^2 + K_y^2}. \tag{6.6}$$

The division of the data is shown in Fig. 6.20. C_2s has been constructed for each data subset. The underlying cause for the difference among the subsets of C_2 is physics driven, as shown in Appendix B.

The lowest K_t, $0. < K_t < 0.1GeV$, for π^+ acceptance contains a "hole" due to the deadened region in the DCs that the non-interacting beam particles traverse through. Even though the one and two dimensional $\pi^+\pi^+$ C_2s have sufficient statistics to extract the fit parameters for these bins, the three dimensional C_2s do not. The π^- acceptance does not suffer from this "hole" effect. We choose to concentrate only on the π^- three dimensional YKP C_2s results in the discussion which follows. For completeness of this thesis, the one, two, and three dimensional BP results for π^+ and π^-, and the three dimensional YKP results for π^+ are shown in Appendix D.

The three dimensional YKP π^- fit results are shown in Fig. 6.21 and 6.22. The results in the figures are redundant in that all the points in the y_K dependence plots on the left column are repeated to show a $m_{K_t}(=\sqrt{K_\emptyset^2 - K_z^2})$ dependence in the right column. A first observation is that there is clearly a $\vec{K}$ dependence in the radii parameters. The dependence on y_K however seems to be steeper than the dependence on m_{K_t} over our acceptance range. This primarily is due to our broader reach in y_K. The cross term parameters (R^2_{ol}, R^2_{sl}, and R^2_{os}) seem to be independent of $\vec{K}$. Additionally, $y_{source} < y_K$. A non-expanding source should show no correlation between y_{source} and y_K, while a boost invariant source should show a strict correlation between y_{source} and y_K. Recently the NA49 collaboration ($Pb + Pb$ at $158AGeV$) showed that the source they measured through the YKP parameterization of C_2s, appears to be boost invariant near y_{mid} and deviates from this, $y_{source} < y_K$, as y_K approaches y_{beam} [62]. Our measurement does not span as wide a rapidity range, but the pions that we measured are $\gtrsim y_{beam}(= 3.2)$. The trend we see for y_{source} appears to follow that observed by NA49: the source is not boost invariant near y_{beam}. This would tend to indicate that many beam rapidity π^-s are coming from lower rapidities and are boosted with the help of a thermal (random) component of the source.

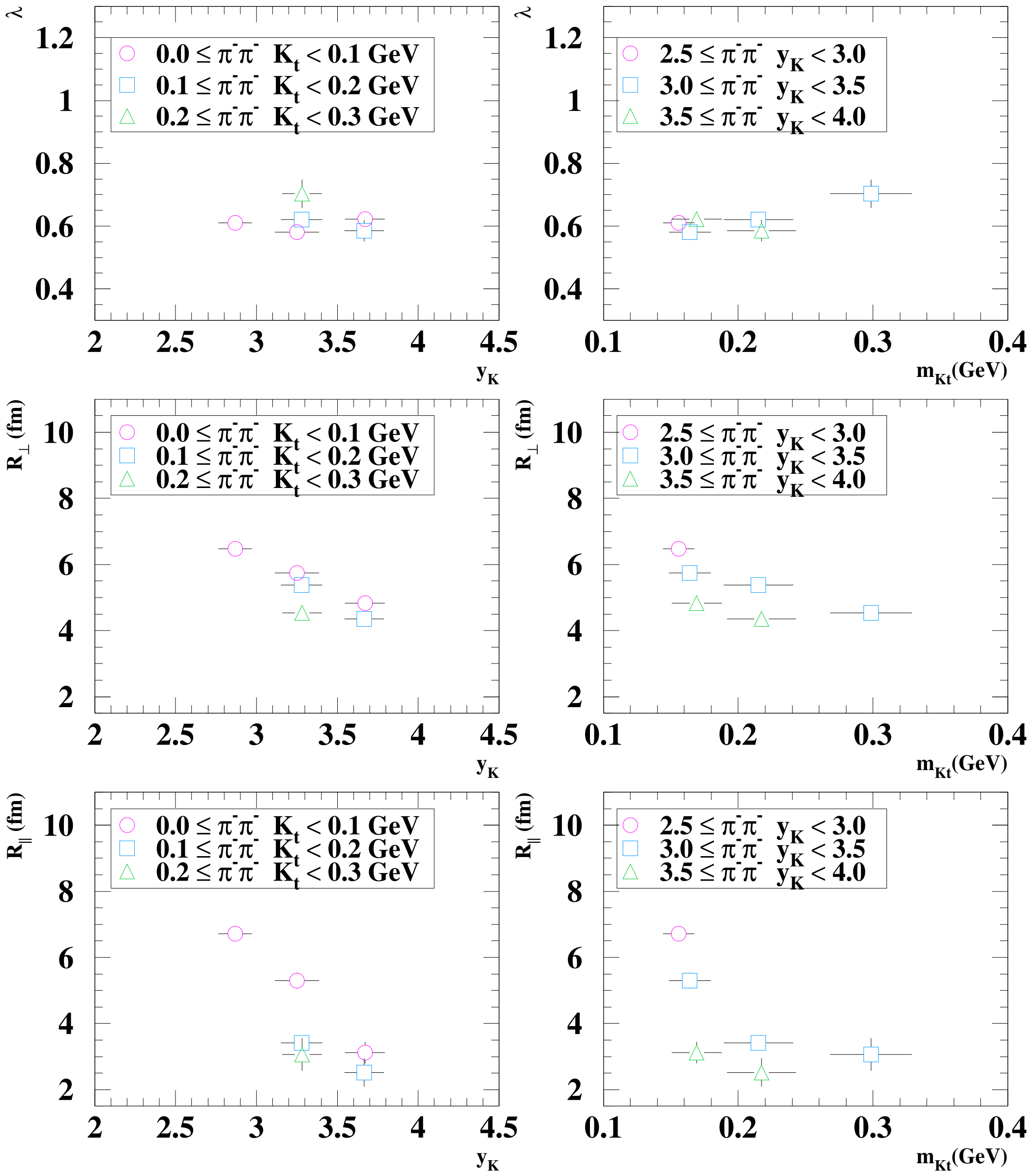

Figure 6.21: $\vec{K}$ dependence of three dimensional C_2 YKP fit parameters for $\pi^-\pi^-$ pairs. The left column shows y_K dependence. The right column shows m_{K_t} dependence.

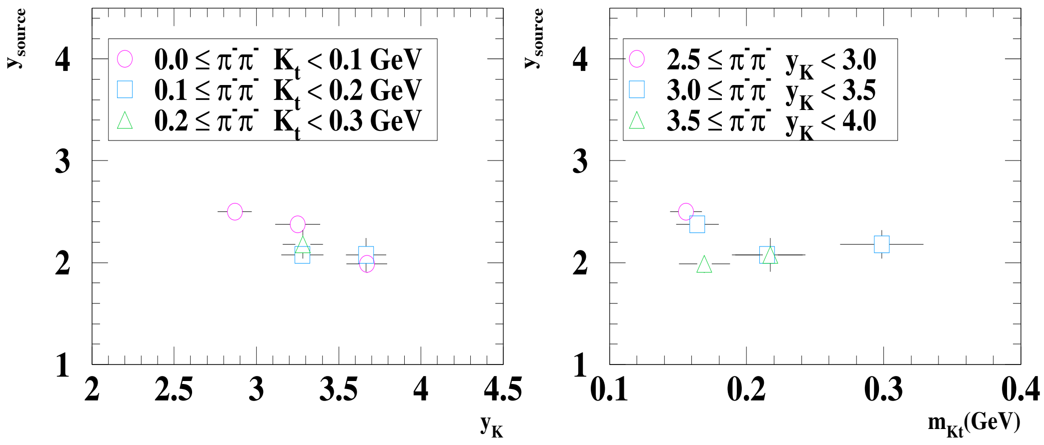

Figure 6.22: $\vec{K}$ dependence of three dimensional C_2 YKP fit parameters for $\pi^-\pi^-$ pairs. The left column shows y_K dependence. The right column shows m_{K_t} dependence.

From our measurements, there is definitively a $\vec{K}$ dependence of the one, two, and three dimensions correlation functions. The dependence is due to the existence of random and collective motion (temperature and flow) of the source. The is no model independent method of determining these global parameters of the source presently. A model dependent determination of the source's global parameters will be pursue in the next chapter.

6.3.1 Comparison to RQMD

RQMD pion pairs has been divided into $\vec{K}$ subsets to construct C_2s for comparison with data. The one dimension overlay of the C_2s are shown in Fig. 6.23 for $\pi^+\pi^+$, and Fig. 6.24 for $\pi^-\pi^-$. The overlay is generally good, except for the first few low q bins. This characteristic is consistent in all $\vec{K}$ subsets. RQMD seems to do an adequate job in reproducing the $\vec{K}$ dependence of the correlation functions. This indicate that the underlying random and collective motion of pions in RQMD are reasonable approximation to those produced in the experiment. The comparison is not completely satisfying however. RQMD is based upon a cascade of binary collisions among the produced particles. Because global characteristics of the source, such as temperature and flow velocity, are output parameters rather than inputs in RQMD, one can only say that RQMD does or does not fit the data. If RQMD does fit the data, the global parameters of the source (outputs) are then reasonable. But what the values of these global parameters are is difficult to determine because they are coupled, correlated observables [37, 63]. In the next chapter, an explicit form of the source function will be assumed. The global parameters can then be fit to the correlation radius parameters. We will be able to determine not only that the RQMD global parameters are reasonable, but also what the range of these global parameters are. This will place true limits on the source model.

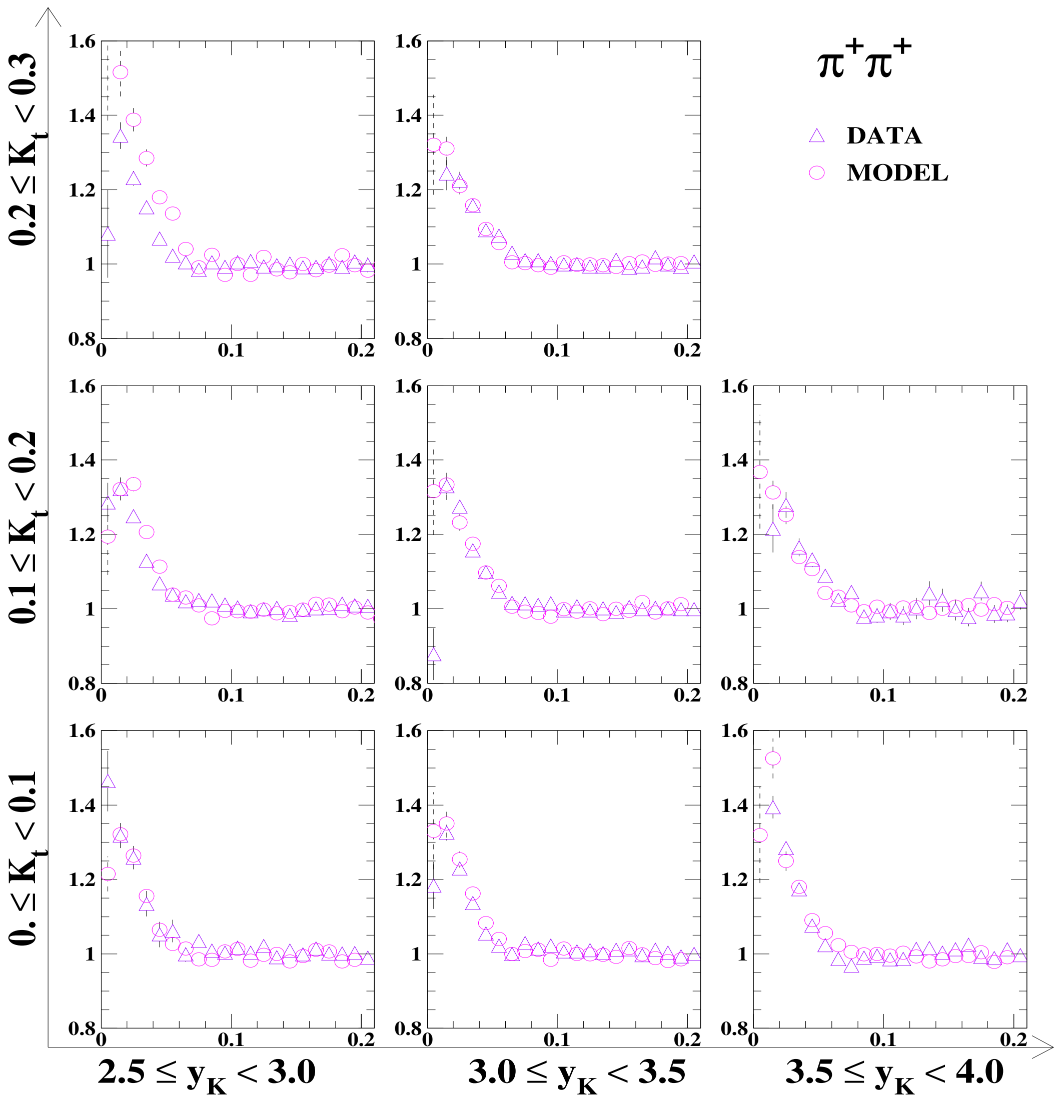

Figure 6.23: RQMD C_2s overlay with data as a function of $\vec{K}$ for $\pi^+\pi^+$ pairs.

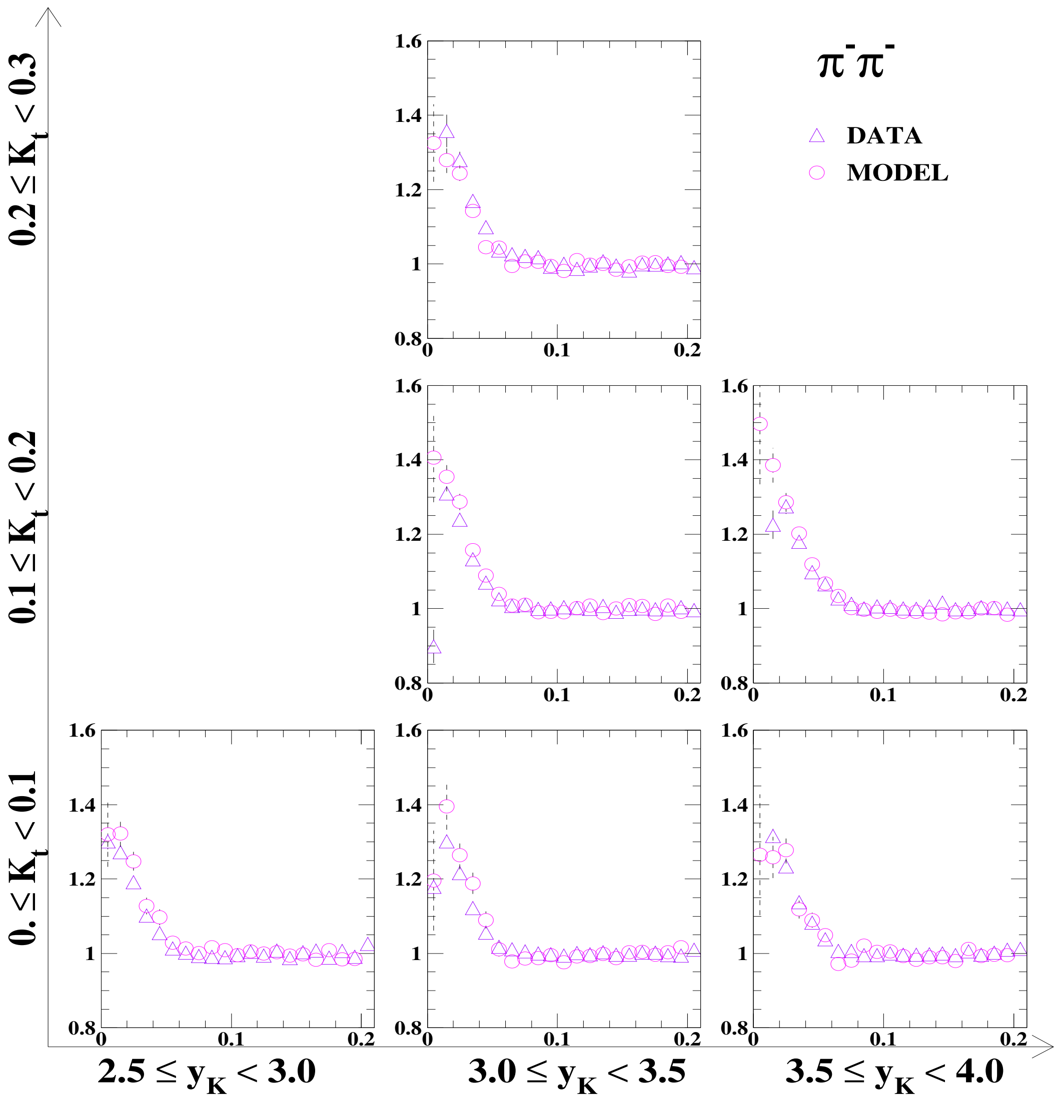

Figure 6.24: RQMD C_2s overlay with data as a function of $\vec{K}$ for $\pi^-\pi^-$ pairs.

Chapter 7

Correlation Results II

In the Sec. 6.3, we discussed the theoretical feasibility of extracting a flow velocity and temperature from the $\vec{K}$ dependence of the correlation radius fit parameters. In order to carry this out, we need to explicitly specify the form of the source function. Chapman, Nix, and Heinz have specified some "general" source function for this purpose [64]. More importantly they have shown the explicit dependence of the YKP radius parameters on the global source parameters. They chose the YKP parameterization of the correlation function because it leads more naturally back to the global source parameters than the standard BP formulation. They explored a variety of source functions, starting from the simplest ones, for instructive exercises, and adding layers of complexity that make the source function more "realistic." All the complexities culminate to one finite expanding source function with transverse flow but no resonance decays. In this model, the source function is:

$$
\begin{aligned}
S(x,K) &= \frac{m_t \cosh(\eta - Y)}{(2\pi)^3\sqrt{2\pi(\Delta\tau)^2}} \\
&\quad \exp\Big(\frac{-K\cdot u}{T} - \frac{x^2+y^2}{2R_G^2} - \frac{(\tau-\tau_0)^2}{2(\Delta\tau)^2} - \frac{\eta^2}{2(\Delta\eta)^2}\Big) \qquad (7.1)
\end{aligned}
$$

where:

$$
\begin{aligned}
u(x) &= \Big(\sqrt{1+(\frac{\beta_t r}{R_G})^2}\cosh\eta, \frac{\beta_t x}{R_G}, \frac{\beta_t y}{R_G}, \sqrt{1+(\frac{\beta_t r}{R_G})^2}\sinh\eta\Big); \\
r &= \sqrt{x^2+y^2}; \\
m_t &= m_{K_t} = \text{ transverse mass of the pair;} \\
Y &= y_K = \text{ rapidity of the pair at momentum } K; \\
\eta &= \frac{1}{2}\ln\Big(\frac{t+z}{t-z}\Big); \\
R_G &= \text{ geometrical transverse radius;} \\
\beta_t &= \text{ transverse flow velocity;} \\
T &= \text{ freezeout temperature;} \\
\tau_0 &= \text{ freezeout time;} \\
\Delta\tau &= \text{ duration of freezeout;} \\
\Delta\eta &= \text{ source width in spacetime rapidity.}
\end{aligned}
$$

This source function describes a source with a transverse expansion that is assumed to have a velocity profile of $\beta(r) = \beta_t(r/R_G)$. The source also has a non-boost invariant longitudinal expansion. Its $\Delta\eta$ cutoff term leads to a more Gaussian-like rapidity distribution. The source function, in addition, becomes a Boltzman approximation to a hydrodynamical source which freezes out at a constant temperature T and freezeout time τ_0 when $\Delta\tau \to 0$.

Fourier transforming Eq. 7.2, using Eq. 2.7, relations of the YKP radius parameters as a function of $\vec{K}$ are found [64] to be:

$$R_{\emptyset} = \Delta\tau; \tag{7.2}$$

$$R_{\perp} = R_G\Big(1+\frac{m_{K_t}\beta_t^2}{T}\cosh(y_{source}-y_K)\Big)^{-1/2}; \tag{7.3}$$

$$R_{||} = \tau_0\Big(\frac{m_{K_t}}{T}\cosh(y_{source}-y_K) - \frac{1}{\cosh^2(y_{source}-y_K)} + \frac{1}{\Delta\eta^2}\Big)^{-1/2} \tag{7.4}$$

Interestingly, we now have access to more information about the source function than we initially had hope for from correlation measurements. In addition to the flow velocity and temperature, β_t and T, which we suspect we can extract from considering the $\vec{K}$ dependence of the radius parameters, the full geometrical source size, R_G and rapidity width $\Delta\eta$, are now attainable. As an extra bonus, we also get the freezeout time, τ_0, from Eq. 7.4. Suddenly, correlation measurements return from the depths of "we don't know what we are measuring" (because of expansion) to be an incredibly rich tool to learn more than we had anticipated about the source function.

7.1 The π^-s

We use our $\pi^-\pi^-$ data that was divided into six y_K and m_{K_t} bins (i.e. the pairs data), a total of 12 data points (six $R_{||}$s and six $R_{\perp}$s), to fit simultaneously to Eq. 7.3 and 7.4. The $\pi^+\pi^+$ data, unfortunately, has too few $\vec{K}$ points (only four y_K and m_{K_t} bins) to fit to. The result of the fit to the $\pi^-\pi^-$ data is shown in Fig. 7.1. The open symbols are the fitted values that should be compared to the closed symbols of the data values. The resulting fit parameters are $R_G =$

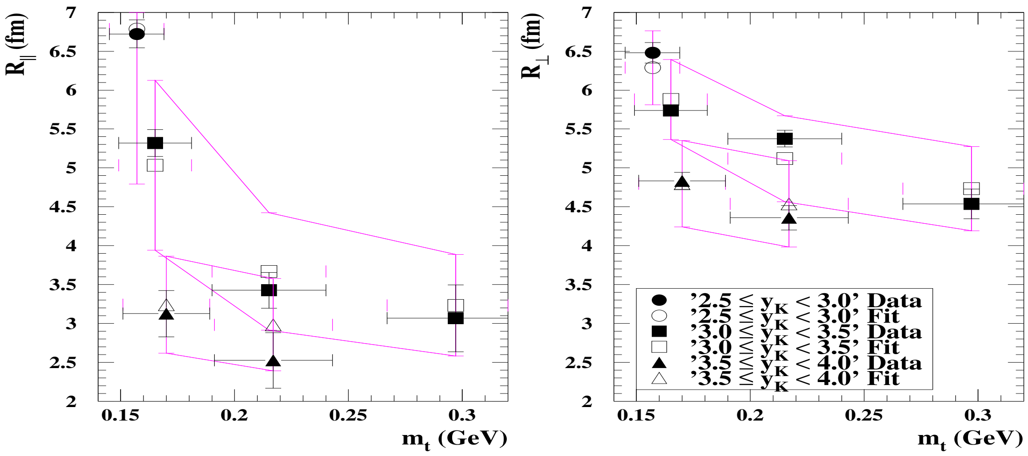

Figure 7.1: Simultaneous fits of the m_{K_t} dependence of $R_\perp$ and $R_{||}$ for $\pi^-\pi^-$ pairs.

$8.11 \pm 0.37 fm$, $\beta_t = 0.53 \pm 0.06$, $T = 0.071 \pm 0.010 GeV$, $\tau_0 = 8.21 \pm 0.9 fm$, and $\Delta\eta = 666 \pm 81200$ with $\chi^2/N_{dof} = 2.82$. In fact, the data seems to be insensitive to $\Delta\eta$. This insensitivity to $\Delta\eta$ is caused by the peculiarities of our acceptance, not an inherent limitation of the technique. When the data was fitted to Eq. 7.3 and a modified Eq. 7.4, omitting the $\Delta\eta$ term, the other fit parameters converged to the same values as stated above, to within 1σ statistical error.

It is worthwhile to remind the reader that our data are in the forward region, $y_K \gtrsim y_{beam}$. The source function, Eq. 7.2, was "designed" to include the most important features of the mid-rapidity source. Since fitting Eq. 7.4 without the $\Delta\eta$ term is technically incorrect, we can get additional help by using the measured π^- invariant multiplicities (i.e. the singles data), in the

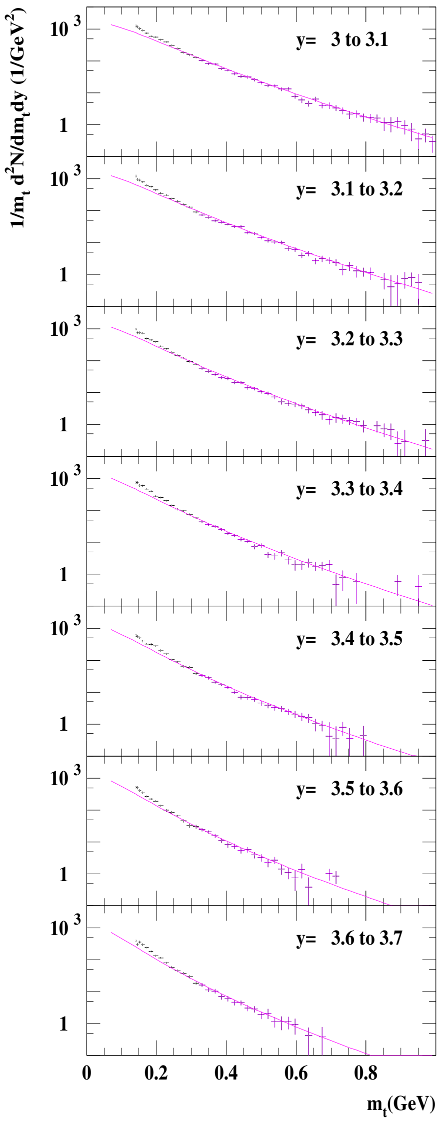

Figure 7.2: Fits of the $0-10\%$ centrality for $10.8AGeV$ $Au+Au$ system π^- singles invariant multiplicities.

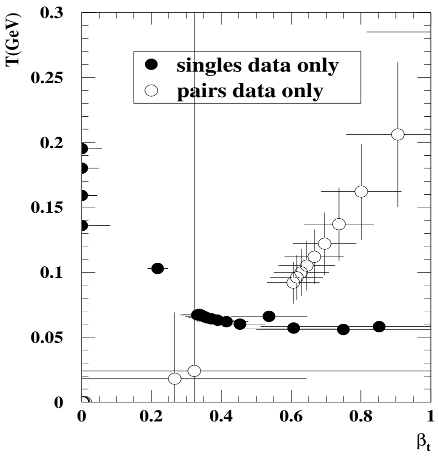

Figure 7.3: Overlay of the β_t and T correlation band obtained from the singles data alone (closed circles) with the anti-correlation band obtained from the pairs data alone (open circles).

---

framework of this same model, to help us determined $\Delta\eta$. $\Delta\eta$ is related but not exactly equal to the width of the dN/dy spectrum. The invariant multiplicity for source function Eq. 7.2 was derived in Ref. [65] to be:

$$\begin{aligned} \frac{1}{m_t}\frac{d^2N}{dm_t dy} &\propto \frac{m_t\Delta\eta_*}{1+\beta_t^2\frac{m_t}{T}}\Big(1+\frac{\Delta\eta_*^2}{2(1+\beta_t^2\frac{m_t}{T})}-\frac{m_t\Delta\eta_*^4}{8T}\Big) \\ &\exp\Big(-\frac{m_t}{T}+\frac{\beta_t^2(m_t^2-m^2)}{2T(T+m_t\beta_t^2)}-\frac{y^2}{2(\Delta\eta_*^2+T/m_t)}\Big) \qquad (7.5) \\ where \quad & \frac{1}{\Delta\eta_*^2}=\frac{1}{\Delta\eta^2}+\frac{m_t}{T}. \end{aligned}$$

The invariant multiplicities for π^-s in the $0-10\%$ centrality window for $10.8AGeV$ $Au+Au$ system are taken from Ref. [40]. One sees the familiar rise at low m_t which is successfully attributed to the Δs and other high mass resonance decays. Since the parameterized model, Eq. 7.2, does not

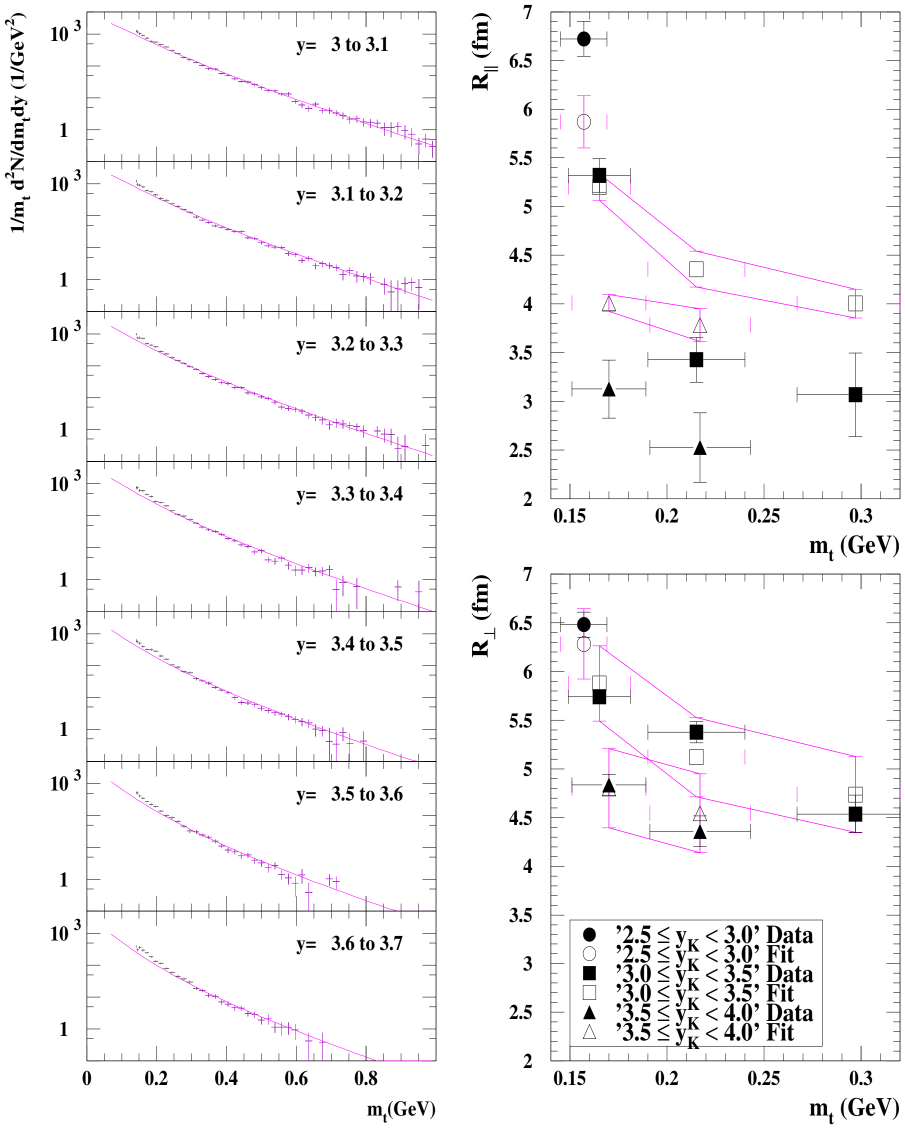

Figure 7.4: Simultaneous fits of the m_{K_t} dependence of $R_{\perp}$ and $R_{\|}$ for $\pi^-\pi^-$ pairs with the π^- singles invariant multiplicities.

include resonance decays, we are forced to perform the fit to only the high m_t tail in the rapidity regions where there is sufficient leverage for the high m_t points. Fitting Eq. 7.6 to the invariant multiplicities we arrived at the following fit parameters: $\beta_t = 0.25 \pm 0.12$, $T = 0.098 \pm 0.022$, and $\Delta\eta = 0.52 \pm 0.05$ with $\chi^2/N_{dof} = 0.50$. The data points overlaid with the fit function are shown in Fig. 7.2. The calculated yield of π^-s with these parameters is 192 ± 66. However the yield from the data, which included π^- from resonances, is ~ 130 [40]. The fact that the fit from the singles and the pair data from exactly the same acceptance window do not all overlap within statistical errors indicates that the underlying source function is likely introducing a significant systematic error in the extraction of the global parameters. Nevertheless, we thrust forward with the only data available to us.

We now have a better idea of what $\Delta\eta$ ought to be; however, it is instructive to scan the χ^2 space of both the singles and the pairs data independently as a function of $\Delta\eta$. The range of $\Delta\eta$ is chosen to be from 0.1 to 1.9, a bracket that is certainly broader than realistic values. We hold $\Delta\eta$ fixed, in intervals of 0.1, and fit the singles data to the rest of the parameters in Eq. 7.6. Independently, we also fit the pairs data to the rest of the parameters in Eq. 7.3 and 7.4 while holding $\Delta\eta$ at the fixed values. Since the only common global parameters that are accessible to both the singles and the pair data are β_t and T, we plot their converged values for each value of $\Delta\eta$ in Fig. 7.3. As can be seen from the plot, the β_t and T parameters are anti-correlated in the singles data set and are correlated in the pair data set. Fortunately the correlation of β_t and T follow distinctly different dependence in parameter space for the two data sets so that we can use their (anti-)correlation crossing to narrow the allowable β_t and T space tremendously.

During this exercise, we want to note a few observations in the values of χ^2/N_{dof} and other free parmeters. The χ^2/N_{dof} in the singles data tends to be better for *smaller* values of $\Delta\eta$. Along with the χ^2/N_{dof} indication, the calculated yield of π^- using the converged free parameters and the fixed $\Delta\eta$ is better, i.e. closer to the measured value, for $\Delta\eta \approx 0.8$. With the pairs data, the χ^2/N_{dof} tends to be better for *larger* values of $\Delta\eta$. The convergence of τ_0 fluctuate somewhat in the range of $6-8fm$. However, the convergence of R_G is amazingly constant, just above $8fm$ for all values of $\Delta\eta$ scanned.

The next obvious step is to simultaneously fit the singles data with the pairs. The results of which are plotted in Fig. 7.4 and the converged parameters are: $R_G = 8.08 \pm 0.37fm$, $\beta_t = 0.52 \pm 0.04$, $T = 0.068 \pm 0.002GeV$, $\tau_0 = 12.49 \pm 0.26fm$, and $\Delta\eta = 0.58 \pm 0.01$ with $\chi^2/N_{dof} = 0.94$. The fit is driven mostly by the singles because it contains an order of magnitude more data points than the pairs. The convergence influence of the singles data, however, is not incompatible with the pairs data. R_G remains stable and unchanged. β_t and T converge to approximately the values predicted by the crossing of the correlation and anti-correlation band in Fig. 7.3. The $R_{\|}(m_{K_t})$ does not fit the data well because the $\Delta\eta$ and τ_0 changed dramatically when we include the singles data. But the $R_{\perp}(m_{K_t})$ remains quite a good fit.

As pointed out in the early part of this thesis, correlations should no longer be considered as just a size measurement. Rather they are rich with information about the dynamics of the source. In this chapter, with the help of a model, we have explicitly remove the dynamics and extracted a full size for the source. As a by product of the procedure, we obtain values for the temperature, flow velocity, and freezeout time of the source in addition. Temperature and flow velocity have been traditionally extracted from *only the singles data.* The parameters we extracted are not in agreement with the "conventional" values of $T \approx 0.12GeV$ and $\beta_t \approx 0.39$. The trend of lower temperature and higher flow as obtained by using *both* the singles and pair data is not unique. Indeed previous applications of this technique have yielded results similiar to ours with sharply lower temperature and higher flow velocity than deduced from the singles data alone [67, 68]. However, despite the unsettling values of T and β_t, the full transverse geometrical source size is stable for the entire reasonable range of T and β_t. $R_G = 8.08 \pm 0.37fm$ for the π^- source. Accounting for Coulombic effects noted in the previous chapter, we can estimate the full source radius to be $\approx 7.5fm$. This conclusion is not far from RQMD's estimate. The size in RQMD is extracted directly from the x position distribution (y distribution is similiar to x) of the mid-rapidity π^- produced by the model. The RQMD $r.m.s_{full} \approx 7.1fm$.

We have attempted to extract global parameters that describe our π^- source with the aid of a model. First we fitted the model to the pair data alone and arrived at: $R_G = 8.11 \pm 0.37fm$, $\beta_t = 0.53 \pm 0.06$, $T = 0.072 \pm 0.010GeV$, $\tau_0 = 8.21 \pm 0.90fm$, and $\Delta\eta = 666 \pm 81200$ with $\chi^2/N_{dof} = 2.82$. Because our pair data seem to be insensitive to $\Delta\eta$, we use the singles data to get a better idea of what $\Delta\eta$ ought to be. We then fitted the singles data alone and arrived at: $\beta_t = 0.25 \pm 0.12$, $T = 0.098 \pm 0.022$, and $\Delta\eta = 0.52 \pm 0.05$. Since the T, β_t, and $\Delta\eta$ are common in the singles and the pair data, and their converged values do not overlap within statistical error bars, it is likely that the underlying model (source function Eq. 7.2) is likely introducing a significant systematic error in the extractions of these parameters. This is a result of not only the possible inadequacy of the source function but also the limited acceptance of our data. Nevertheless, we then fitted the singles and the pair data together and arrived at: $R_G = 8.08 \pm 0.37 fm$, $\beta_t = 0.52^{+0.10}_{-0.27}$, $T = 0.068^{+0.026}_{-0.002} GeV$, $\tau_0 = 12.49^{+0.26}_{-4.28} fm$, and $\Delta\eta = 0.58^{+666}_{-0.06}$ with $\chi^2/N_{dof} = 0.94$. The error bars include systematics consideration, estimated from the independent fits of the singles and the pair data.

7.2 The K^+s

In Sec. 6.1, we discussed the two possible explanations for the observation of the K^+ radius parameter being smaller then the π radius parameter. The two possibilities were: if there is a common collective motion of the system, the kaon radius parameter, owing to the kaon's larger transverse mass (than the pion's), then should be smaller than the pion's; and because the kaon interaction cross section with the surrounding nucleons is smaller than the pion's, the kaons should decouple from the system sooner than the pions. Both explanations are probably likely.

We try here to assess the likelihood of either scenerio. We first make an assumption that the two dimensional correlation measurement R_T is approximately equal to the YKP three dimensional $R_\perp$. Since we do not measure a

	$R_G^{K^+}(fm)$
Same as π^-s $T = 0.07GeV$ $\beta_t = 0.5$ $(y_{source} - y_K) = 0$	8.9
Same as π^-s $T = 0.07GeV$ $\beta_t = 0.5$ $(y_{source} - y_K) = -0.5$	9.7
"Conventional" values $T = 0.12GeV$ $\beta_t = 0.3$ $(y_{source} - y_K) = 0$	4.3
"Conventional" values $T = 0.12GeV$ $\beta_t = 0.3$ $(y_{source} - y_K) = -0.5$	4.4

Table 7.1: $R_G^{K^+}$ calculated for a variety of $(y_{source} - y_K)$, T, and β_t values using Eq. 7.3 and assuming the two dimensional $R_T \approx$ the YKP three dimensional $R_\perp$.

---

three dimensional kaon correlation, this assumption is necessary. If there is a common collective motion of the system, then the global parameters that describe the π^- source should also describe the K^+ source. We can use Eq. 7.3, and the converged T and β_t values from Sec. 7.1, to solve for $R_G^{K^+}$. Otherwise, if there is no common collective motion for the whole system, we can test a resonable range of $(y_{source} - y_K)$, T, and β_t in Eq. 7.3 to solve for $R_G^{K^+}$. The resulting $R_G^{K^+}$ for a variety of $(y_{source} - y_K)$, T, and β_t are summarized in Table 7.1. The ambiguity in the kaon flow is sufficient to tolerate results ranging from the kaon geometrical source size being 0.5 to 1.2 times the pion geometrical source size.

Chapter 8

Conclusions

In this thesis we have measured two bosonic particle correlations using π^+s, π^-s, and K^+s from central and semi-peripheral $Au + Au$ collisions at $11.5 AGeV$. The conventional purpose of correlation measurements is to discover the size of the particle emitting source. But due to dynamics of the source, the radius parameters extracted from C_2 is a minimum value for the full source size. With the advent of theoretical developments and luck of the experimenter, C_2 not only can be corrected to yield the full size of the source, but it can also provide us with a measure of the dynamic observables of the source and subtler content such as Coulomb interaction with the surrounding matter.

Study of pion correlations as a function of reaction plane angle has been done. The azimuthal asymmetry is at most 8% for π^+ source and 6% for the π^- source. It appears that the hadronic stage of the system has little recollection of its initial asymmetry; this is the primary difficulty in using hadrons to search for early stage effects such as a phase transition.

Study of pion correlations as a function of average pair momentum, $\vec{K}$, has also been done. It is definitive that the measured radius parameters do vary with $\vec{K}$ due to the dynamic nature of the source. However, to extract values for these dynamical parameters, and the actual size of the source, we must rely on model assumptions and explicitly formulation of a source function. Fitting the singles and the pair data to a specific source function, we arrived at $R_G = 8.08 \pm 0.37 fm$, $\beta_t = 0.52^{+0.10}_{-0.27}$, $T = 0.068^{+0.026}_{-0.002} GeV$, $\tau_0 = 12.49^{+0.26}_{-4.28} fm$, and $\Delta\eta = 0.58^{+666}_{-0.06}$ with $\chi^2/N_{dof} = 0.94$. The converged value of R_G also agrees with that deduced from RQMD mid-rapidity π^-s spatial distribution. We have also attempted to put a limit on the range of the actual size of the K^+ source. For the K^+ pairs, if the two dimensional R_T is assumed to be approximately the same as the YKP three dimensional $R_\perp$, then with the "conventional" and our "un-conventional" values of temperature and flow velocity assumptions , $R_G^{K^+} \approx 0.5 - 1.2 R_G^{\pi^-}$.

The size of the π^- source we deduced, from a finite expanding source function model and RQMD, is larger than the initial size of the colliding system (r.m.s of Au nucleus $\sim 7/\sqrt{5} fm$). The intial system's asymmetry is nearly forgotten in the final hadronic state. Cumulatively this means that the system's final state is probably dilute and insensitive to the interesting earlier stage effects. The K^+s however, may offer us a chance to look into the earlier stage (earlier than the pions) and offer us the possibility of detecting interesting effects. The first step to utilize the K^+s is to make the same correlation as a function of $\vec{K}$ study as we have done here for the π^-. The limited statistics of current data prevented us from making this study for the K^+s. The limitation of present data sets is due to the lower luminosity and the inability to identify higher momentum kaons because of contamination from neighboring pions and protons. But with future colliders, RHIC and LHC, not only will they run at higher luminosity than the AGS and CERN SPS, but they, being colliders (the system's center of mass frame is the lab frame), will be able to identify higher momentum kaons without contamination from the pions and protons. With the data from future experiments at RHIC (and LHC), detailed measurements of kaons correlations to extract global parameters for the kaon source will not be difficult.

Bibliography

[1] E. Laermann, Nucl. Phys. A **610** (1996) 1c.

[2] B. Müller, Rep. Prog. Phys. 611-636 **58** (1995).

[3] Proceedings of the Quark Matter International Conferences on Ultra-relativistic Nucleus-Nucleus Collisions from 1983 to 1997.

[4] I. Ravinovich, Nucl. Phys. A **638** (1998) 159c.

[5] L. Ramello, Nucl. Phys. A **638** (1998) 261c.

[6] H. Liu, Nucl. Phys. A **638** (1998) 451c.

[7] U. Heinz, Proceedings for the 2^{nd} Catania Relativistic Ion Studies: "Measuring the Size of Things in the Universe: HBT Interferometry and Heavy Ion Physics," Acicastello, Italy (1998); hep-ph/9806512.

[8] R. Hanbury-Brown, and R.Q. Twiss, Nature **178** (1956) 1046.

[9] G. Goldhaber, S. Goldhaber, W. Lee, and A. Pais, Phys. Rev. (1960) 120.

[10] B. Lörstad, Int. J. Mod. Phys. A **4** (1989) 2861.

[11] D. Boal, C.K. Gelbke, and B.K. Jennings, Rev. Mod. Phys. **62** (1990) 553.

[12] U. Heinz, Proceedings of International Summer School on Correlations and Clustering Phenomena in Subatomic Physics, Dronten, Netherlands (1996); nucl-th/9609029.

[13] S. Pratt, Phys. Rev. Let. **53** (1984) 1219.

[14] G.F. Bertsch, Nucl. Phys. A. **498** (1989) 173c.

[15] S. Pratt, T. Csörgő, J. Zimányi, Phys. Rev. C **42** (1990) 2646.

[16] J.D. Bjorken, Phys. Rev. D., **27** (1983) 140.

[17] S. Pratt, Phys. Rev. D **33** (1986) 1314.

[18] S. Chapman, P. Scotto, U. Heinz, hep-ph/9409349v2; U. Heinz, Nucl. Phys. A **610** (1996) 264c; U. Heinz, B. Tomášik, U.A. Wiedemann, Wu Y.F., Phys. Lett. B **383** (1996) 181.

[19] S. Chapman, P. Scotto, U. Heinz, Heavy Ion Phys. **1** (1995) 1.; S. Chapman, P. Scotto, U. Heinz, Phys. Rev. Lett. **74** (1995) 4400; U.A. Weidemann, P. Scotto, U. Heinz, Phys. Rev. C **53** (1996) 918.

[20] S. Chapman, J.R. Nix, U. Heinz, Phys. Rev. C. **52** (1995) 2694.

[21] F. Yano, S. Kooni, Phys. Lett. B **78** (1978) 556.

[22] M.I. Podgoretskiĭ, Sov. J. Nucl. Phys. **37** (1983) 272.

[23] M. Gyulassy, S. Kauffmann, and L.W. Wilson, Phys. Rev. C **20** (1979) 2267.

[24] R. Lednicky, and M.I. Podgoretskiĭ, Sov. J. Nucl. Phys. **30** (1979) 432.

[25] P. Grassberger, Nucl. Phys. **120** (1977) 231; M. Gyulassy, and S.S. Padula, Phys. Lett. B **217** (1988) 181.

[26] M.S. Muthuswamy, PhD thesis, SUNY at Stony Brook (1992).

[27] B. Hong, PhD thesis, SUNY at Stony Brook (1995).

[28] L.S. Waters, PhD thesis, SUNY at Stony Brook (1990).

[29] Z. Zhang, PhD thesis, University of Pittsburgh(1993).

[30] J. Simon-Gillo, PhD thesis, Texas A&M University (1992).

[31] Z. Zhang, P. Braun-Munzinger, W.E. Cleland, G. David, and D. Lissauer, Nucl. Instr. Meth. **A343** (1994) 610.

[32] W.J. Llope, PhD thesis, SUNY at Stony Brook (1991).

[33] R. Bersch, MSI Dissertation, SUNY at Stony Brook (1995).

[34] S.V. Green, PhD thesis, Yale University (1992).

[35] R. Lacasse, J. Barrette, Y. Dai, K. Filimonov, S. Gilbert, S.K. Mark, C. Pruneau, M. Rosati, Y.J. Qi, G. Wang, Nucl. Instr. Meth. **A408** (1998) 408.

[36] Y. Kwon, PhD thesis, SUNY at Stony Brook (1997).

[37] S.C. Johnson, PhD thesis, SUNY at Stony Brook (1997).

[38] http://wwwinfo.cern.ch/asd/paw.

[39] W.C. Chang, PhD thesis, SUNY at Stony Brook (1997).

[40] T.W. Piazza, PhD thesis, SUNY at Stony Brook (1997).

[41] Y. Dai, PhD thesis, McGill University (1998), to be published.

[42] Y. Zhang, PhD thesis, SUNY at Stony Brook (1995).

[43] K. Filimonov, PhD thesis, McGill University (1998), to be published.

[44] J. Dee, PhD thesis, SUNY at Stony Brook (1995).

[45] C.M. Zou, PhD thesis, SUNY at Stony Brook (1996).

[46] M. Pollack, PhD thesis, SUNY at Stony Brook (1997).

[47] K. Shigaki, PhD thesis, University of Tokyo (1995).

[48] G.I. Kopylov, Phys. Lett. **B50** (1974) 472.

[49] S. Panitkin, PhD thesis, SUNY Stony Brook (1997).

[50] D. Miśkowiec, E877 collaboration notes, 18 April 1997.

[51] A. Messiah *Quantum Mechanics Volume I*, Appendix B, North Holland, Amsterdam, 1961.

[52] M.D. Baker, private communication.

[53] P.R. Bevington, D.K. Robinson, *Data Reduction and Error Analysis for the Physical Sciences*, McGraw-Hill Inc., New York, 1992.

[54] http://wwwinfo.cern.ch/asd/cernlib/minuit/minmain.html

[55] Computer code provided by H. Sorge, at http://alba.physics.sunysb.edu/ sorge/rqmd.html; H. Sorge, H. Stöcker, W. Greiner, Ann. Phys. (NY) **192** (1989) 266; A. Jahns, H. Sorge, H. Stöcker, W. Greiner, Z. Physik **341** (1992) 243.

[56] Computer code provided by S. Pratt, at http://www.nscl.msu.edu/ pratt/freecodes/crab/home.html; method described in detail in S. Pratt, T. Csörgo, J. Zimányi, Phys. Rev. **C42** (1990) 2646.

[57] D. Miśkowiec, Nucl. Phys. A **610** (1996) 227c.

[58] J. Barrette *et al*,(E814 Collaboration) Phys. Lett. B **333** (1994) 33.

[59] C. Ogilvie, Nucl. Phys. A **638** (1998) 57c.

[60] G. Baym, P. Braun-Munzinger, Nucl. Phys. A **610** (1996) 286c.

[61] J. Barrette *et al.*, (E877 Collaboration) Phys. Rev. C **56** (1997) 3254; Phys. Rev. C **55** (1997) 1420; Phys. Rev. C **51** (1995) 3309; Phys. Rev. Lett. **70** (1993) 2996.

[62] H. Appelshäuser *et al.*, (NA49 Collaboration) Eur. Phys. J. C **2** (1998) 661.

[63] S. Esumi, S. Chapman, H. van Hecke, Nu Xu, Phys. Rev. C **55** (1997) R2163.

[64] S. Chapman, J.R. Nix, U. Heinz, Phys. Rev. C **52** (1995) 2694.

[65] S. Chapman, P. Scotto, U. Heinz, Heavy Ion Physics **1** (1995) 1.

[66] P. Braun-Munzinger, J. Stachel, J.P. Wessels, Nu Xu Phys. Lett. **B344** (1995) 43; Phys. Lett. **B365** (1996) 1.

[67] S. Chapman, and J.R. Nix, Phys. Rev. C **54** (1996) 866.

[68] J.R. Nix, D. Strottman, H.W. van Hecke, B.R. Schlei, J.P. Sullivan, and M.J. Murray, Proceedings of the 14th Winter Workshop on Nuclear Dynamics, Snowbird, Utah (1998); nucl-th/9801045.

[69] T. Peitzmann, Z. Phys. C **44** (1992) 485.

Appendix A

Fitting the Wrong Assumed Function to the Data Distribution

A major assumption in the process of extracting source function information from pion correlations is that the source itself *must be Gaussian*, or that we are measuring *only the Gaussian part.* If this assumption is wrong, then our extracted source function information is highly dependent on the distribution of our data points and their associated errors [69].

A.1 A Simple Example: Generated Correlation

In Fig. A.1, I have created "data" points with an underlying distribution of functional form:

$$C_2(Q_{inv}) = 1. + 0.5e^{-6^2 Q_{inv}^2}. \tag{A.1}$$

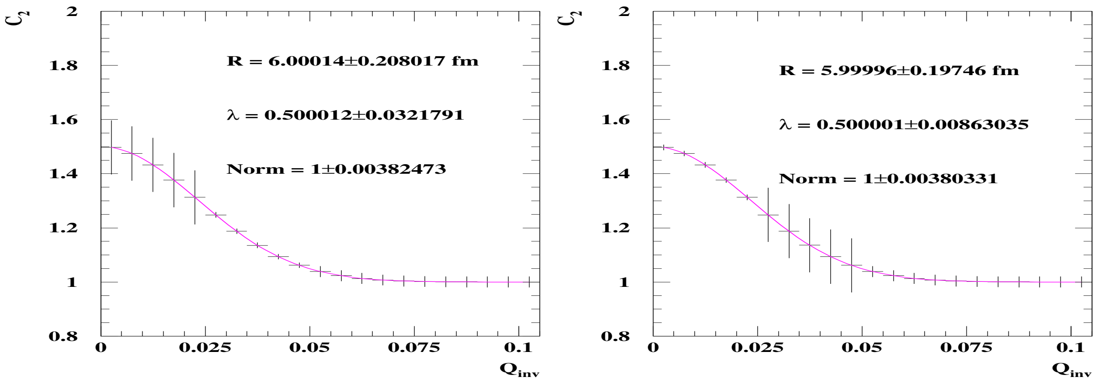

Figure A.1: Simulated data points with Gaussian underlying distribution fitted to a Gaussian function. The left panel is where data in the $0.025GeV < Q_{inv} < 0.05GeV$ region is well measured while the right panel is where data in the same region is not well measured.

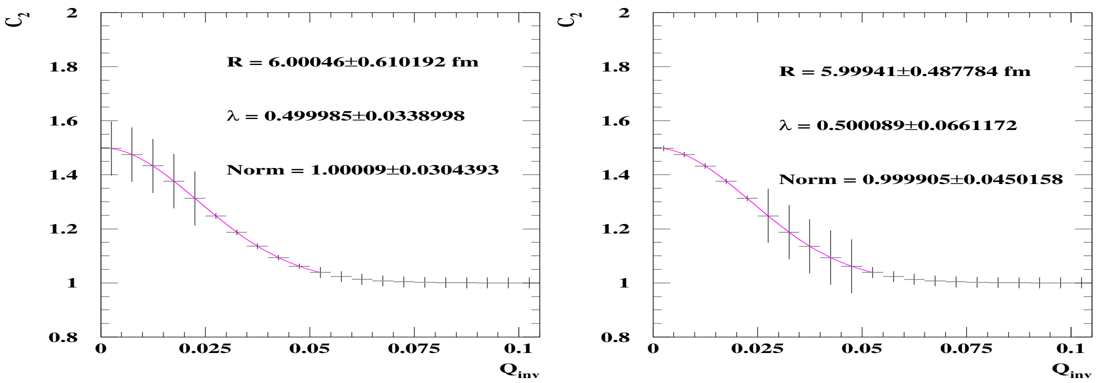

Figure A.2: Simulated data points with Gaussian underlying distribution fitted to a Gaussian function in a limited range.

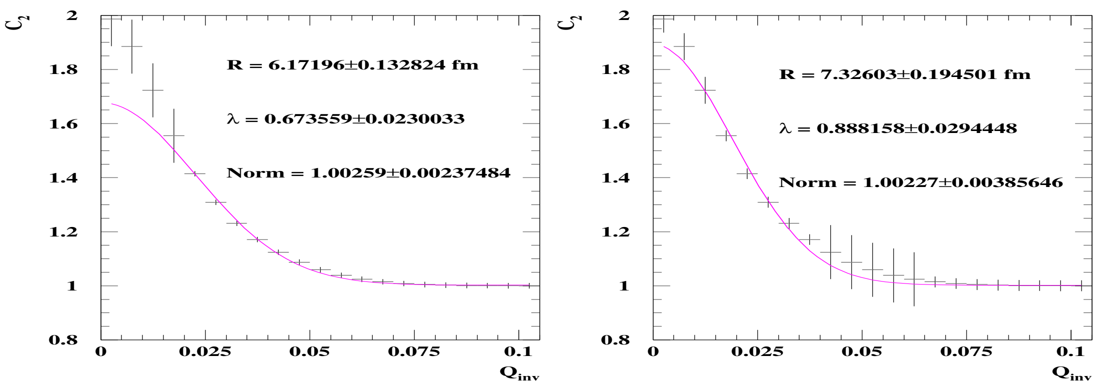

Figure A.3: Simulated data points with a non-Gaussian underlying distribution fitted to a Gaussian function. The left panel is where data in the $0.025GeV < Q_{inv} < 0.05GeV$ region is well measured while the right panel is where data in the same region is not well measured.

Fig. A.1 - left panel - is representative of data which are well measured in the $0.025GeV < Q_{inv} < 0.05GeV$ region while Fig. A.1 - right panel - represents data which are not so well measured in the same area. The fit function I used to fit these simulated data is:

$$C_2(Q_{inv}) = Norm(1. + \lambda e^{-R^2 Q_{inv}^2}) \tag{A.2}$$

where R, λ, and $Norm$ are the fit parameters. Because the underlying distribution of the data points is the same as the fit function's form, the extracted fit parameters are close to the actual input parameters used to create the "data" points. Even if the fit range is limited, as in Fig. A.2, the extracted fit parameters are still representative of the input parameters for the distribution.

A counter example is where the data points are created from a non-

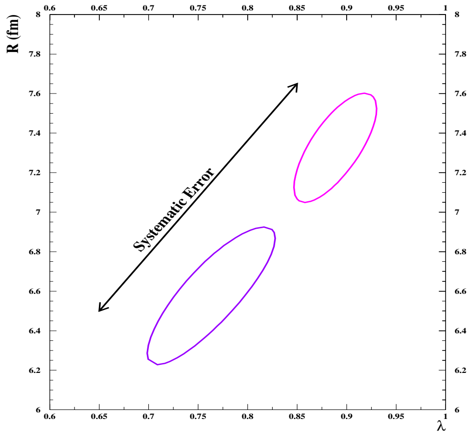

Figure A.4: One sigma contours showing the correlations of fit parameters λ and R_{inv} for fit results from Fig. A.3. The bottom ellipse is for the fit result of the left panel of Fig. A.3. The top ellipse is for the fit result of the right panel of Fig. A.3.

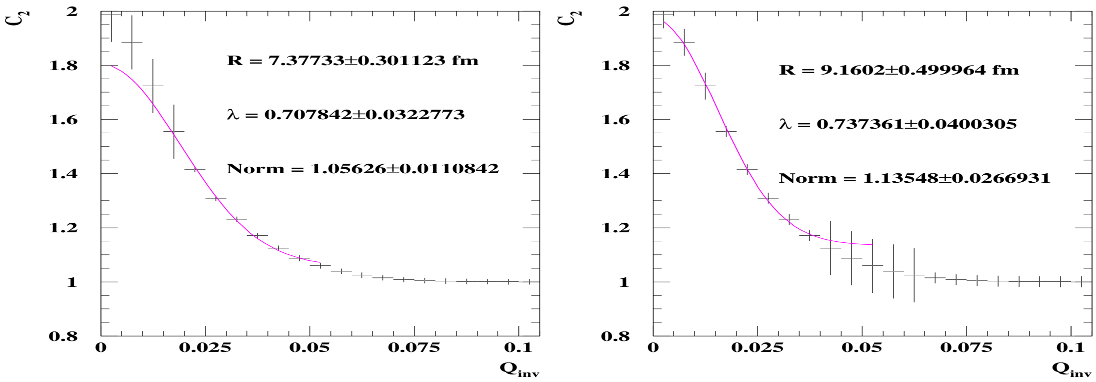

Figure A.5: Simulated data points with a non-Gaussian underlying distribution fitted to a Gaussian function in a limited range.

Gaussian distribution. Fig. A.3 show data points created from:

$$C_2(Q_{inv}) = 1 + 0.5e^{-6^2Q_{inv}^2} + 0.5e^{-20^2Q_{inv}^2} \tag{A.3}$$

The left panel of Fig. A.3 is where data in the $0.025GeV < Q_{inv} < 0.05GeV$ region is well measured while the right panel is where data in the same region is not well measured. The "data" is fitted to Eq. A.2. Because the underlying distribution is not Gaussian, the extracted fit parameters is highly dependent on the distribution of the errors of the data points. In addition, the fit parameters are highly correlated. One sigma contours showing the correlation of the fit parameters λ and R_{inv} for each of the left and right panel of Fig. A.3 are shown in Fig. A.4. Correlated changes of fitted λ and R_{inv} (movement along the major axis of the contour ellipse), for our particular example, is all attributed to systematic error. In reality, since we do not know the underlying distribution of the data, we cannot exclude physics causes for the difference between two C_2s, that when displaying their correlated fit parameters contour, looks like movements along the major axis of the contour ellipses. But we can certainly include systematic error, at least, as a partial cause of correlated changes of the fit parameters.

Limiting the range of the fit also has a highly volatile effect on the extracted fit parameters, as shown in Fig. A.5. This particular pitfall, not having enough range to fit to, will be demonstrated and examined in the real data in the next section.

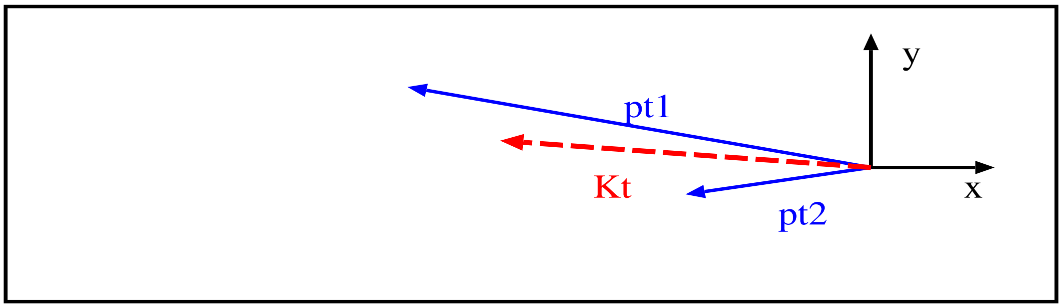

Figure A.6: Looking up stream at the E877 collimator opening, for most pairs, K_t is pointed in the lab x direction. Thus the *out* direction is also pointed in the x direction.

A.2 A Complex Example: The Measured Correlation

E877 has a limited aperture. The collimator opening has more acceptance in lab coordinate x than y. Thus for pair acceptance, the K_t of the pair is mostly pointing in the lab x direction, see example in Fig. A.6. By definition of the *out*, *side*, *long* coordinate, since *out* is parallel to K_t, then *out* is mostly in the lab x direction. The *side* direction then is mostly in the lab y direction. Because of E877's very limited y acceptance, this has a dramatic consequence in the $\vec{q}$ range of the pair, specifically the q_s range of the pair. Fig. A.8 shows two dimensional projections of $C_2(q_s, q_l)$ for consecutive slices of q_o values. Fig. A.7 schematically show what each plot in Fig. A.8 is, in "3 dimensional" space: $q_i = q_o$, $q_j = q_s$, and $q_k = q_l$. The limited lab y opening of the E877 collimator is evident in the limited measured range of q_s, as seen in Fig. A.8.

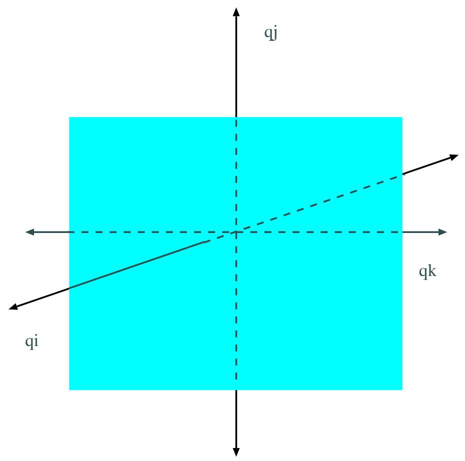

Figure A.7: A schematic of a two dimensional slice of a three dimensional C_2. The slice is $C_2(q_j, q_k)|_{q_i}$.

The range of coverage of q_o is larger because of the larger lab x opening of the collimator. The range of coverage of q_l is larger because the spectrometer sits in forward rapidity. It is clear that $|q_o|$ and $|q_l|$ extend beyond $0.15GeV$, the scope of what is shown in the plots. Note that the range of q_s is even narrower for $|q_o|, |q_l| < 0.05GeV$, where the correlation signal exists. Projections of C_2 onto one q_i are shown in Fig. A.9. Here it is also obvious that q_s has a very limited range of coverage by our apparatus.

As an exercise, to examine the sensitivity of the fit parameters with respect to "the amount of coverage" that we allow the fitting procedure to fit to, we devised the following. The edge of q_s coverage is parameterized as a function of q_o and q_l, i.e. each plot in Fig. A.8 (each q_o) is parameterized as a fuction of q_l. This edge is systematically cut away and fitted to extract R_o,

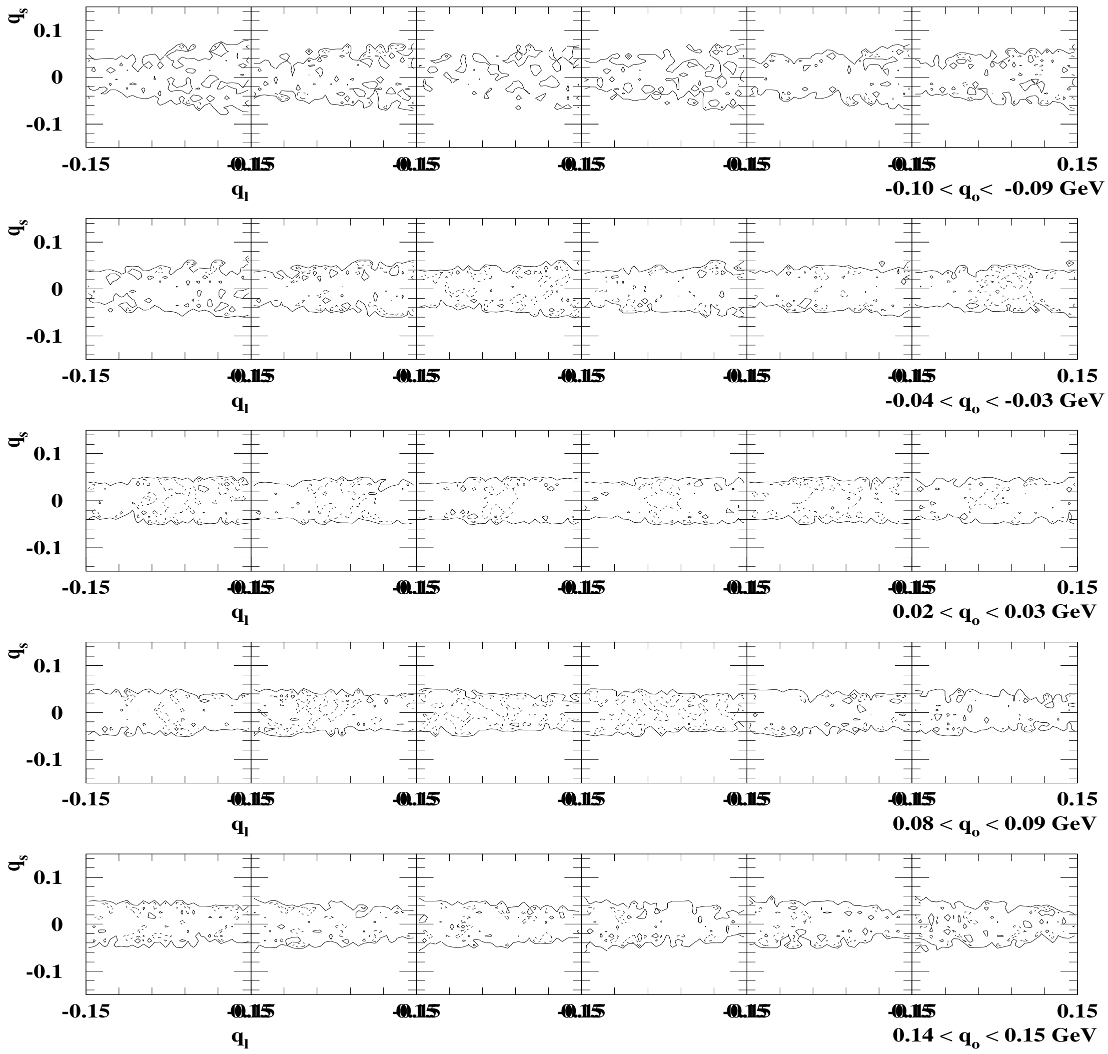

Figure A.8: Two dimensional slices of $C_2(q_s, q_l)|_{q_o}$. The upper left corner is a slice for $-0.15GeV < q_o < -0.14GeV$. Subsequent plots are for consecutive $0.01GeV$ of q_o slices. Hence the lower right corner is a slice for $0.14GeV < q_o < 0.15GeV$. The limited range of q_s is discussed in the text.

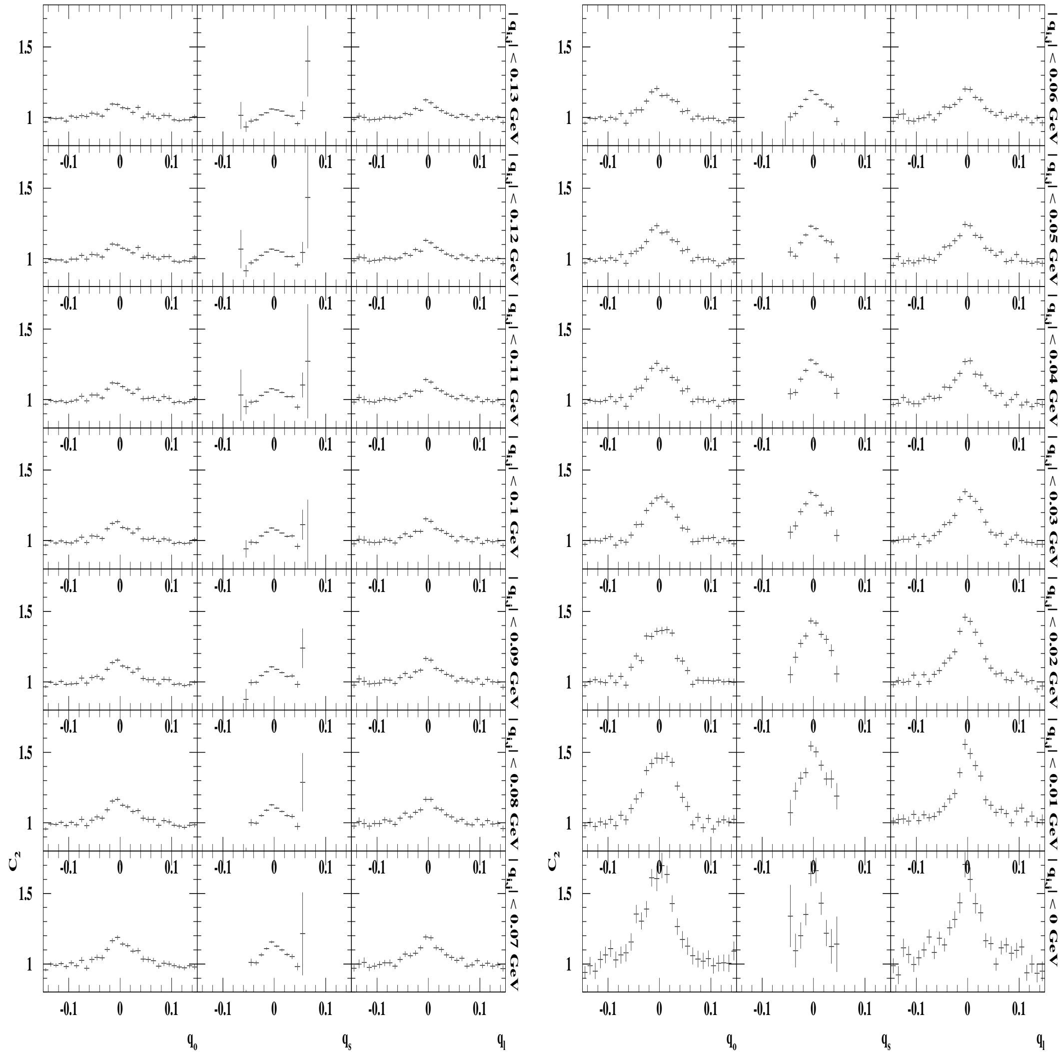

Figure A.9: One dimensional projections of $C_2(q_o, q_s, q_l)$. The range of integration is indicated on the right side of each row of plots.

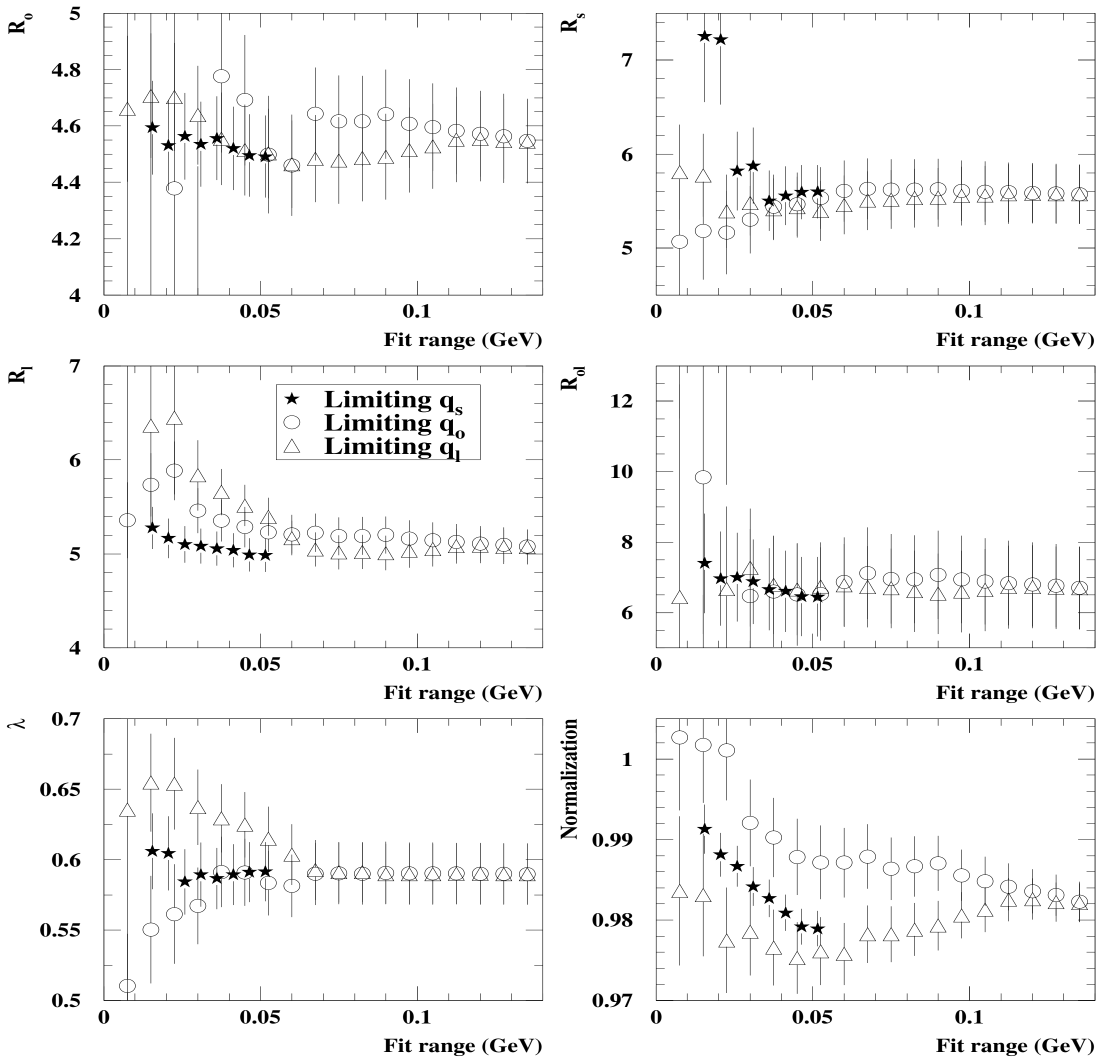

Figure A.10: Limiting q_i, $(i = o, s, l)$, to examine the convergence of the fit parameters. See text for discussion.

R_s, R_l, R_{ol}, λ, and $Norm$, using Eq. 5.17. The extra parameter $Norm$ is used to allow for an overall vertical shift of the correlation. The extracted fit parameters are plotted as a function of how much is cut away - more quantatively as a function of the absolute value of the range of q_s at $q_o, q_l = 0$ in Fig. A.10 (the star symbols). Limiting the range of q_o and q_l also yields a similar trend of extracted fit parameters (open circles and triangles in Fig. A.10). As there is less q_i to fit to, the parameters diverge. This is most evident in the λ and $Norm$ parameters, analogous to of our previous section's simple example in Fig. A.5. We can conclude that the convergence of the fit parameters, at large q coverage, is the most stable values. This then leads us to argue that we cannot measure R_s due to the limiting coverage of q_s. Eventhough it looks as if R_s does converge to some value, we must be reminded that for large q_o and q_l coverage points, there is still a limited coverage of q_s. The star symbol does not extend beyond $\approx 0.05GeV$; therefore we cannot speculate about the value of convergence of R_s in the upper right hand corner plot in Fig. A.10. We conclude that since we have far enough reach in q_o and q_l, R_o and R_l are then well measured. But due to the limiting reach of q_s, R_s is measured with an unknown uncertainty. This uncertainty is very sensitive to the distribution of the error bars of the data points.

Appendix B

Assessing Underlying Cause of $\vec{K}$ Dependence of C_2s

In order to assess that a C_2 of one $\vec{K}$ subset is different from another, we plot the one sigma contour of the correlation of the fit parameters λ and R_{inv} for each one dimensional C_2 in Fig. 6.20, using what we have learned in Appendix A. We do not believe that the underlying function of a C_2 is truly Gaussian although it is fitted as such. As a result one must take care before drawing conclusions about differences based only on the statistical error bars because there exists a systematic error correlating the radius and the λ parameters. Showing that the correlations of the R_{inv} and λ do scatter across parameter space is sufficient to demonstrate that there are physics driven differences in the data samples. The R_{inv} and λ correlation contours for $\pi^+\pi^+$ data subsets are shown in Fig. B.1 left panel; the contours for $\pi^-\pi^-$ data subsets are shown in Fig. B.1 right panel. The fact that the contours are scattered in the λ and R_{inv} parameter space implies there are underlying physics differences between any two correlations.

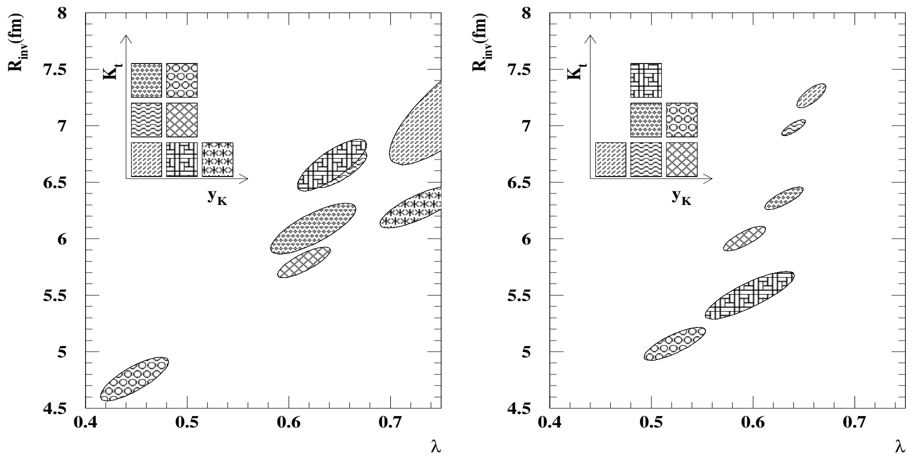

Figure B.1: 1σ χ^2 contours of one dimensional correlations' fit parameters, for $\pi^+\pi^+$ on the left panel, for $\pi^-\pi^-$ on the right panel.

Appendix C

The Stability of the YKP Parameterization of C_2

The energy component of the momentum difference, $q_\emptyset$, has a small coverage only at small $\vec{q}$. This is obvious from:

$$\begin{aligned} q_\emptyset = E_1 - E_2 &= \sqrt{m^2 + \vec{p}_1^2} - \sqrt{m^2 + \vec{p}_2^2} \\ &\quad \text{for } \vec{p}_1 \approx \vec{p}_2 = \vec{p} \\ &\approx \sqrt{m^2 + \vec{p}^2} - \sqrt{m^2 + \vec{p}^2} = 0. \end{aligned} \tag{C.1}$$

Therefore $q_\emptyset$'s coverage is limited for small $\vec{q}$ but it is extended at larger $\vec{q}$. This is seen in the $q_{||}$ slice contour plots of $q_\perp$ vs $q_\emptyset$ in Fig. C.1. The movement of the data from low $q_{||}$ value slice to high $q_{||}$ value slice is a consequence of $y_{analysis} = 2.73 \neq y_{source}$. If this movement of the data is confusing to the reader, we can look at the integrated one dimensional projections of $C_2(q_\perp, q_{||}, q_\emptyset)$ to see the same point in Fig. C.2.

The measurement of $\Delta\tau$ is restricted by the inherent $q_\emptyset$ limit of identical particles correlations given our statistics. Whether $\Delta\tau$ is measured accurately

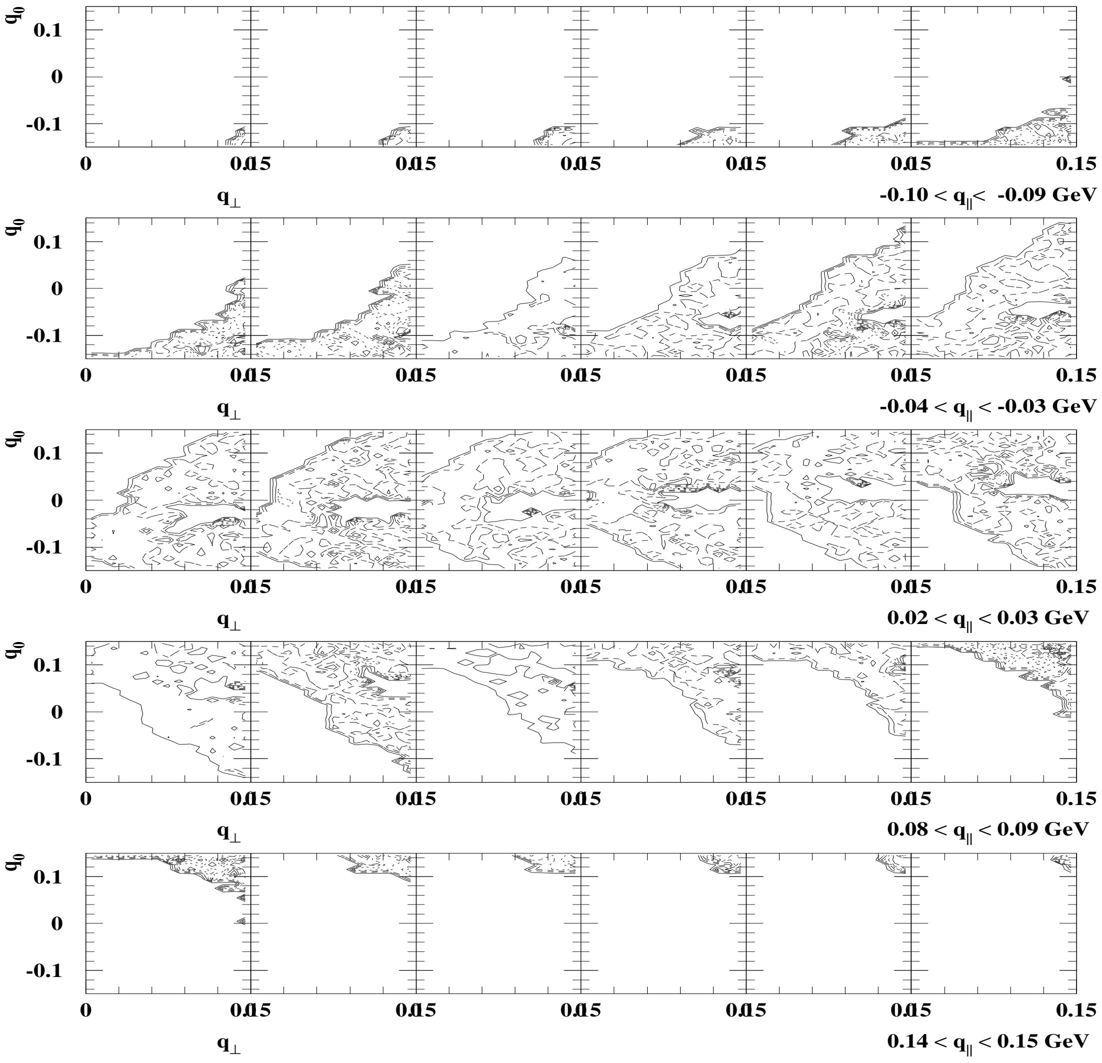

Figure C.1: Two dimensional slices of $C_2(q_\perp, q_\emptyset)|_{q_\|}$. The upper left corner is a slice for $-0.15GeV < q_{||} < -0.14GeV$. Subsequent plots are for consecutive $0.01GeV$ of $q_{||}$ slices. Hence the lower right corner is a slice for $0.14GeV < q_{||} < 0.15GeV$. The apparent limited range of $q_\emptyset$ and the movement of the data are discussed in the text.

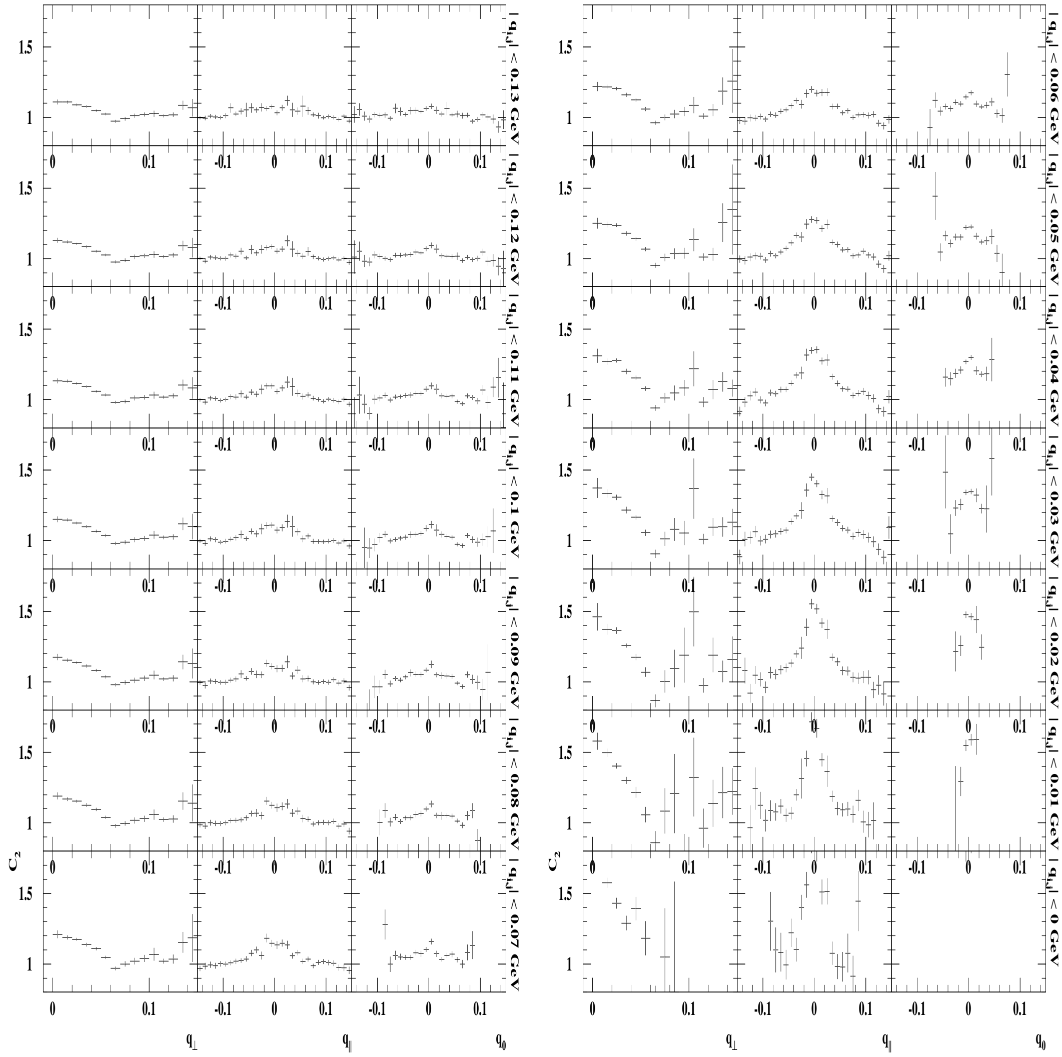

Figure C.2: One dimensional projection of $C_2(q_\perp, q_{||}, q_\emptyset)$. The range of integration is indicated on the right side of each row of plots.

is difficult to determine (the exercise in Appendix A does not work for $q_\emptyset$). We can only check the stability of the fit convergence of this parameter for the data we have. To test that the $\Delta\tau$ we are measuring really converges to 0 in the YKP parameterization, we also fit the correlation to:

$$C_2(q_\perp, q_{||}, q_\emptyset) = 1 + \lambda e^{-R_\perp^2 q_\perp^2 - R_{||}^2 \gamma^2 (q_{||} - v q_\emptyset)^2 - \frac{1}{x}\gamma^2 (q_\emptyset - v q_{||})^2} \tag{C.2}$$

where $x = 1/\Delta\tau^2$. In this form we allow the x parameter to be "as close to zero as it wants to be," (the degree of which can be limited by computer accuracy when we fit to $\Delta\tau$) or even negative. The $\Delta\tau$ in Table 6.5 is not zero exactly but instead on the order of 1x10^{-4} and the $x(= 1/\Delta\tau^2)$ is not exactly zero either. Since both fit function (with $\Delta\tau$ directly and $x = 1/\Delta\tau^2$) converged to 0 for the value of $\Delta\tau$, the convergence in both is stable. Another sign of stability of the fits is that the other fit parameters ($R_{||}$, $R_\perp$, v, and λ) converged to the nearly exact same values and errors using either fit functions.

Appendix D

Plots of $\vec{K}$ Dependence of C_2 Fit Paramters

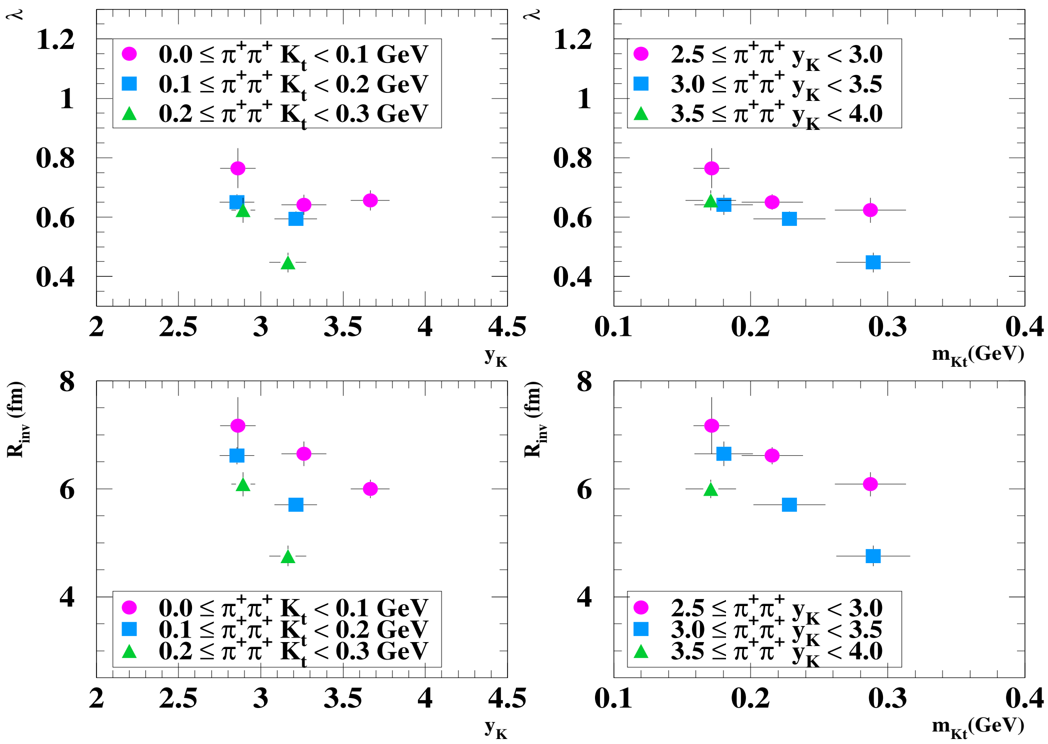

Figure D.1: $\vec{K}$ dependence of one dimensional C_2 fit parameters for $\pi^+\pi^+$ pairs. The left column shows y_K dependence. The right column shows m_{K_t} dependence.

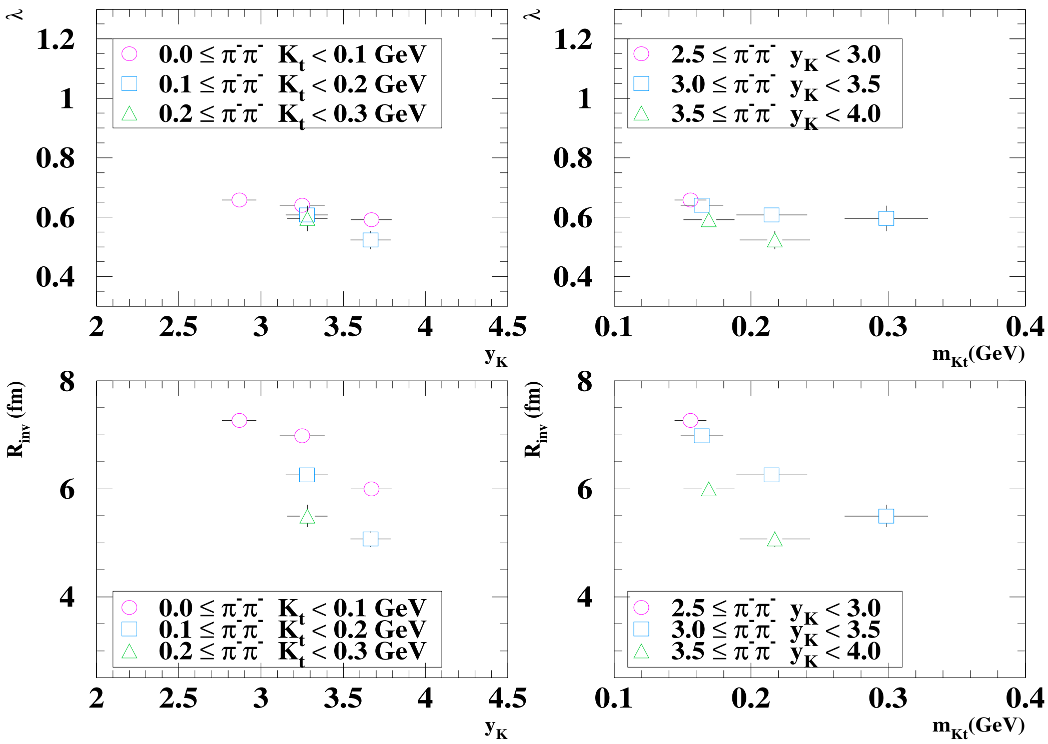

Figure D.2: $\vec{K}$ dependence of one dimensional C_2 fit parameters for $\pi^-\pi^-$ pairs. The left column shows y_K dependence. The right column shows m_{K_t} dependence.

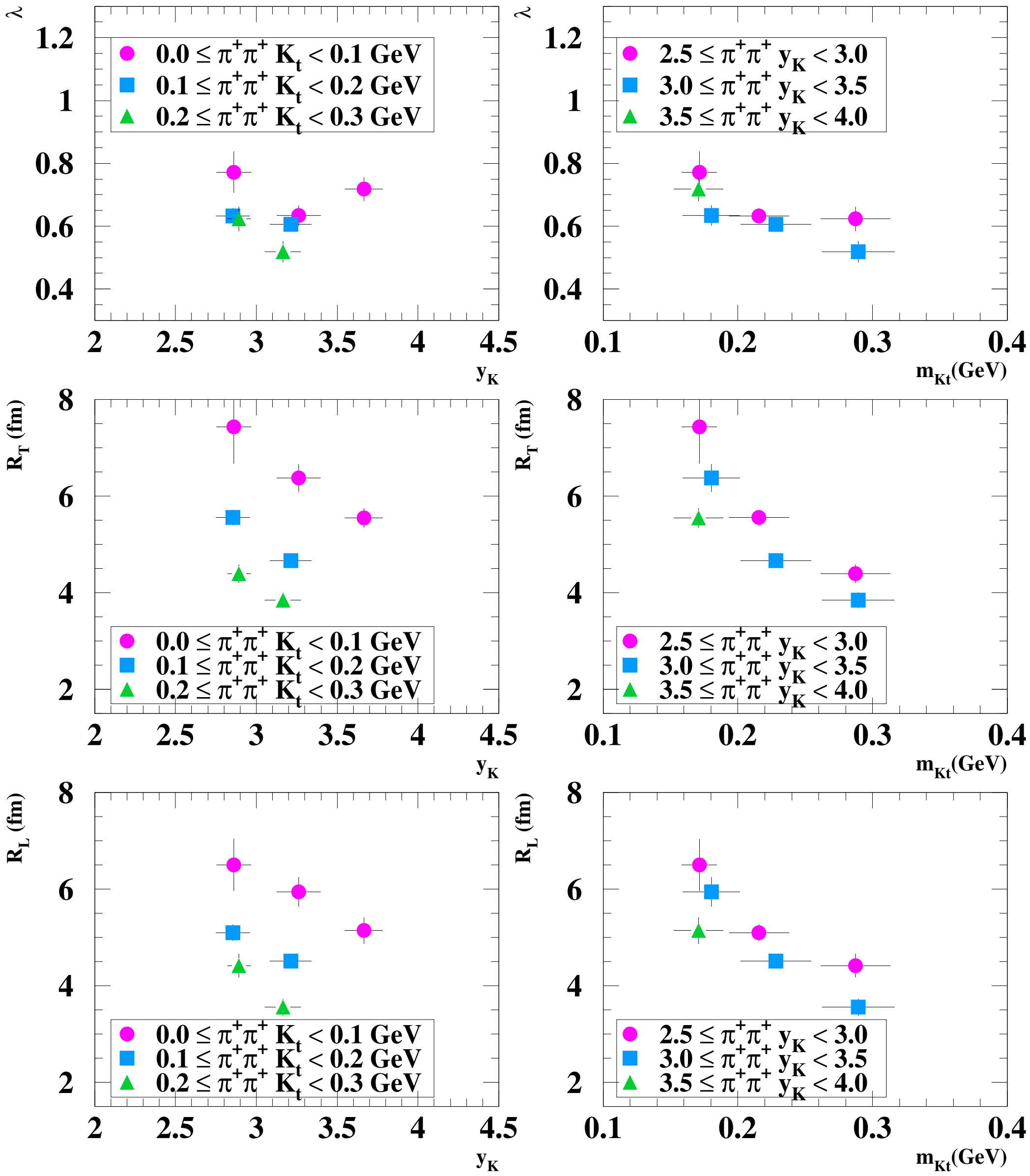

Figure D.3: $\vec{K}$ dependence of two dimensional C_2 fit parameters for $\pi^+\pi^+$ pairs. The left column shows y_K dependence. The right column shows m_{K_t} dependence.

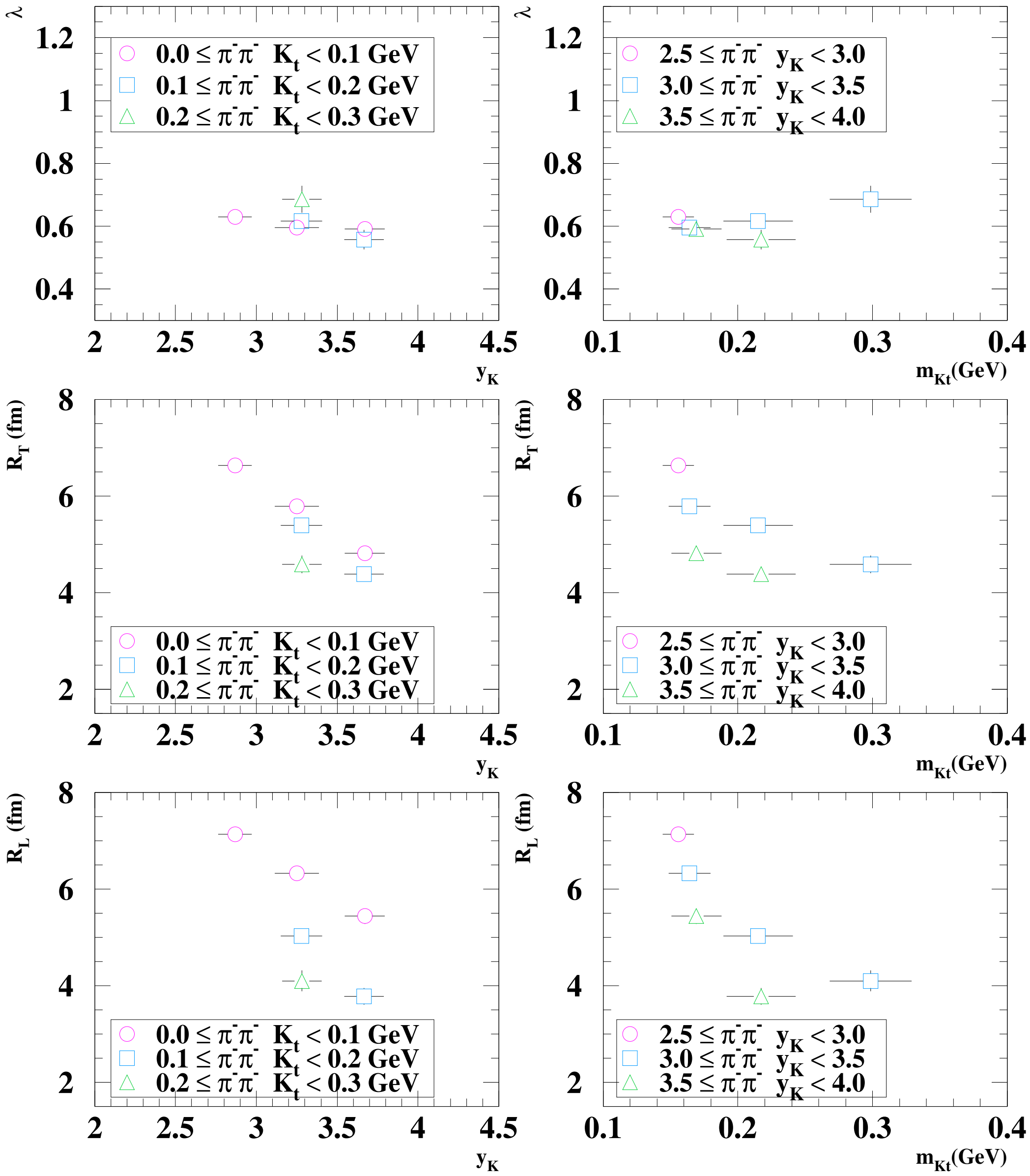

Figure D.4: $\vec{K}$ dependence of two dimensional C_2 fit parameters for $\pi^-\pi^-$ pairs. The left column shows y_K dependence. The right column shows m_{K_t} dependence.

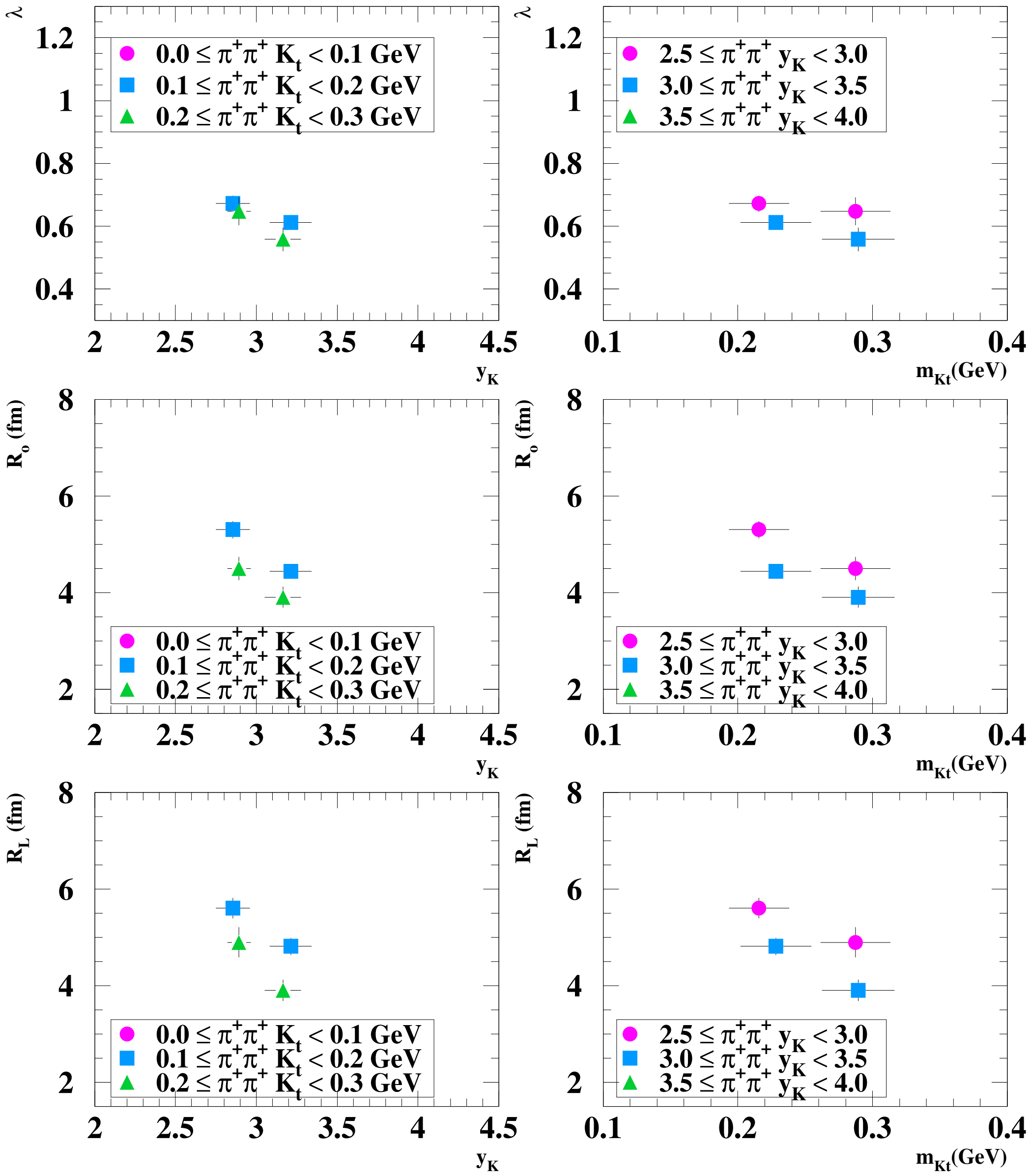

Figure D.5: $\vec{K}$ dependence of three dimensional C_2 BP fit parameters for $\pi^+\pi^+$ pairs. The left column shows y_K dependence. The right column shows m_{K_t} dependence.

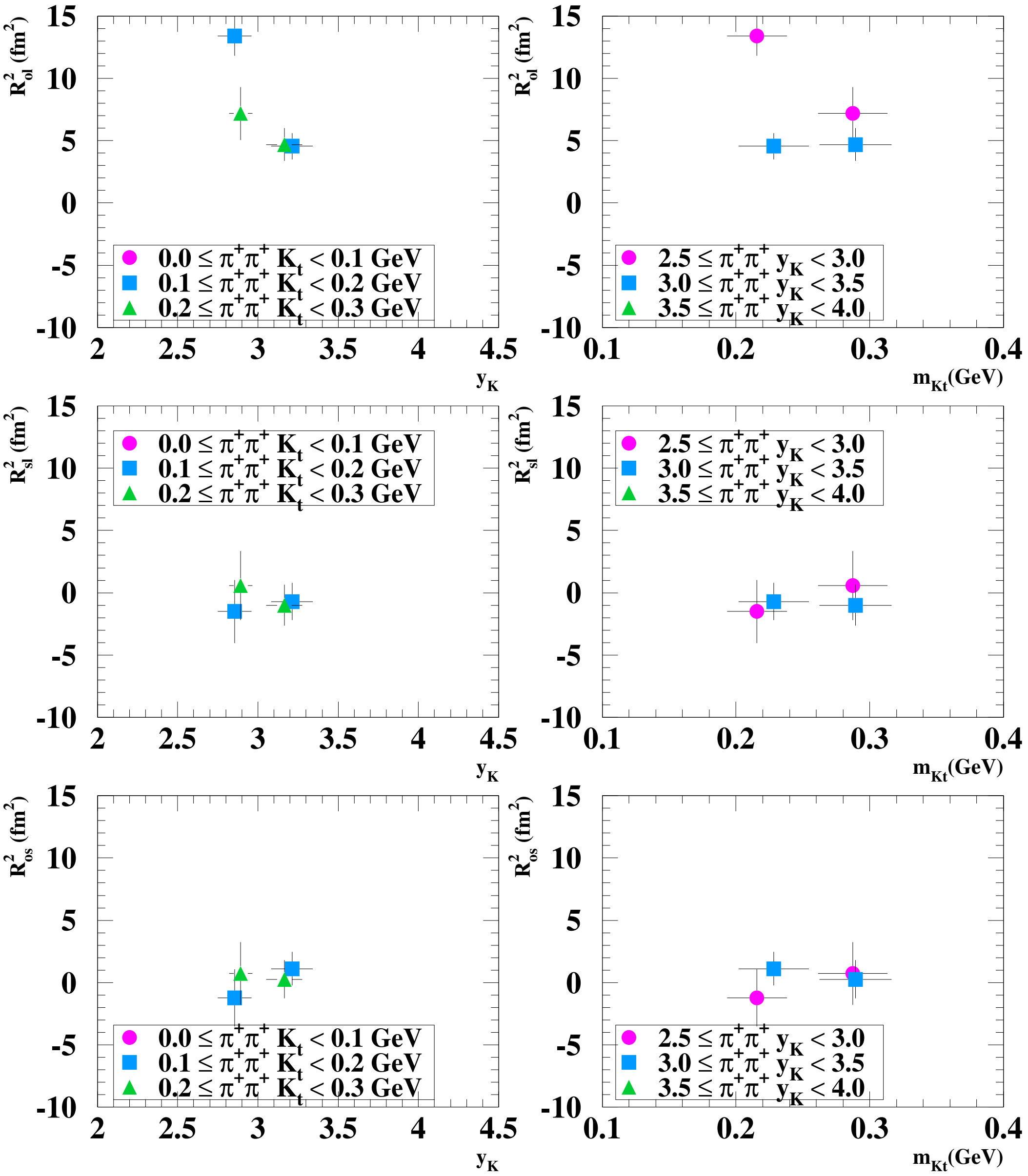

Figure D.6: $\vec{K}$ dependence of three dimensional C_2 BP fit parameters for $\pi^+\pi^+$ pairs. The left column shows y_K dependence. The right column shows m_{K_t} dependence.

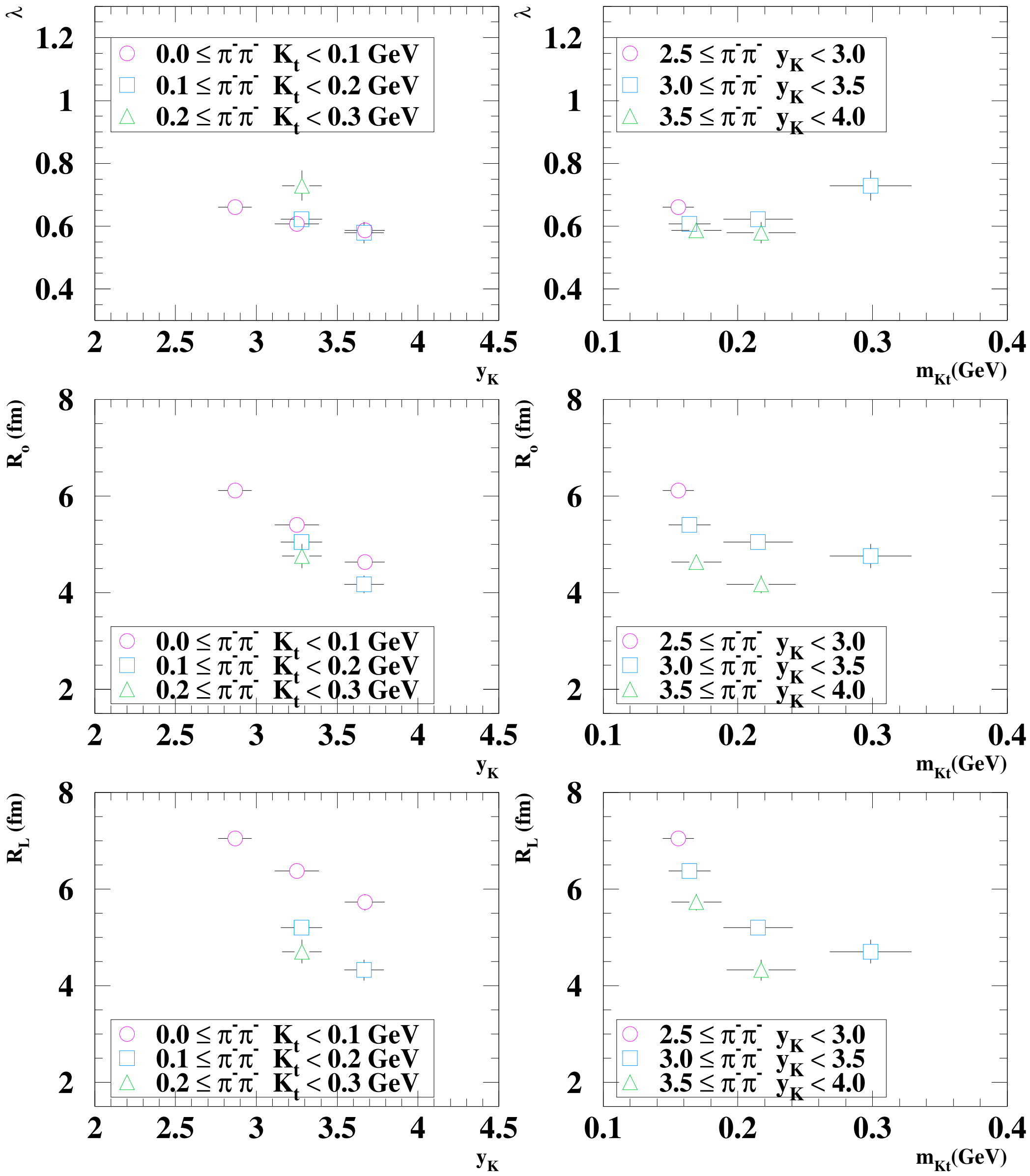

Figure D.7: $\vec{K}$ dependence of three dimensional C_2 BP fit parameters for $\pi^-\pi^-$ pairs. The left column shows y_K dependence. The right column shows m_{K_t} dependence.

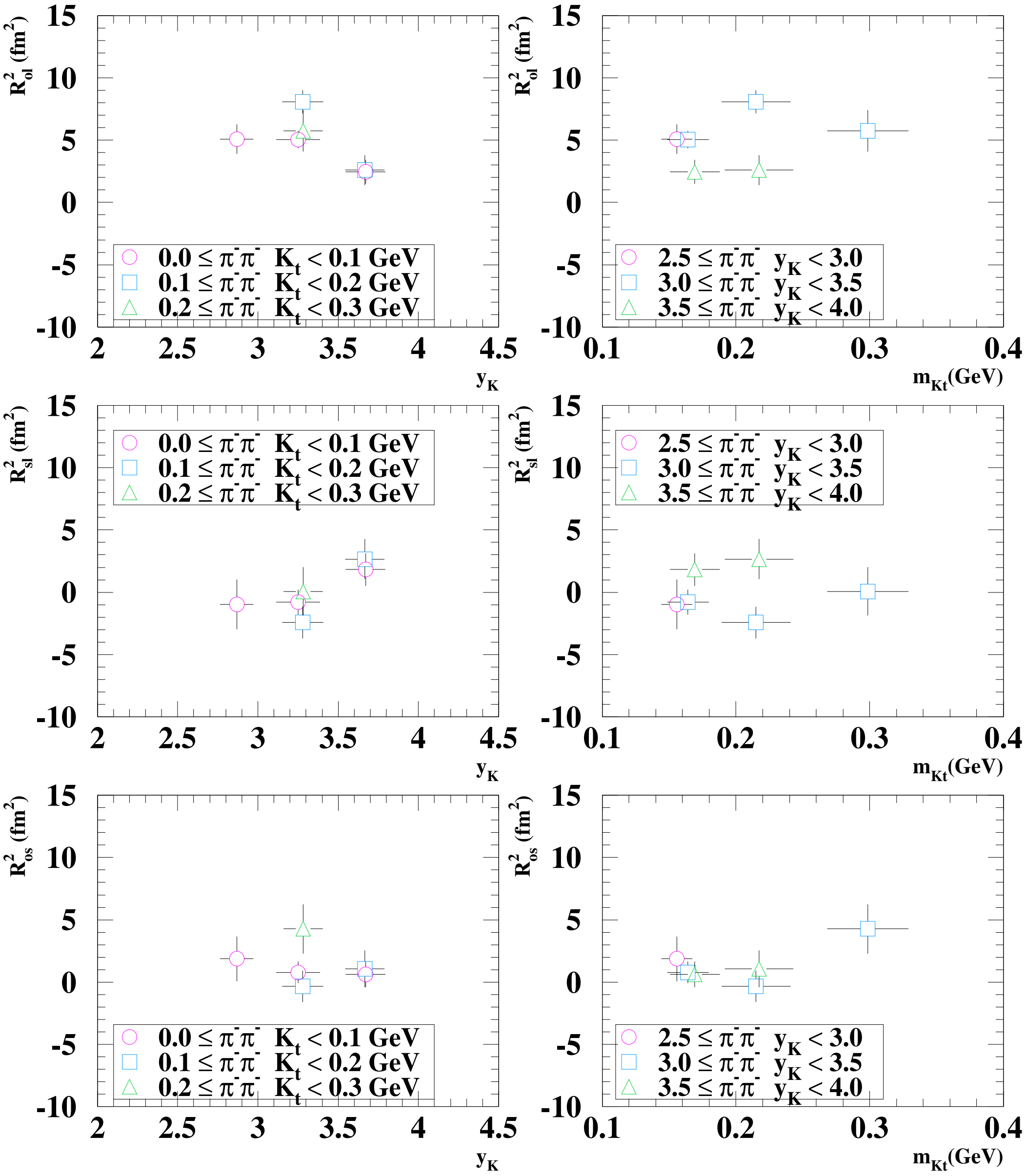

Figure D.8: $\vec{K}$ dependence of three dimensional C_2 BP fit parameters for $\pi^-\pi^-$ pairs. The left column shows y_K dependence. The right column shows m_{K_t} dependence.

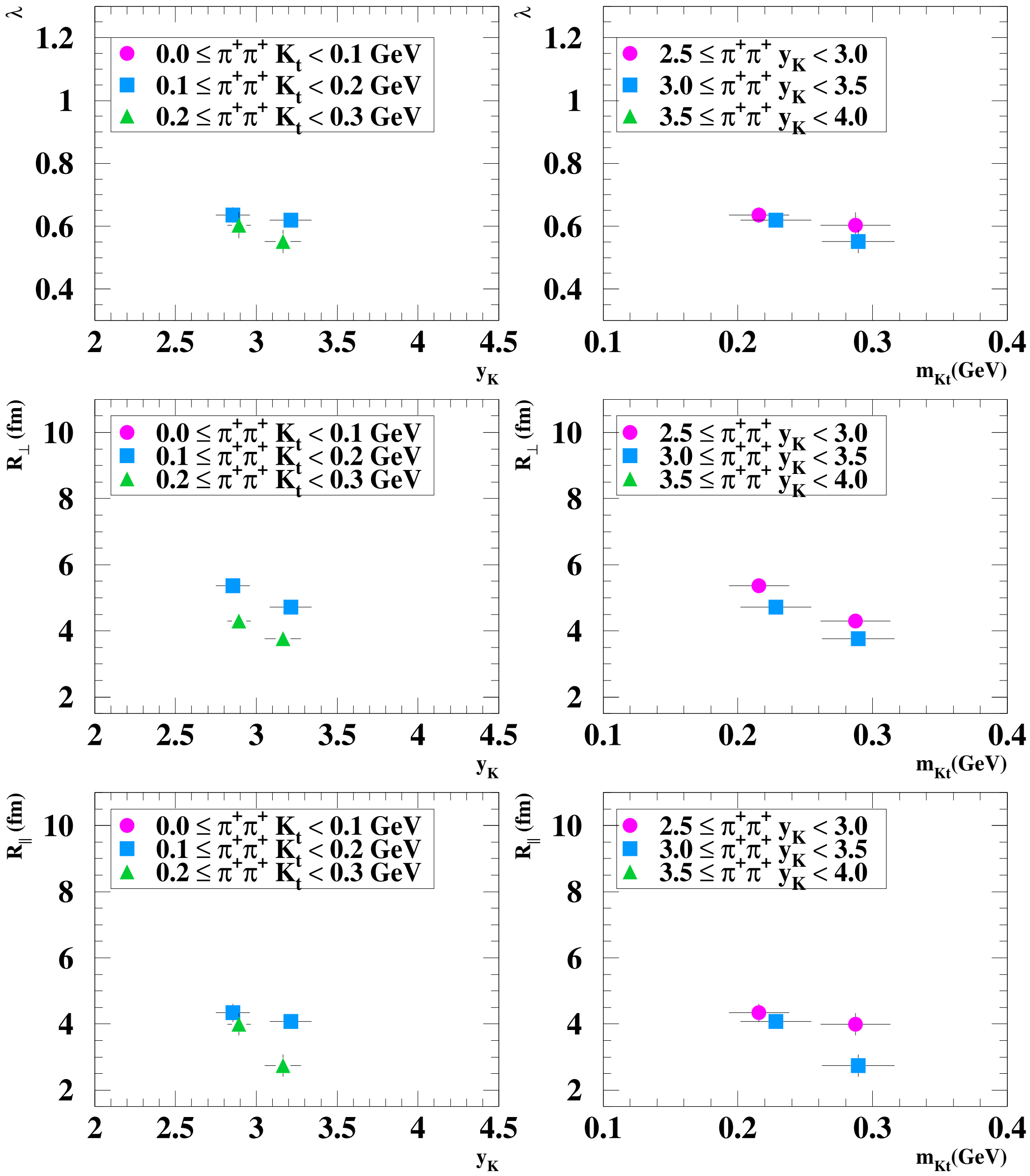

Figure D.9: $\vec{K}$ dependence of three dimensional C_2 YKP fit parameters for $\pi^+\pi^+$ pairs. The left column shows y_K dependence. The right column shows m_{K_t} dependence.

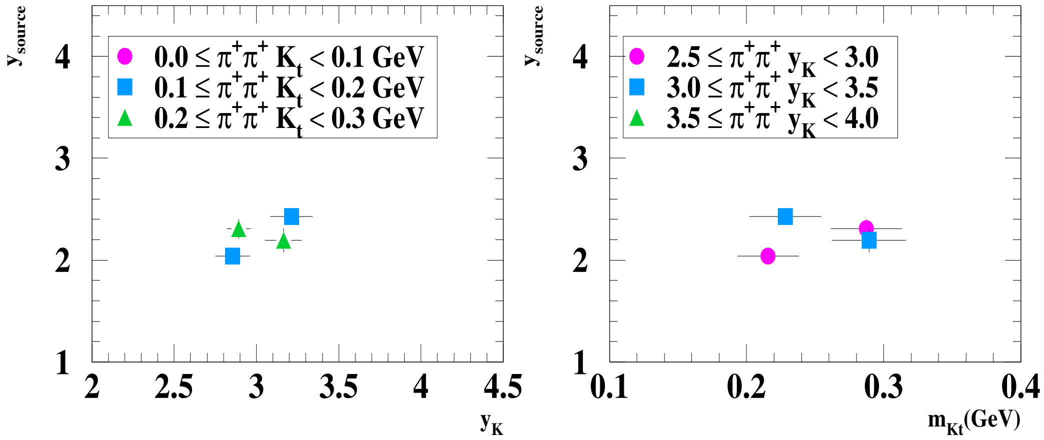

Figure D.10: $\vec{K}$ dependence of three dimensional C_2 YKP fit parameters for $\pi^+\pi^+$ pairs. The left column shows y_K dependence. The right column shows m_{K_t} dependence.